

**APPLICATION OF X-RAY DIGITAL IMAGE CORRELATION (XDIC)  
ON MATERIALS WITH ENGINEERED SPECKLES**

by  
**Junyu Wang**

**A Thesis**

*Submitted to the Faculty of Purdue University  
In Partial Fulfillment of the Requirements for the degree of*

**Master of Science**



School of Aeronautics and Astronautics  
West Lafayette, Indiana  
December 2020

**THE PURDUE UNIVERSITY GRADUATE SCHOOL**  
**STATEMENT OF COMMITTEE APPROVAL**

**Dr. Wayne Chen, Chair**

School of Aeronautics and Astronautics

**Dr. Michael Sangid**

School of Aeronautics and Astronautics

**Dr. Wenbin Yu**

School of Aeronautics and Astronautics

**Approved by:**

Dr. Wayne Chen

*To Kuo Zhou, Chaoyun Yan, and Zhonggui Wang,  
with Love.*

## **ACKNOWLEDGMENTS**

I would like to express my greatest gratitude towards Prof. Wayne Chen who has brought me into the research career and greatly helped me in every single aspect during my program here at Purdue. I would not have the opportunity to arrive where I am without his continuous guidance and support. I also want to thank Prof. Michael Sangid and Dr. Wenbin Yu for the knowledge I have learned from them and their willingness to help when I need in my study. I would also like to thank my fellow colleagues in patiently providing help whenever I approached. Among the colleagues, I would like to especially thank Jinling Gao who has always been available to help and provide invaluable discussions with which I can carry through doubts and indecisions, Cody Kirk who provided critical insights in my X-ray DIC work and crucial help with the experiments at Argonne APS, as well as Jonathan Drake and Amelia Leenig who provided early discussion and help with sample manufacturing.

I would like to thank the staffs at Purdue School of Aeronautics and Astronautics for their great service behind the scenes and especially, Morgan Delaney, for spending time with me to sort out many procedural problems during my program. I would like to thank the staffs at APS, Argonne National Laboratory, especially Kamel Fezzaa. Their continuous help to our lab made this study possible.

I would like to send my warmest thanks to my wife, Kuo Zhou, who had decided to abandon her own career and come to accompany and support me in the US, for her unwavering love and trust for 8 years so that I can be determined to pursue my goals. My life has been enjoyable every day I spent with her. My warmest gratitude is also towards my parents, Chaoyun Yan and Zhonggui Wang, for their determination to send me to a long journey when I was a teenager and their unwavering support throughout the years. Last but not least, I would like to thank my friends, especially Yuhao Wen, for the joy and laughter we had together that expelled the bore and loneliness of being abroad.

# TABLE OF CONTENTS

LIST OF TABLES .....	7
LIST OF FIGURES .....	8
ABSTRACT .....	11
1. INTRODUCTION .....	12
1.1 Overview .....	12
1.2 X-Ray Digital Image Correlation.....	18
1.3 Synchrotron X-ray PCI .....	25
1.4 Research objectives.....	26
2. EXPERIMENTAL METHODS .....	28
2.1 Materials and Sample Preparation .....	28
2.2 Types of Particles.....	32
2.3 Kolsky Compression Bar Apparatus.....	33
2.4 X-ray Control .....	35
2.5 Digital Image Correlation .....	36
2.5.1 Sub-pixel Registration .....	38
2.5.2 Sub-pixel Search Algorithm .....	38
2.5.3 Mean Intensity Gradient (MIG).....	40
2.5.4 Theoretical Error Estimation .....	41
3. RESULTS AND DISCUSSION.....	43
3.1 Bright Field Correction .....	43
3.2 Phase Contrast Imaging Results.....	43
3.2.1 FeO Inclusions at 4% Weight .....	44
3.2.2 FeO Inclusions at 7% Weight .....	46
3.2.3 FeO Inclusions at 10% Weight .....	48
3.2.4 FeO Inclusions at 13% Weight .....	50
3.2.5 WC Inclusions at 4% Weight .....	52
3.2.6 WC Inclusions at 7% Weight .....	54
3.2.7 WC Inclusions at 10% Weight .....	56
3.2.8 WC Inclusions at 13% Weight .....	58

3.2.9	Pt Inclusions at 5% Weight.....	60
3.2.10	Speckle Assessment and Error Analysis .....	62
3.3	X-ray DIC Results.....	65
3.3.1	FeO Inclusions at 4% Weight .....	66
3.3.2	FeO Inclusions at 7% Weight .....	68
3.3.3	FeO Inclusions at 10% Weight .....	69
3.3.4	FeO Inclusions at 13% Weight .....	70
3.3.5	WC Inclusions at 4% Weight .....	71
3.3.6	WC Inclusions at 7% Weight .....	72
3.3.7	WC Inclusions at 10% Weight .....	73
3.3.8	WC Inclusions at 13% Weight .....	74
3.3.9	Pt Inclusion with 5% Weight.....	75
3.3.10	WC Inclusion with 4% Weight at Finer Resolution.....	76
3.3.11	Discussion on the DIC Result .....	78
3.4	Kolsky Bar Results .....	79
4.	CONCLUSION.....	84
5.	FUTURE RESEARCH.....	86
	REFERENCES .....	87
	VITA.....	92

## LIST OF TABLES

Table 1. All Types of Added Particles.....	32
Table 2. Commonly Seen Correlation Schemes. ....	37
Table 3. Mean Intensity Gradient of Each Sample. ....	63
Table 4. Theoretical Deviation Error of Each Sample.....	64
Table 5. Subset Size Required to Ensure 0.01 pixels Theoretical Error.....	64
Table 6. Reuss and Voight Limits for Each Sample.....	83

## LIST OF FIGURES

Figure 1. (1) SEM-DIC at sub-micron to micron level. Movement detected is ~40 nm [7]. (2) FEM-DIC on rock ring under compression. The speckle field is first discretized [13]. (3) 3-D DIC on thermal deformation of Chromium-Nickel austenite in 3D [12]. .....	13
Figure 2. Basic Concept of DIC—A Displacement Measurement [14]. .....	14
Figure 3. Basic Concept of 3-D DIC [12]. .....	15
Figure 4. Basic Concept of FEM-DIC. a) The reference and deformed subsets. b) The meshed reference region of interest. c) The deformed mesh [13]. .....	16
Figure 5. X-ray field of view (FOV) of additively manufactured energetic composite. ....	17
Figure 6. HMX crystal embedded in Sylgard® under X-ray PCI. The arrow points to the crystal [16]. .....	19
Figure 7. a) XPCI images of etched aluminum sample under compression, b) The shear strain field, c) The axial strain field, d) and von Mises strain field [15]. .....	20
Figure 8. XPCI images of PMMA plate embedded with glass beads a) pre- and b) after-shock loading. c) Horizontal displacement field. d) Vertical displacement field [15]. .....	21
Figure 9. a) The speckle size distribution and b) the gray level intensity distribution [23]. ....	22
Figure 10. The XPCI images and corresponding DIC analysis results of the titanium sample under dynamic tension. The arrow indicates microcracks forming [25]. ....	23
Figure 11. XPCI images and DIC results of sample under dynamic tension. The dashed ellipses mark strain localization sites [25]. .....	24
Figure 12. Comparison between PCI images a) without and b) with edge enhancement. The sample-detector distance is a) 0.5 cm and b) 25 cm [27]. .....	26
Figure 13. Commercially Available Sylgard®. ....	28
Figure 14. a) A picture, b) a schematic of the stainless-steel mold top, and c) a schematic of the plastic mold base. ....	29
Figure 15. a) Sylgard® cylinder with WC, removed from the mode. b) Sample of Sylgard® with FeO cut from the cylinder. ....	30
Figure 16. A schematic and a picture of the sample holder. ....	31
Figure 17. Schematic of the sample gripper. ....	31
Figure 18. A Schematic of Kolsky Bar Apparatus at Beamline 32-B. ....	34
Figure 19. Synchronization Scheme of the X-ray and Kolsky Bar Apparatus. ....	36
Figure 20. Mapping of points in a subset from reference image to deformed image [21]. ....	38



Figure 21. A list of speckles with decreasing MIG [24].....	41
Figure 22. Comparison between a) uncorrected and b) corrected XPCI images of Sylgard® with 13% FeO. ....	43
Figure 23. Sylgard® with 4% FeO particles under impact.....	45
Figure 24. Mean Intensity Gradient Change during the Impact Process, 4% FeO. ....	45
Figure 25. Gray Level Intensity Distribution in the 4% FeO Sample Image. ....	46
Figure 26. Sylgard® with 7% FeO particles under impact.....	47
Figure 27. Mean Intensity Gradient Change during the Impact Process, 7% FeO. ....	47
Figure 28. Gray Level Intensity Distribution in the 7% FeO Sample Image. ....	48
Figure 29. Sylgard® with 10% FeO particles under impact.....	49
Figure 30. Mean Intensity Gradient Change during the Impact Process, 10% FeO. ....	49
Figure 31. Gray Level Intensity Distribution in the 10% FeO Sample Image. ....	50
Figure 32. Sylgard® with 13% FeO particles under impact.....	51
Figure 33. Mean Intensity Gradient Change during the Impact Process, 13% FeO. ....	51
Figure 34. Gray Level Intensity Distribution in the 13% FeO Sample Image. ....	52
Figure 35. Sylgard® with 4% WC particles under impact. ....	53
Figure 36. Mean Intensity Gradient Change during the Impact Process, 4% WC. ....	53
Figure 37. Gray Level Intensity Distribution in the 4% WC Sample Image.....	54
Figure 38. Sylgard® with 7% WC particles under impact. ....	55
Figure 39. Mean Intensity Gradient Change during the Impact Process, 7% WC. ....	55
Figure 40. Gray Level Intensity Distribution in the 7% WC Sample Image.....	56
Figure 41. Sylgard® with 10% WC particles under impact. ....	57
Figure 42. Mean Intensity Gradient Change during the Impact Process, 10% WC. ....	57
Figure 43. Gray Level Intensity Distribution in the 10% WC Sample Image.....	58
Figure 44. Sylgard® with 13% WC particles under impact. ....	59
Figure 45. Mean Intensity Gradient Change during the Impact Process, 13% WC. ....	59
Figure 46. Gray Level Intensity Distribution in the 13% WC Sample Image.....	60
Figure 47. Sylgard® with 5% Pt particles under impact. ....	61
Figure 48. Mean Intensity Gradient Change during the Impact Process, 5% Pt. ....	61
Figure 49. Gray Level Intensity Distribution in the 5% Pt Sample Image. ....	62

Figure 50. Intensity Distribution Comparison between the 4% FeO Sample and the 4% WC Sample.	65
Figure 51. Displacement map of the 4% FeO sample.	66
Figure 52. Displacement map of the 7% FeO sample.	68
Figure 53. Displacement map of the 10% FeO sample.	69
Figure 54. Displacement map of the 13% FeO sample.	70
(5) Frame 90-93 (82.8 $\mu$ s to 85.56 $\mu$ s)      (6) Frame 110-113 (101.2 $\mu$ s to 103.96 $\mu$ s) Figure 55.	
Displacement map of the 4% WC sample.	71
Figure 56. Displacement map of the 7% WC sample.	72
Figure 57. Displacement map of the 10% WC sample.	73
Figure 58. Displacement map of the 10% WC sample.	74
Figure 59. Displacement map of the 10% WC sample.	75
Figure 60. Displacement map of the 4% WC sample using 19 X 19 subsets.	76
Figure 61. Displacement map of the 4% WC sample using 13 X 13 subsets.	77
Figure 62. Calculated strain from single pulse loading for sample of 4% FeO.	80
Figure 63. Comparison of FeO samples and pure Sylgard®.	81
Figure 64. Comparison of WC samples and pure Sylgard®.	81
Figure 65. Comparison of WC samples and pure Sylgard®.	82

## ABSTRACT

As an intrinsic requirement for digital image correlation (DIC) to be applicable, the images must exhibit a speckle pattern of sufficient unique features. Researchers have incorporated X-ray phase contrast imaging (PCI) and DIC (XDIC) and conducted studies on materials with natural internal features as speckles. This study is the first attempt to explore the applicability and standards of XDIC to be applied on materials that are transparent under X-ray PCI, mainly polymers, by deliberately embedding particles into the sample. The goal is to generate a high-quality speckle while maintaining the least influence on the material's properties. Iron oxide (FeO), tungsten carbide (WC), and platinum (Pt) are embedded into Sylgard® epoxy at various weight ratios, and the Sylgard® samples are loaded with a Kolsky compression bar paired with high-speed X-ray PCI. The speckle quality of the PCI images is assessed using a mean intensity gradient based approach, as well as intensity distribution analysis. DIC is applied to the images to measure the displacement field in the loading direction, and the results are analyzed. The engineering stress-strain relationship is generated from the Kolsky bar apparatus, and the results are compared to find the influence of the added particles.

The results indicate that the addition of particles does not significantly alter the base polymer's properties, and the theoretical deviation error can be as low as less than 0.01 pixels. Disregarding the limited applicability to embed into polymer samples, platinum produces the best speckle. WC particle is the superior choice of material to embed for its good speckle quality, ease of embedding, and good availability. Lower weight ratios are shown to be preferential. This study also emphasizes the importance of sample design when applying XDIC to materials with embedded particles. It is preferential for best accuracy to design the region of interest to be away from the surfaces of the samples and be located near the back of the sample with respect to the impact surface.

# 1. INTRODUCTION

## 1.1 Overview

The motion and deformation of objects can be visualized by human eyes. They can also be recorded by a series of digital images. The visualization process inherently records the motion and deformation qualitatively. But how can they be measured quantitatively? Digital image correlation (DIC) was first developed in the 1980s as a non-contact optical technique for strain and displacement measurement [1][2]. This technique has had a great impact on the field of experimental solid mechanics since it was developed. Over the years, DIC as a technique has been consistently improved, and its application extended. Nowadays, the application of DIC has already been extended to a wide variety of time and space scales, and it is still under development [3]. By using an ultra-high-speed imaging tool, the time scale can be as small as nanoseconds [4][5]. With a scanning electron microscope (SEM) or an atomic force microscope (AFM), the space scale can be brought down to nanometers [6][7].

Essentially, DIC is an optical measurement technique. This nature brings many advantages over other measurement techniques such as strain gauges. First, it is non-contact and non-intrusive, meaning that taking the measurement does not interfere with the specimen during the experiment. Also, DIC is less sensitive to experimental conditions. It can be viable under extreme temperatures, corrosive conditions, or high humidity conditions [8][9]. As long as the specimen can be observed with an imaging device, digital image correlation could be applicable. The measured result using DIC is full-field instead of pointwise, which gives it advantages when localized deformation is of interest. Moreover, most of the costs are associated with the imaging process. Once the images are recorded, with the computing power nowadays, processing DIC can be fast and cheap [10][11]. Other extensions of DIC application include 3-D DIC, and finite element method (FEM) DIC [12][13]. Examples of these applications are shown in Fig. 1.

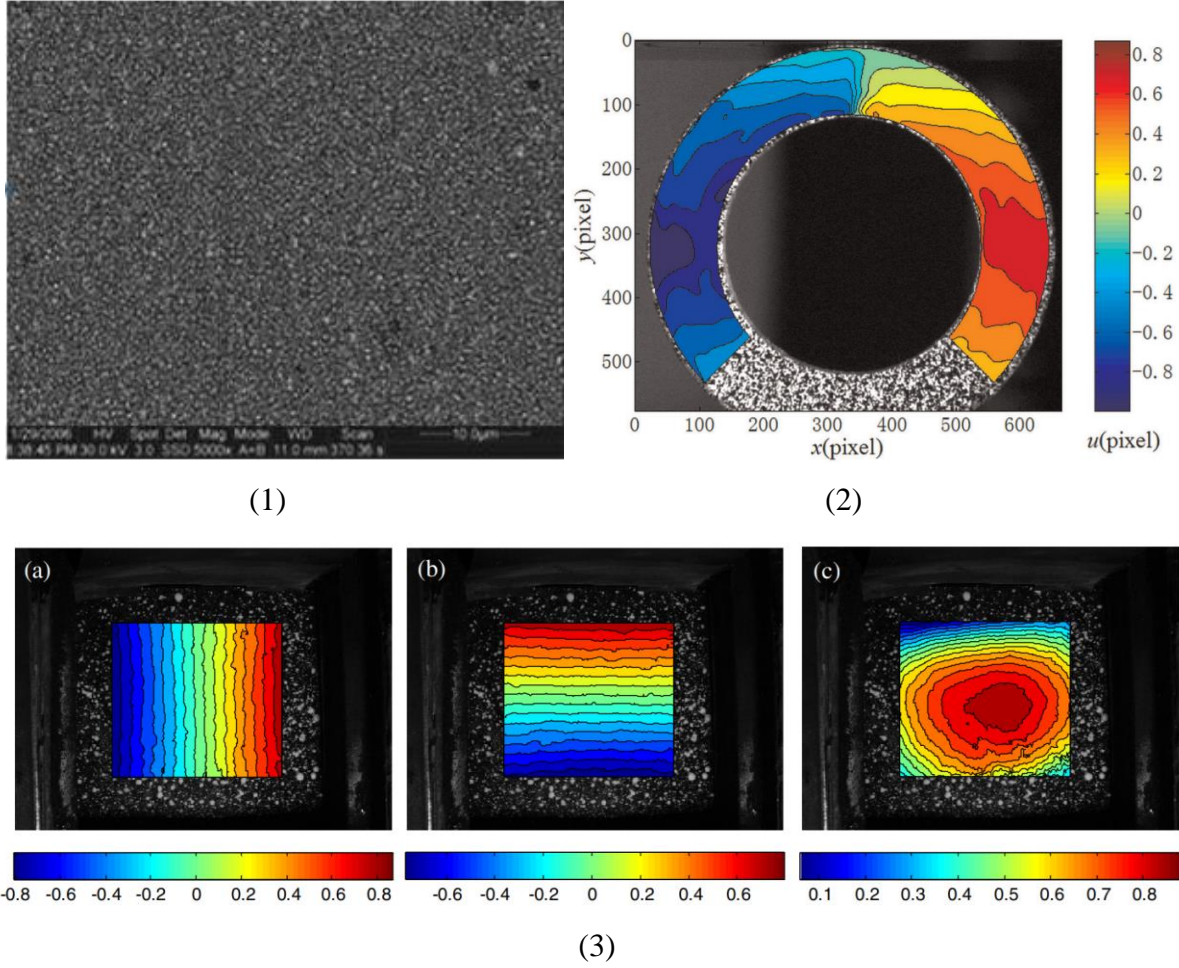


Figure 1. (1) SEM-DIC at sub-micron to micron level. Movement detected is  $\sim 40$  nm [7]. (2) FEM-DIC on rock ring under compression. The speckle field is first discretized [13]. (3) 3-D DIC on thermal deformation of Chromium-Nickel austenite in 3D [12].

The sole purpose of DIC is to measure the displacement field of an object under loading between two digital image frames. That is, after the correlation calculation, the displacement at any point in the region of interest should be known. With the displacement information, engineering strain field can be obtained. To achieve this, certain patterns of the object should be recognized in a reference frame and tracked in a frame deformed from the reference frame. The change in the relative positions of the pattern is therefore the displacement at that point. A simple illustration of this concept is given in Fig. 2. Since it is often impractical to obtain the displacement at any point in the region of interest from pattern tracking, in the area between the points with obtained displacements, the displacements are often interpolated. The way displacement is

calculated poses limitations to apply DIC in certain circumstances. Over the years, researchers have been trying to tackle the challenges by incorporating other advanced techniques.

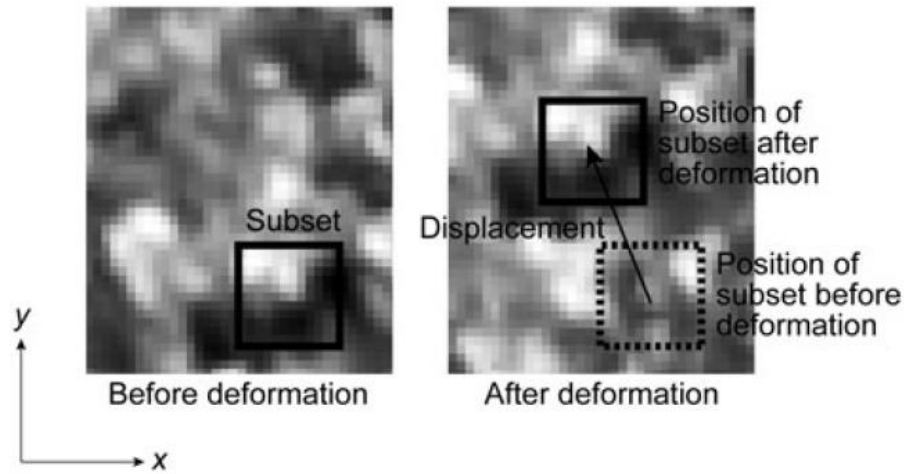


Figure 2. Basic Concept of DIC—A Displacement Measurement [14].

Since traditional DIC is an optical technique, the camera only captures what occurs on the surfaces. Thus, the regions far away from the surface, for example, the back surface of the specimen, cannot be measured. Therefore, it is important to carefully select the imaged surface such that localized displacement outside the imaged surface is non-significant. To tackle this challenge, three-dimensional (3D) DIC was developed. In 3-D DIC, two cameras at different angles are set up to record the deformation of a sample that exhibits a speckle pattern with the aid of artificial light sources. Figure 3 shows the basic concept of how 3-D DIC is performed. For a unique point on the sample defined in the reference image taken by one of the cameras, its position in the image taken by the other camera is different. Such difference can be obtained by 2-D correlations between images from the two cameras and be used to locate that point in the global 3-D coordinates. By performing 2-D DIC analysis on the deformed images, the global coordination of the point after deformation can be obtained. The displacement can thus be calculated from the position difference.

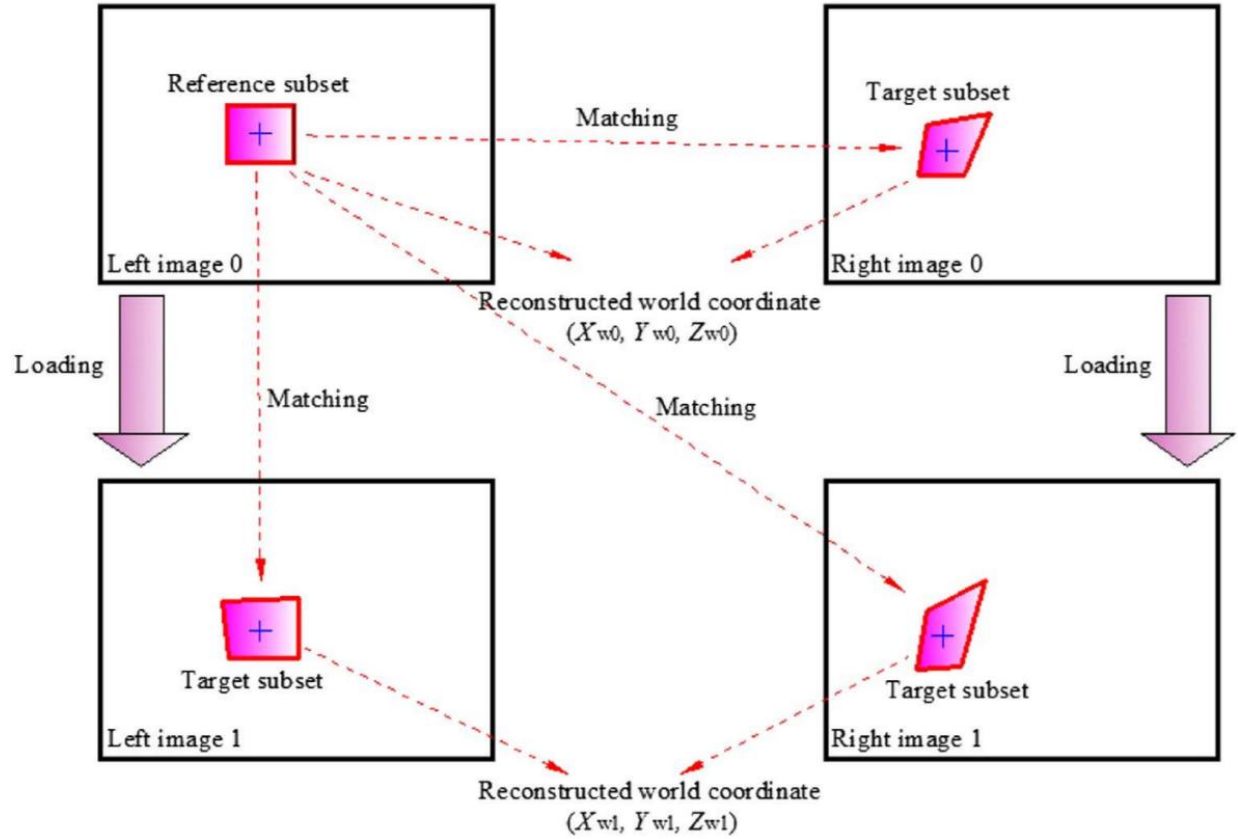


Figure 3. Basic Concept of 3-D DIC [12].

As a pattern is tracked from the original frame to deformed frame, it is assumed that the pattern is continuous across the frames. If there is any discontinuity in the pattern from the original frame to the deformed frame, such as cracks, the conventional algorithms would be unable to track the pattern. Also, it would be challenging to track large deformation and rotations between two consecutive images. To solve these problems, researchers have developed finite element method (FEM) DIC [13]. In finite element DIC, also known as mesh-based DIC, the regions of interest in the images are first discretized to form a mesh. Then the correlation is performed based on the whole mesh to find the nodal displacements, from which the displacement field can be obtained with the functions of choice. Just like the traditional FEM, shape functions and element types can also be chosen to achieve various goals. Figure 4 illustrates the basic concept of FEM-DIC.

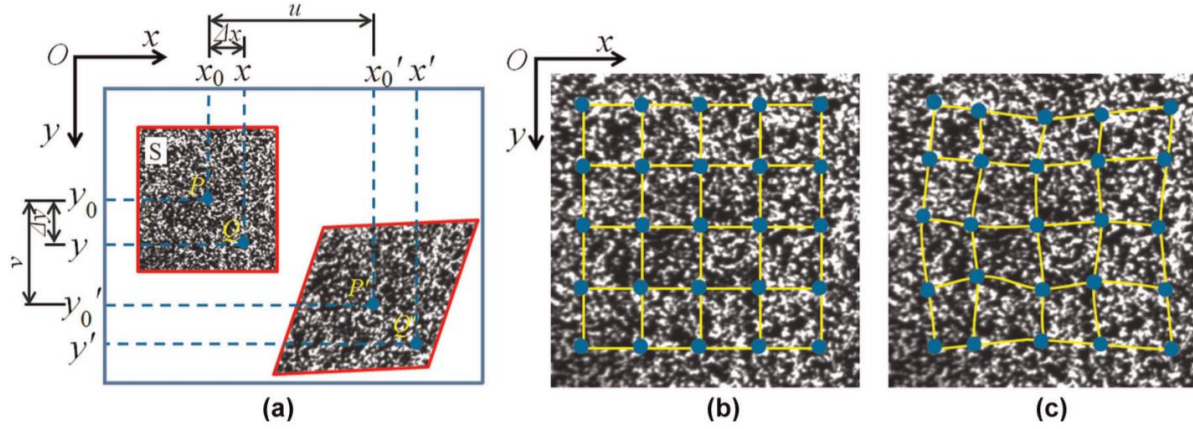


Figure 4. Basic Concept of FEM-DIC. a) The reference and deformed subsets. b) The meshed reference region of interest. c) The deformed mesh [13].

Sometimes, the displacement inside an opaque specimen may be of interest. However, it is impossible to see what happens inside with optical devices. To enable measurement inside an opaque specimen, the X-ray digital image correlation (XDIC) was developed [15]. Full-field synchrotron X-ray phase contrast imaging (PCI) enables *in-situ* visualization through a specimen under loading. Contrasts in digital images are produced as the X-ray goes through the medium with different phases. The X-ray signal is received by a scintillator and converted to optical signal. With the use of synchrotron X-rays and ultra-high-speed cameras, the frame rate can be as high as 5 million frames per second (fps). The converted phase contrast images have sufficient spatial and temporal resolution to be used for DIC measurements for dynamic events.

This technique is very useful in studying deformation process and damage behavior of a material under impact loading conditions. However, there must be some contrast inside the specimen to form the patterns to be tracked in DIC analysis. These phase differences can be from inherent features, such as inclusions in composite materials or different phases in alloys, or deliberately added inclusions as speckles if the material of interest either has no inherent phase differences or does not provide enough contrast.

Researchers have used XDIC to study the impact behavior of agglomerates of energetic materials, taking advantage of phase difference created by the energetic powder [16]. It has been shown that XDIC performs well on specimen with inherent speckles. Figure 4 shows the X-ray field of view of a specimen with inherent speckle patterns, which are made of energetic powders, for DIC analysis. However, as a novel technique of measuring in-volume deformation, its



applicability on specimen with engineered speckles remains barely touched. This work focuses on assessing how well XDIC performs in measuring the displacement field of materials with deliberately added particles, as well as exploring some guidelines with engineering the speckles that minimize their influence on the mechanical behavior of the base materials.

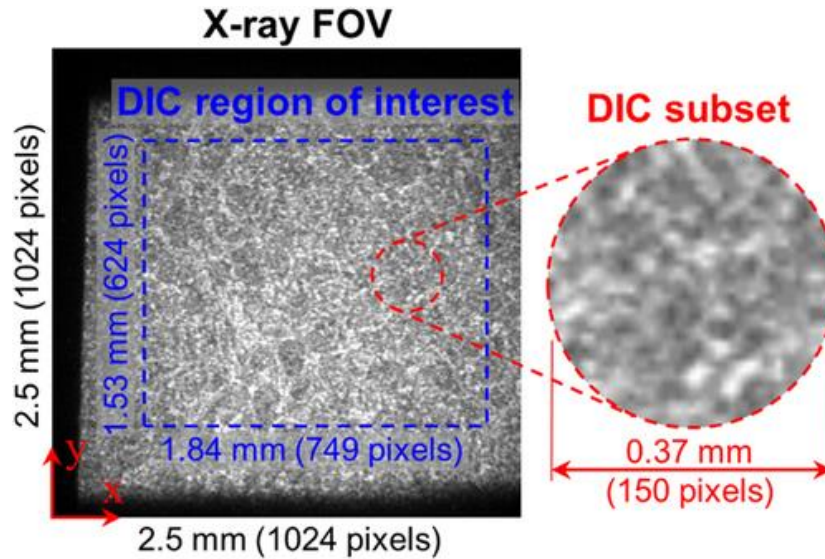


Figure 5. X-ray field of view (FOV) of additively manufactured energetic composite.

Another extension of the traditional DIC is digital volume correlation (DVC), which is also highly related to the subject of this study. DVC relies on 3-D imaging capabilities such as X-ray computed tomography (CT) or magnetic resonance imaging (MRI), which can reproduce the internal features and microstructures of a sample in a 3-D model. This method has been under constant develop for more than two decades and has been vastly applied in biomedical engineering, biomedical diagnosis, and material science [17]. In DVC, the constructed 3-D model is divided into sub-volumes, as contrast to a subset in traditional DIC [18]. By applying either purely numerical correlation schemes (similar to traditional DIC) or correlation schemes that enforce equilibrium and compatibility, a sub-volume that includes some microstructure can be tracked from a reference frame to a deformed frame, and the 3-D internal displacement field can be constructed in such way. Similar to traditional DIC, DVC has been developed in both algorithm aspect and application aspect. One of the example applications of DVC in biomedical study is the failure mode of augmented vertebrae bone [17]. Early material science studies utilizing DVC focused on the internal localization of bulk granular materials, while DVC was also vastly used

for metal alloys to study internal shear localization or even crack propagation in later years [17]. In the algorithm development aspect, researches target maximizing efficiency by eliminating redundant computation while also maximizing accuracy of measurement by implementing reliability-guided tracking strategy [18].

Similar to 2D-DIC, the viable measurements of DVC significantly rely on imaging capabilities. In DVC, the most commonly used imaging technique is X-ray CT or  $\mu$ CT with the available synchrotron facilities worldwide, such as Argonne National Lab or European Synchrotron Radiation Facility. While providing high resolution of the internal microstructure,  $\mu$ CT also introduce limitations. One of the limitations is what also exhibits in X-ray DIC. When the internal features are lacking in the sample, it becomes very challenging to create correlation between the reference image to the deformed image. Another challenge draws the line that distinguishes DVC from the subject of this research such that this work is not redundant with respect to DVC. A  $\mu$ CT constructs the 3-D image by scanning the internal features of a sample layer by layer before putting all the layers together to form the 3-D image. Even at a synchrotron beamline, the process of producing one frame takes several minutes. This significantly limits the loading rate of an *in-situ* measurement to be within the quasi-static range.

## 1.2 X-Ray Digital Image Correlation

X-ray digital image correlation (XDIC) is a novel technique that enables in-volume measurement of the displacement field in a specimen under loading. This technique is based on full-field synchrotron X-ray phase contrast imaging. For this work, the PCI was performed at Beamline 32 ID-B, Advanced Photon Source (APS), Argonne National Laboratory, Illinois [19][20]. The initial drive for developing this technique is to achieve good spatial and temporal resolutions in the measurement in a dynamic loading event. In the proof-of-concept study, it was shown that the technique was capable for experiments on samples with both natural speckles and artificial speckles under dynamic loading, including using Kolsky tension bar and gas gun. It is critically important to note the difference between XDIC and traditional DIC in terms of specimen eligibility. For traditional DIC, the speckles to be tracked between the frames can be natural patterns on the specimen surface, or sprayed patterns on the surface [21]. With speckle spraying, the eligible specimen material types are as broad as almost anything. However, the eligible materials for XDIC, are much more limited. The speckles to be tracked between the frames must

be from the phase difference inside the specimen. This does not only require heterogeneity, but also require enough diffraction index of the heterogeneity. For example, a composite made of two similar materials, although heterogeneous, is not suitable for XDIC because the PCI cannot produce enough speckles. An example of an ineligible heterogeneous specimen is shown in Fig. 6 [22]. The X-ray PCI image shows an HMX crystal embedded in Sylgard® epoxy under impact. The displacement field around the crystal is of interest but cannot be measured with DIC due to poor speckle patterns. It can be seen that the borders are relatively vague under PCI compared to the speckles in successful traditional DIC images presented previously or the XDIC images presented later. Although the specimen was not designed for XDIC, it showcased that the importance of material eligibility for XDIC.

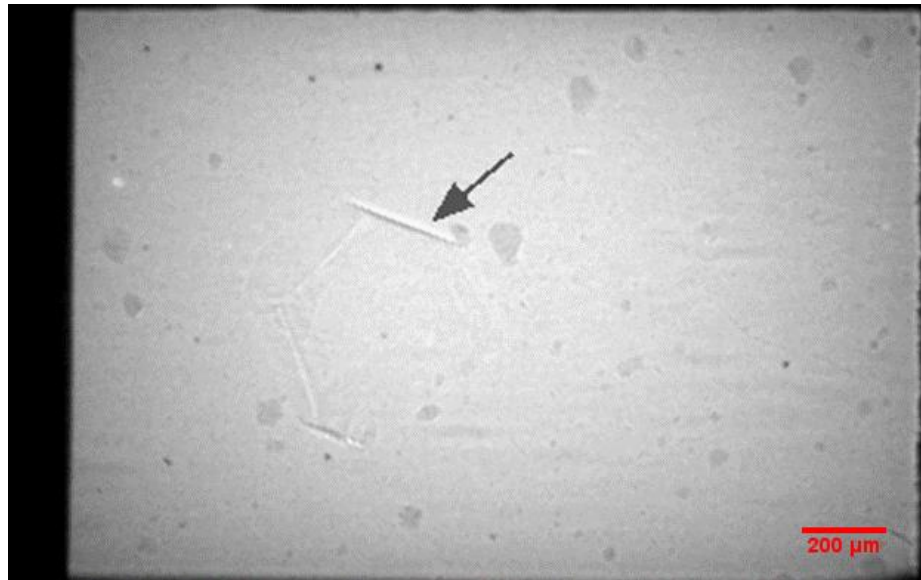


Figure 6. HMX crystal embedded in Sylgard® under X-ray PCI. The arrow points to the crystal [16].

In the proof-of-concept study, two different conditions were studied and validated. The first experiment is a strain field measurement on an etched Al dog-bone sample under dynamic tension loading using a Kolsky tension bar at a striker impact speed of 8 m/s. The samples are 0.5 mm thick and chemically etched with hydrofluoric acid to make a  $\sim 100\ \mu\text{m}$  hole. Figure 7 presents the PCI images and DIC results at various time instants. Etched Al samples create a natural pattern of speckles under X-ray PCI. During the loading process, the etched hole was observed to be

growing, and a shear band was observed to form. In the corresponding XDIC measurement mapping, strain was observed to concentrate near the etched hole. The shear band was also verified in the measurement. Another experiment was an impact on borosilicate glass beads embedded PMMA plates using a gas gun. The sand particles inside the PMMA plate forms a speckle pattern that can be tracked by XDIC. Figure 8 shows the images taken by the high-speed camera and the corresponding DIC results for the PMMA plate experiment.

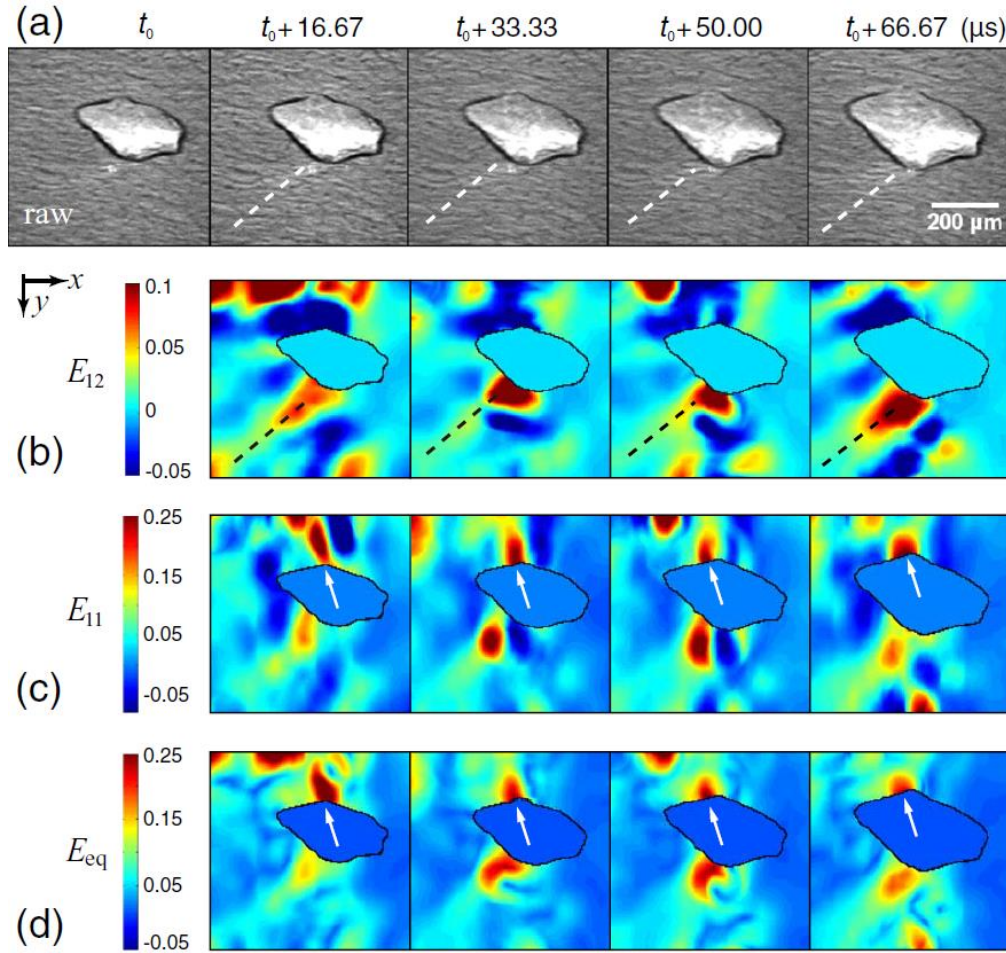


Figure 7. a) XPCI images of etched aluminum sample under compression, b) The shear strain field, c) The axial strain field, d) and von Mises strain field [15].

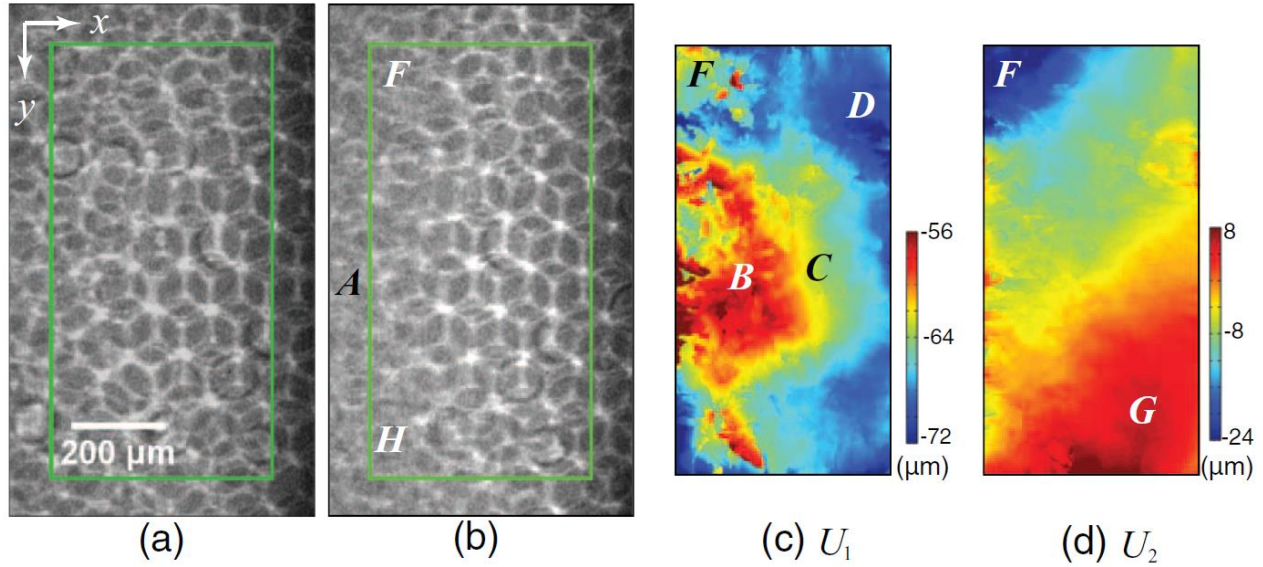


Figure 8. XPCI images of PMMA plate embedded with glass beads a) pre- and b) after-shock loading. c) Horizontal displacement field. d) Vertical displacement field [15].

Since XDIC was first developed, several studies were done utilizing this technique. A study on dynamic shear localization of titanium alloys under high-rate tension was performed using XDIC, as well as a comparison experiment at quasi-static loading rate [23]. In this study, adiabatic shear bands inside Ti-6Al-4V under dynamic tension were observed, and the in-situ temperature and displacement field were measured. The in-situ observation of the dynamic tension was made by XPCI, and the images were used for DIC analysis to yield the strain fields. The Ti-6Al-4V rod samples were loaded using Kolsky tension bars. In this study, the quality and sizes of the speckles needed for DIC analysis were assessed and analyzed. The speckles come from naturally occurring patterns of surface roughness caused by machining. The transmitted X-ray along with edge enhancement can produce a speckle pattern when such roughness is present. The quality and sizes were analyzed based on the image morphologies with a circular speckle assumption. The sample under XPCI, gray level histogram, and size histogram are shown in Fig. 9. The average speckle size is 5 pixels, corresponding to 20  $\mu\text{m}$ . Based on gray level distribution, the quality of the images for DIC analysis were assessed with its mean intensity gradient—a parameter developed by Pan, *et al*, which will be introduced in later chapters [24]. The result showed that the PCI images had high quality speckles according to the assessment standards.



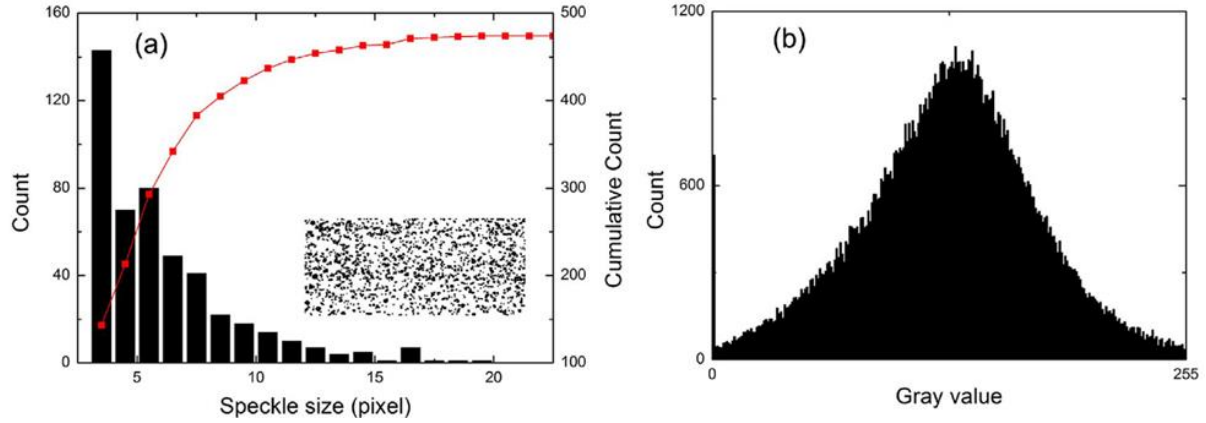


Figure 9. a) The speckle size distribution and b) the gray level intensity distribution [23].

The bulk stress and strain were measured using the standard Kolsky tension bar apparatus. The selected phase contrast images and corresponding strain maps at the corresponding instances are presented in Fig. 10. In the beginning, all strains were homogeneous. A band of deformation was then observed to form near the center and propagate at approximately 45 degrees. Shear localization was observed inside the band as the sample were further compressed. The localized shear grew independently until they coalesced into a deformation band at approximately 50 degrees. The width, measured to be  $\sim 350 \mu\text{m}$ , appeared larger than those under quasi-static loading condition [25]. Utilizing the natural speckles on the titanium alloy rods, the in-situ strain maps and shear band localization were easily obtained and observed with XDIC.

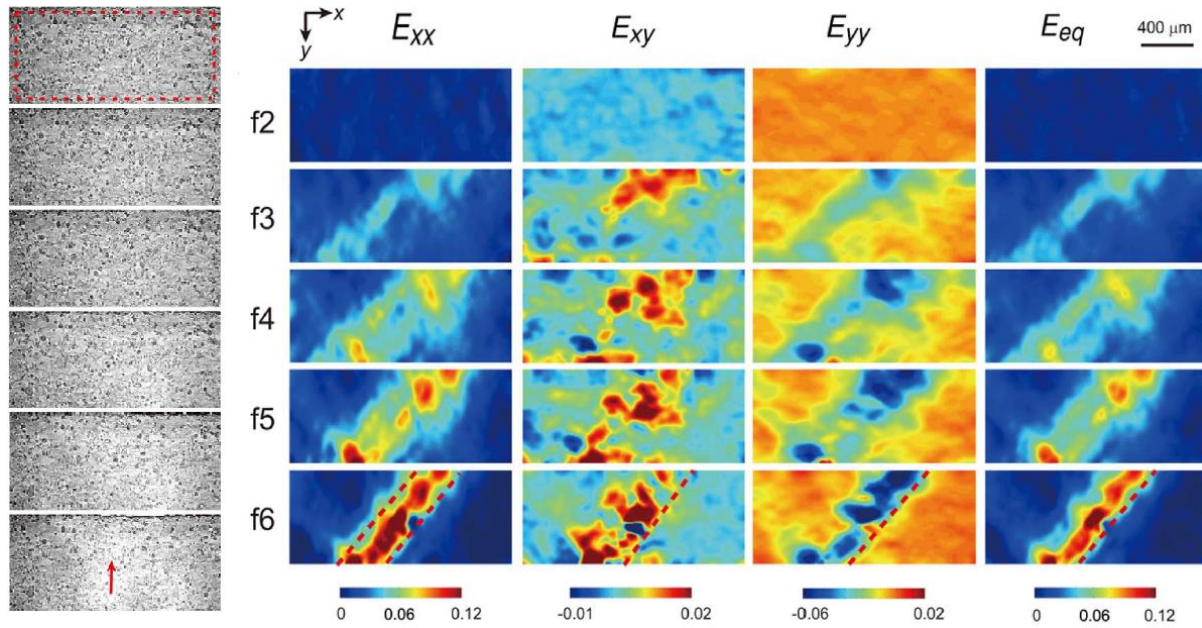


Figure 10. The XPCI images and corresponding DIC analysis results of the titanium sample under dynamic tension. The arrow indicates microcracks forming [25].

Another dynamic tensile study using XDIC was performed on dynamic deformation and damage behavior of B<sub>4</sub>C-reinforced aluminum—a metal matrix composite (MMC) [25]. In this study, a high hardness reinforcement phase used in metal matrix composites was studied under high-rate ( $10^2 - 10^4 \text{ s}^{-1}$ ) tensile experiments. The study focused on in-situ characterization of deformation and damage inside the samples to understand the dynamic response of this material. Two types of samples of different weight ratios of B<sub>4</sub>C were made. The experiment was conducted with a Kolsky tension bar synchronized with high-speed X-ray PCI. X-ray DIC was used to analyze the internal strain mapping during the deformation process. In this study, high-speed images were collected at a frame rate of  $180000 \text{ s}^{-1}$ . The B<sub>4</sub>C reinforcement particles served as natural speckles for DIC analysis. Snapshots of deformation process at various instants are presented in Fig. 11, along with the corresponding strain maps obtained with XDIC. It was shown in the XDIC results that samples with both weight ratios exhibited strain localization upon tensile loading. As the tensile loading continues, the stresses concentrated in a small area and caused damage in both cases. The sample with higher weight ratio exhibited more heterogeneity in strain distribution, experienced significantly more shear strain, and had an inclined strain localization area. This study also utilized the natural speckles produced by the B<sub>4</sub>C inclusions to perform XDIC analysis and showed the strain localization of B<sub>4</sub>C reinforced aluminum under dynamic tension.

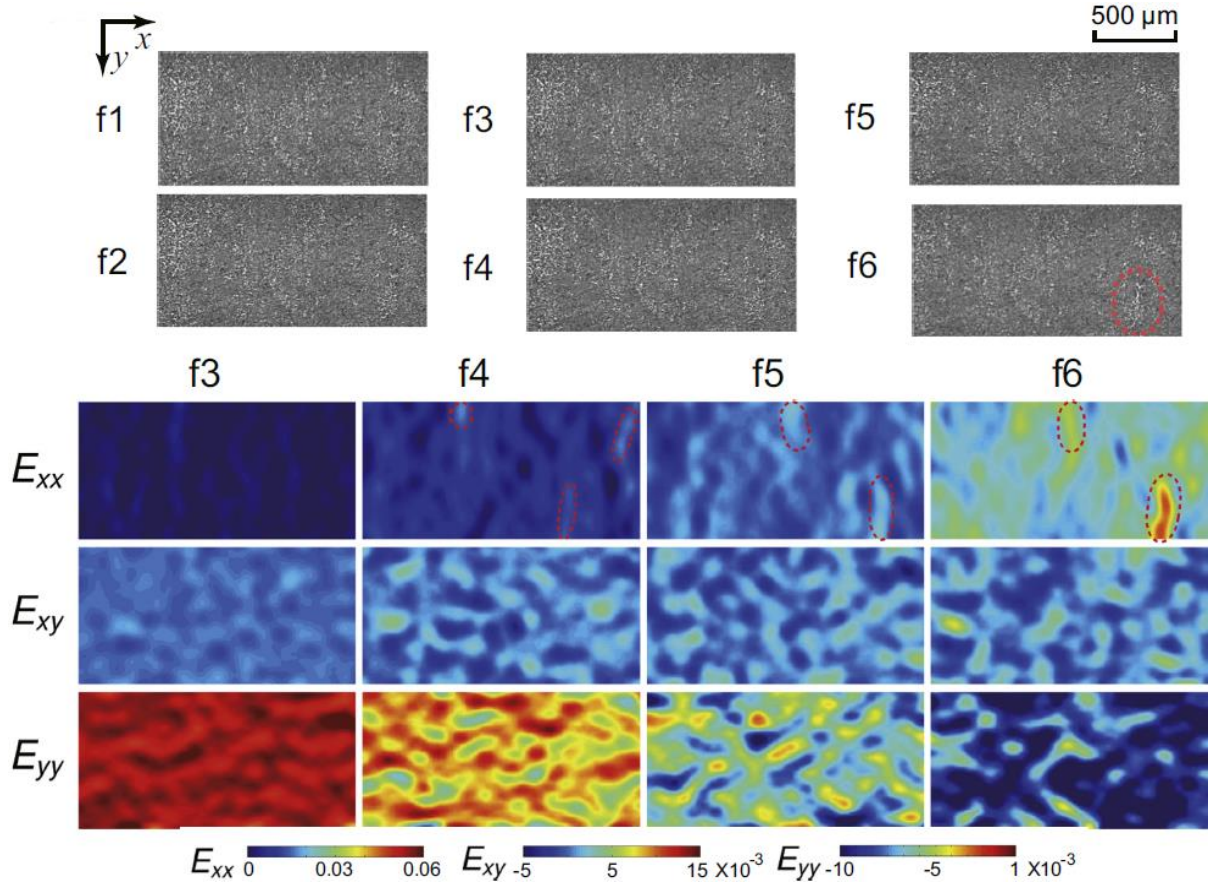


Figure 11. XPCI images and DIC results of sample under dynamic tension. The dashed ellipses mark strain localization sites [25].

As reflected in the recent works in the literature, the specimens of interest were naturally eligible for XDIC measurements. Although the case where glass beads were embedded in a transparent plate as speckles was shown viable, the applicability of XDIC in a study where particles are added as speckles to a transparent specimen when its dynamic response is of interest has not been assessed or discussed. Embedding particles in a material makes the material a composite and changes its properties. When conducting a study on a material that needs artificial speckles from embedded particles, it is crucially important to embed as few particles as possible while obtaining the best possible speckle pattern quality for XDIC measurement. So far, the application has not been extended into such a direction.



### 1.3 Synchrotron X-ray PCI

The XDIC method was developed based on the capability of synchrotron X-ray at APS Beamline 32-B at Argonne National Lab, Illinois. A synchrotron source maintains electron bunches in a storage ring. X-ray is emitted in the tangential direction by the electrons. In the experiments conducted for this work, 24 equidistant electron bunches were moving in a circular trajectory at the relativistic speed. An undulator in the storage ring was used to increase the X-ray intensity [26]. The undulator used was U18 (period: 18 mm, length: 2.4 m, number of periods: 133). The photon flux and the harmonic energy can be controlled by adjusting the gap between the two magnetic poles on the undulator. In the experiment conducted for this work, the gap size was set to be 13 mm. A 10 mm X 10 mm X 100  $\mu\text{m}$  scintillator (single crystal,  $\text{Lu}_3\text{Al}_5\text{O}_{12}:\text{Ce}$ ) is installed 25 cm downstream of the specimen field, converting the X-ray that passed through the specimen to optical light.

The phase contrast imaging at Beamline 32-B was obtained by an in-line holographic technique [27]. As X-ray passes through the sample, its phase changes can be caused by the materials that have different refractive indices. Such phase changes are the source of contrast in the images. The refractive index is given by  $n = (1 - \delta) + i\beta$ , where  $\beta$  and  $\delta$  are absorption and phase change, respectively. As the X-ray passes through a material with a small  $\beta$ , spatial phase change will be induced along with local curvature of the transmitted wavefront. As the X-ray travels from the specimen to the scintillator, the wavefronts overlap and interference causes its intensity being modulated. Edge enhancement is achieved from such intensity change, which is proportional to the Laplacian of the phase of X-ray.

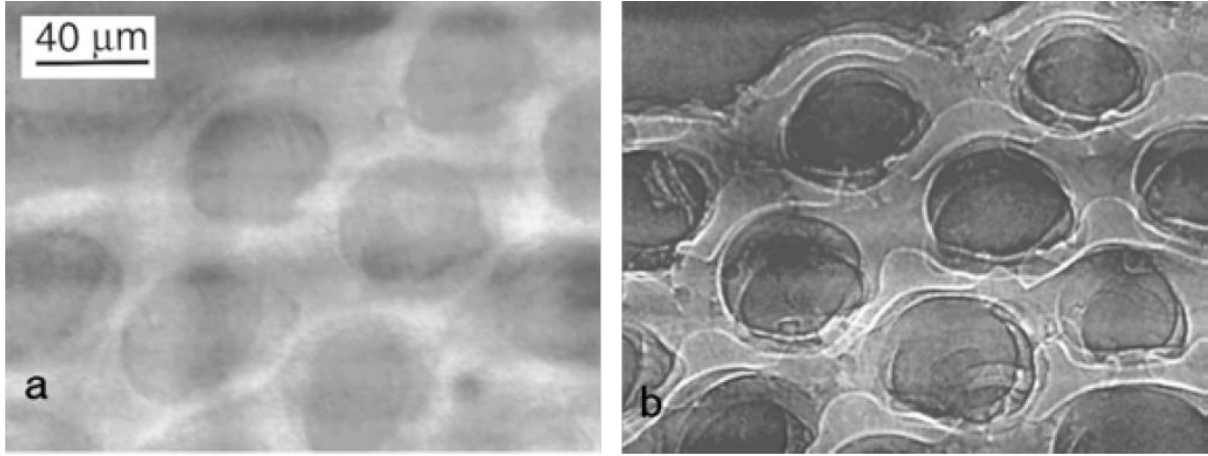


Figure 12. Comparison between PCI images a) without and b) with edge enhancement. The sample-detector distance is a) 0.5 cm and b) 25 cm [27].

Edge enhancement is crucially important for the purpose of this study as the applicability and quality of DIC measurement are directly affected by the quality of the images. Better contrast yields higher gradient value of intensity, which is inversely proportional to the viable subset size to maintain a constant measurement accuracy [24]. If the viable subset size is too big, spatial resolution cannot be achieved and the purpose of DIC measurement would be forfeited. An example of PCI images with and without edge enhancement is given in Fig. 12. As shown in the example, when the X-ray has not traveled enough distance to the scintillator to have the intensity modulated, the contrast is low and the boundaries of the features are blurry, making it difficult to apply DIC measurements.

#### 1.4 Research objectives

As reviewed earlier, the current works in the literature that utilized X-ray DIC all depended on the inherently viable speckle patterns of the material of interest under X-ray, and the method has not been developed to be applied to a transparent-under-X-ray material of interest with artificially added particles as speckles. The overall objective of this work is to assess the applicability of X-ray DIC on transparent materials with artificial speckles, and, if it is applicable, what the general standards are.

The initial drive of this study came from dynamic experiments on HMX crystals embedded in Sylgard® epoxy [16]. In the experiments, the deformation of the HMX crystal inside Sylgard® was of interest, but both Sylgard® and the HMX crystal were transparent under X-ray, with only

the boundaries of the HMX crystal being visible, as shown in Fig. 6. Therefore, it is extremely challenging to apply DIC measurements. It has been shown that it is possible to use artificial speckles, but how to implement this in a real study remains unknown.

In this study, 3 different types of powders were added to Sylgard® epoxy at various weight ratios. These samples were loaded with a Kolsky compression bar apparatus. The loading process was observed with X-ray PCI and the signal was transferred to optical light by the scintillator and recorded with a Shimadzu HPV-X2 ultra high speed camera. The quality for DIC measurements of the recorded results were assessed. The theoretical measurement errors were estimated with respect to measurement resolution, which is reflected as the subset size. The theoretically achievable resolution is also estimated based on target accuracy of 0.01 pixels. The measured deformation is calculated as displacement maps. These results will be displayed and discussed regarding the quality of measurements. Finally, the overall performances of the different powder materials as artificial speckles will be discussed.

## 2. EXPERIMENTAL METHODS

### 2.1 Materials and Sample Preparation

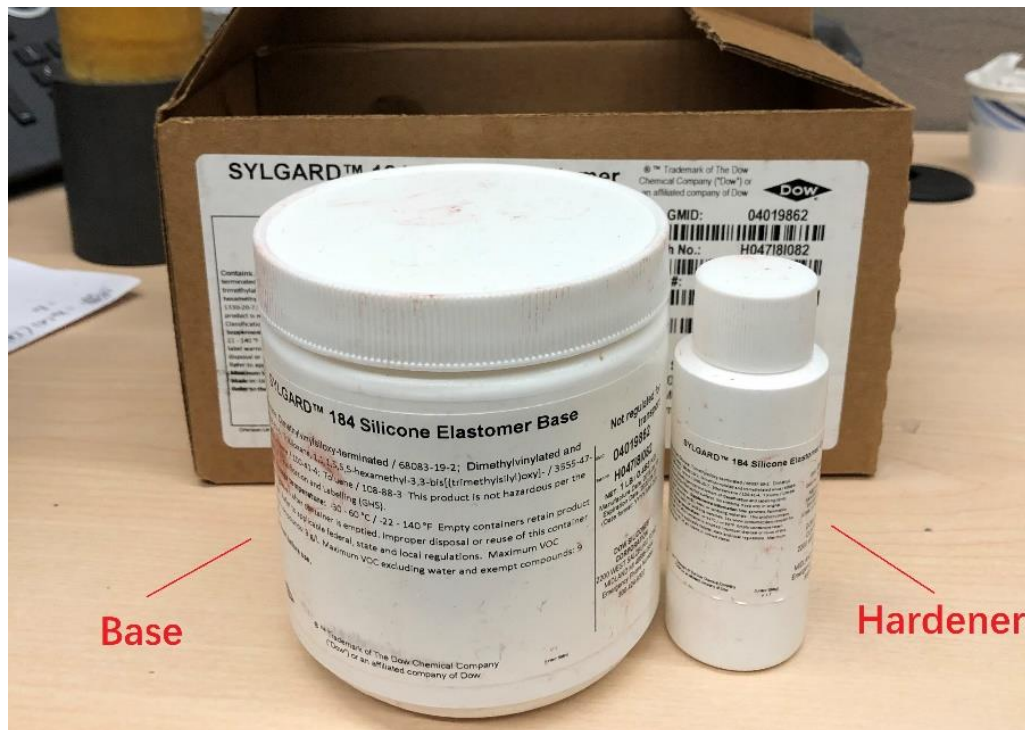


Figure 13. Commercially Available Sylgard®.

The material that was studied on the Kolsky compression bar is commercially available 2-part Sylgard® epoxy, as shown in Fig. 13. Since the original drive for this study is to explore a way to measure the deformation of HMX crystals, Sylgard® was chosen as the material to be studied. The cured Sylgard® epoxy is an elastic polymer under room temperature. It is transparent unless particles are added. All types of powder materials used in this study make Sylgard® epoxy opaque. To make Sylgard® samples, the base and the hardener were mixed together at weight ratio 10:1. The mixture was then placed in vacuum for degassing. After the mixture has been degassed, the powder of measured weight was added to the mixture. This was again well mixed and degassed in a vacuum chamber. The mixture with powder added was poured in a rectangular stainless steel mold, as shown in Fig. 14. The mold consists of a top stainless steel plate with  $\frac{1}{2}$ " diameter holes and a base made of high density polyethylene block. The two parts are combined using the  $\frac{3}{16}$ " bolts and nuts. At the bottom of each cylindrical hole, there is a 2 mm X 2 mm X 1 mm slot on the

plastic base, where the actual sample will be molded. The steel mold containing the mixture was degassed once again and set in an environment chamber at 90 °C for 10 hours. After the mixture was cured, it was removed from the mold and the small rectangular portion was cut from the cylindrical portion, as presented in Fig. 15. These small portions were stored and were to be placed in the sample holder before being loaded on a Kolsky bar.

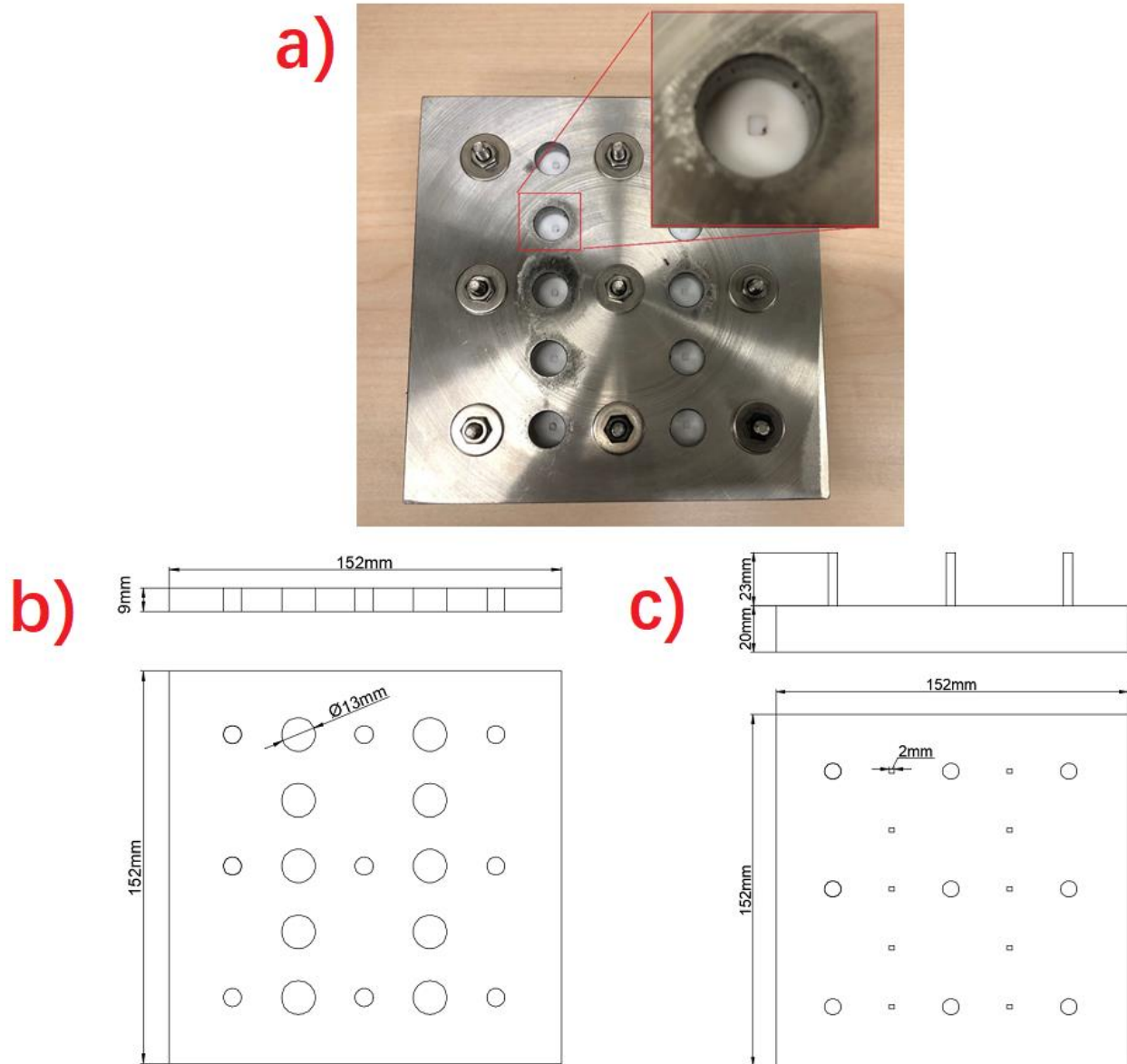


Figure 14. a) A picture, b) a schematic of the stainless-steel mold top, and c) a schematic of the plastic mold base.

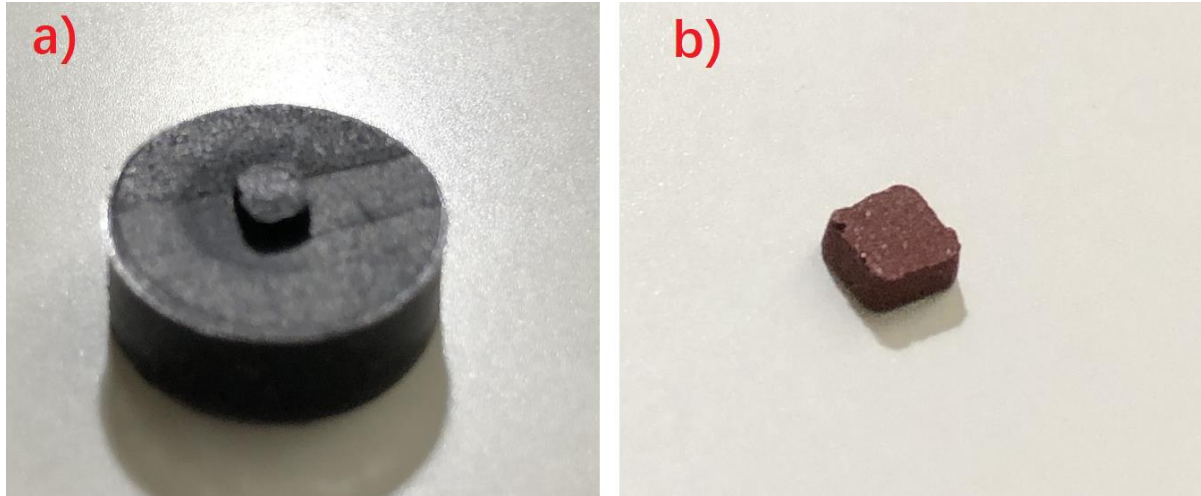


Figure 15. a) Sylgard® cylinder with WC, removed from the mode. b) Sample of Sylgard® with FeO cut from the cylinder.

The sample holder has a sandwich structure. A schematic along with the dimensions of the sample holder is given in Fig. 16. The middle plate is made of aluminum and is the main supporting part, which transmits the loads from the sample to the load cell. A 1 mm thick PMMA plate is attached to the aluminum plate from its each side, which serves the purpose of constraining the sample horizontally. The outer PMMA plates and the inner aluminum plate were assembled using 4 3/16" bolts and nuts. The sample shown in the picture was not used for experiment due to irregular shape. During the experiment, the sample holder was mounted onto an aluminum gripper, which is connected to the load cell using a setscrew. The schematic of the gripper is also presented in Fig. 17. The width of the opening is slightly larger than the thickness of the sample holder such that the holder can slide in and out of the gripper.

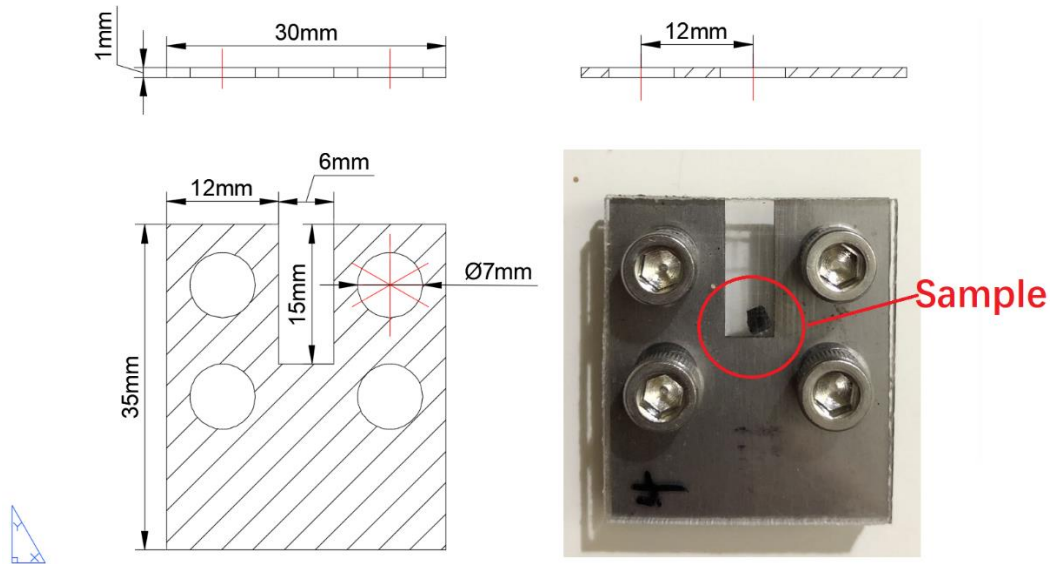


Figure 16. A schematic and a picture of the sample holder.

During the experiment, the sample was compressed via a stainless steel plunger, which is screwed onto the incident bar. The position of the sample mount was adjusted such that the plunger can freely slide in and out of the slit and is just in touch with the sample.

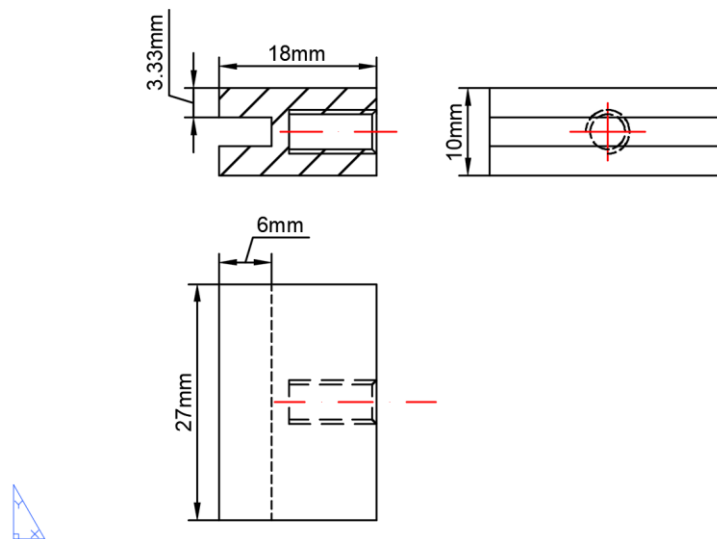


Figure 17. Schematic of the sample gripper.

## 2.2 Types of Particles

Table 1. All Types of Added Particles.

Particle Material	Iron Oxide (FeO)	Tungsten Carbide (WC)	Platinum (Pt)
Weight Ratio	4%	4%	5%
	7%	7%	
	10%	10%	
	13%	13%	

Three different granular materials were used as the artificial speckles in the Sylgard® epoxy. These are iron oxide powders, tungsten carbide powders, and platinum powders. They were added to the epoxy at various weight ratios. The information of all the combinations is given in Table. 1. In earlier dynamic study on HMX crystal embedded in Sylgard®, a very small amount of iron oxide particles (0.25%) were added as cursor particles. It was shown to produce a particulate pattern but was too scarce to produce a consistent speckle field. Therefore, it was selected with an increased amount for a candidate particle. However, the refractive index of iron oxide is not optimal. In another word, in the PCI images, the iron oxide particles are not dark enough to produce the highest contrast. Two other materials with higher refractive indices were selected as competing candidates. Platinum particles have the best refractive index and produce the highest possible contrast. One of the disadvantages is that the platinum particles are very costly. Another disadvantage is that Platinum tends to react with polymer matrices, making it difficult to apply in studies on polymer matrix materials. Due to limited availability, only 5% by weight ratio was tested for platinum. Also, the purpose of choosing Platinum is to use the result as a referential case as it is expected to produce the optimal speckle pattern. By comparing to the platinum results, it is easier to make a judgement on the speckle quality. Tungsten carbide particles have slightly lower refractive index than platinum, also exhibiting dark particulate pattern in the PCI images. It was selected as a main competing candidate and was studied at 4 different weight ratios.

Another factor that affects the quality of the speckle pattern is the way these particles are distributed inside the epoxy. Since the X-ray PCI does not have resolution in the direction it travels, what is seen in the PCI images can be thought as a stack of tomography images that overlap with each other. It is essentially a 2-D projection of the everything inside the 3-D object. Therefore, an ideal speckle pattern requires even distribution of small particles throughout the region of interest, such that the particles overlap to form a dense pattern but do not overlap too much to appear



connected to each other and form a cluster in the PCI images. In the sample preparation process, the platinum particles were added with special caution and were made sure to be added after the two parts of Sylgard® were well mixed, because platinum particles were found to react with the hardener, and formation of platinum clusters should be avoided.

### **2.3 Kolsky Compression Bar Apparatus**

In this study, the experiments were conducted with a miniature Kolsky compression bar apparatus at Argonne APS Beamline 32-B, as shown in Fig. 17. This experimental setup along with the X-ray PCI has been used in a wide range of studies, including failure mechanism of particles [28]-[30], fiber-reinforced composite [31], high-performance fibers [32], skull bone failures [33], etc. The Kolsky compression bar apparatus is typically used in dynamic experiments at high strain rate ( $10^2$  to  $10^5$  s<sup>-1</sup>) [34]. As illustrated in Fig. 18, this Kolsky bar is consist of a high-strength steel striker (diameter = 12.7 mm, length = 305 mm) and a high-strength steel incident bar (diameter = 12.7 mm, length = 1372 mm). Unlike a typical Kolsky compression bar apparatus, this setup does not include the transmission bar. Instead, the load cell is directly mounted onto a backstop at the other side of the sample. A 3 V DC signal is sent to a zero-pass solid-state relay to trigger a fast-open solenoid. The solenoid then releases the pressed air from the gas tank to launch the striker. The input pressure used in this study was consistently 10 psi.

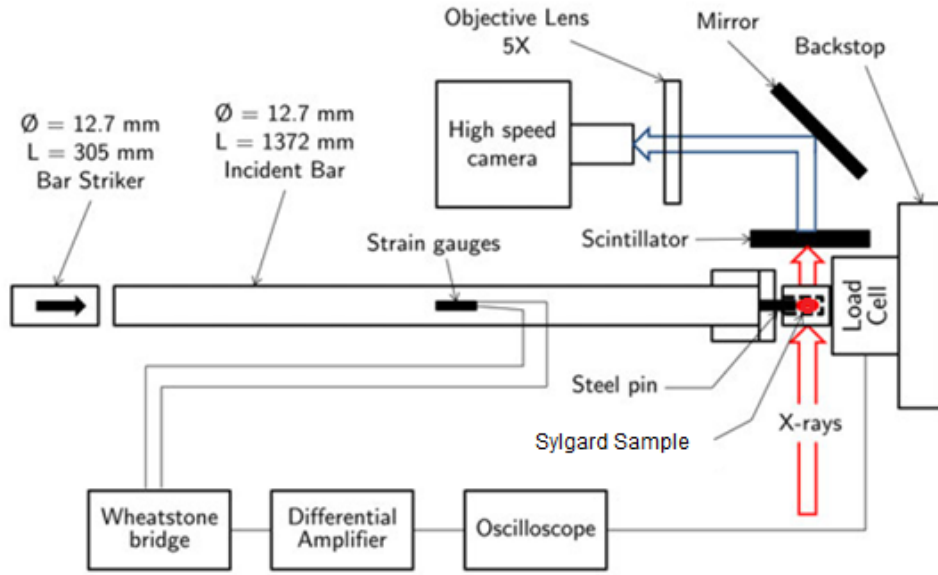


Figure 18. A Schematic of Kolsky Bar Apparatus at Beamline 32-B.

In Kolsky bar experiments, it is in general assumed that dynamic stress equilibrium is maintained inside the sample and that the deformation of the sample is uniform in order to obtain viable measurements. For a soft material such as Sylgard®, it can be challenging that these two assumptions are met due to the low characteristic wave speed. It has been reported that elastomers during Kolsky compression bar experiments commonly exhibit non-uniform deformation [35]. One way to tackle the challenge is to ramp up the incident strain at lower rate, allowing stress equilibrium to form inside the sample. It is proposed that 100  $\mu$ s should be allowed for the strain to ramp up as a rule of thumb [36]. This is achievable using pulse shaping techniques. To decelerate the wave as it is transmitted to the incident bar, a material that is softer than the incident bar was sought to serve as a pulse shaper, which was attached at the front end of the incident bar. With the pulse shaping materials available, round rubber plates were found to alter the incident strain such that it has  $\sim 94$   $\mu$ s of ramp-up time. This method is used in all the experiments served as material response characterization. The pulse shapers are not used in the XPCI experiments to match the loading condition in previous work with Sylgard® [16].

Two semi-conductor strain gauges are attached onto the incident bar diametrically and are connected to a half Wheatstone bridge and a pre-amplifier. The incident and reflected waves in the

incident bar are recorded by the gauges via the oscilloscope (Tektronix, DPO7104C Beaverton, Oregon), which also collects the signal from the load cell. The bar speed can then be calculated from the strain:

$$v(t) = C_B(\epsilon_i(t) - \epsilon_r(t))$$

where  $C_B$  denotes the wave velocity of the bar,  $\epsilon_i$  and  $\epsilon_r$  denotes the incident and reflected strain, respectively. The compression speed of the bar is calculated as around 6 m/s, which is consistent with all the other studies done with this apparatus.

The strain rate in the sample can be calculated as

$$\dot{\epsilon} = \frac{C_B}{L_s}(\epsilon_i - \epsilon_r)$$

which can be integrated to find the strain in the sample as

$$\epsilon = \int \frac{C_B}{L_s}(\epsilon_i - \epsilon_r)dt.$$

## 2.4 X-ray Control

The X-ray was controlled by two water cooled copper block shutters. The purpose of have the shutter system is to protect the samples and device from the damage cause by over-exposure under high-energy X-ray. The opening and closing time of the shutters are approximately 50 ms. In a typical dynamic experiment, the shutter opening, high-speed camera recording, and the Kolsky bar firing are synchronized using a delay generator (DG 535, Stanford Research Systems, Sunnyvale, CA). The synchronization scheme is shown in Fig. 19. At  $t_1$ , the manual signal was sent to the solenoid to launch the striker. A delayed signal was sent to open the shutter at  $t_2$ , which completed the opening at  $t_3$ . The strain gauge signal was received at  $t_4$ . After a short delay, the high-speed camera started recording the loading process at  $t_5$ . After the loading process (approximately 15 ms), the shutter started to close at  $t_6$ , and finished the process at  $t_7$ .

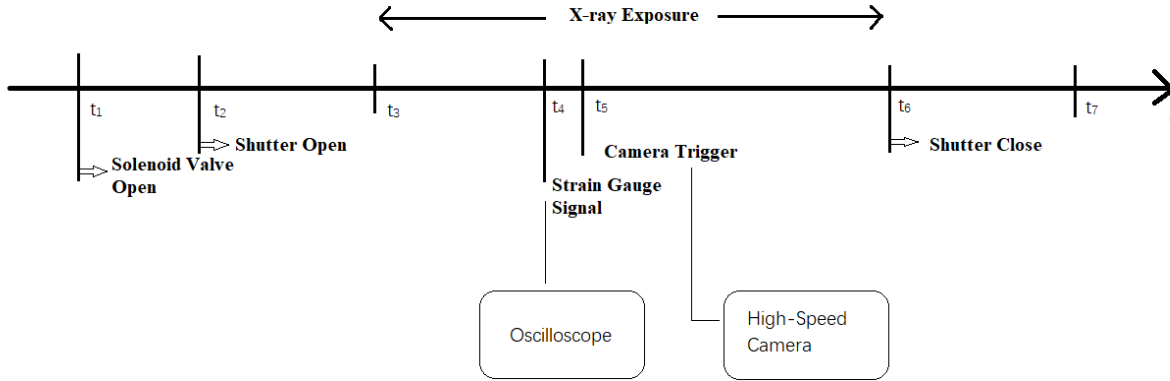


Figure 19. Synchronization Scheme of the X-ray and Kolsky Bar Apparatus.

## 2.5 Digital Image Correlation

The digital image correlation measurement scripts used in this study were independently written. The program followed the same theories and algorithm as what is frequently seen in the literature. In DIC, a subset grid is first defined for the reference frame. For each subset in the reference frame, the algorithm searches for a subset of the same size near the same pixel location in the deformed frame to match the subset in the reference frame. The searching range is predefined based on expected range of deformation in pixels. The degree of match is determined by correlation coefficients between two subsets. The correlation coefficient is computed using the greyscale intensities of all the pixels in both subsets. If the subsets in both frames reflect the same portion of the object, the correlation coefficient is either maximum or minimum depending on the method of calculation. Knowing the location of this subset in the deformed frame, the integer pixel displacement of that portion of the object can be calculated as the difference from the subset location in the reference frame. Looping this process throughout the region of interest produces an integer displacement map. There are multiple types of correlation coefficient schemes [21]. A list of them is given in Table. 2. In general, the normalized formulas can account for linear variations of the grey level intensity, which is suitable for this study because the intensity fields are not stable across frames. In specific, zero normalized sum of squared difference (ZNSSD) scheme was used in this study.

Table 2. Commonly Seen Correlation Schemes.

Correlation Criterion	Definition
Cross-correlation	$C_{CC} = \sum_{i=-M}^M \sum_{j=-M}^M [f(x_i, y_j)g(x'_i, y'_j)]$
Normalized Cross-correlation	$C_{NCC} = \sum_{i=-M}^M \sum_{j=-M}^M \left[ \frac{f(x_i, y_j)g(x'_i, y'_j)}{\bar{f}\bar{g}} \right]$
Zero-Normalized Cross-correlation	$C_{ZNCC} = \sum_{i=-M}^M \sum_{j=-M}^M \left\{ \frac{[f(x_i, y_j) - f_m][g(x'_i, y'_j) - g_m]}{\Delta f \Delta g} \right\}$
Sum of Squared Difference	$C_{SSD} = \sum_{i=-M}^M \sum_{j=-M}^M [f(x_i, y_j) - g(x'_i, y'_j)]^2$
Normalized Sum of Squared Difference	$C_{NSSD} = \sum_{i=-M}^M \sum_{j=-M}^M \left[ \frac{f(x_i, y_j)}{\bar{f}} - \frac{g(x'_i, y'_j)}{\bar{g}} \right]^2$
Zero-Normalized Sum of Squared Difference	$C_{ZNSSD} = \sum_{i=-M}^M \sum_{j=-M}^M \left[ \frac{f(x_i, y_j) - f_m}{\Delta f} - \frac{g(x'_i, y'_j) - g_m}{\Delta g} \right]^2$

In Table 2,  $f$  and  $g$  are the reference and deformed frame, respectively, in which  $x$  and  $y$  are the vertical and horizontal coordinates, respectively.  $M$  denotes the one half size of the subset, in which  $i$  and  $j$  are the vertical and horizontal index of a pixel, respectively. In the normalized schemes,

$$\bar{f} = \sqrt{\sum_{i=-M}^M \sum_{j=-M}^M [f(x_i, y_j)]^2},$$

$$f_m = \frac{1}{(2M+1)^2} \sum_{i=-M}^M \sum_{j=-M}^M f(x_i, y_j),$$

$$\Delta f = \sqrt{\sum_{i=-M}^M \sum_{j=-M}^M [f(x_i, y_j) - f_m]^2},$$

and similarly for  $g$ .

### 2.5.1 Sub-pixel Registration

The information stored in digital images is not continuous, but rather discretely stored on each pixel. Thus, the direct search method, for example the ZNSSD scheme, only yields integer pixel displacement. However, the pixels represent finite portions of the object. The points on the object may not fall into exact pixel positions after deformation in the target frame. If only direct search method is used, only integer pixel accuracy is achieved, which is much less compared to bulk measurements methods such as strain gages. To achieve sub-pixel accuracy, the space between pixel points in the target frame must be filled first. In this study, the sub-pixel information is registered using a bicubic curve fitting algorithm. For any four adjacent pixels that form a square, the grey level intensity of any point inside this square can be interpolated as

$$g(x, y) = \sum_{m=0}^3 \sum_{n=0}^3 a_{mn} x^m y^n$$

where  $x$  and  $y$  are the normalized local coordinates inside the square from 0 to 1, and  $a_{mn}$  are the bicubic coefficients. The coefficients were calculated based on the grey level intensity of the four pixels, the estimated gradients of intensity at the four pixels, and the estimated Hessian at the four pixels (total of 16 values to yield 16 coefficients). The estimation was based on a central difference scheme.

### 2.5.2 Sub-pixel Search Algorithm

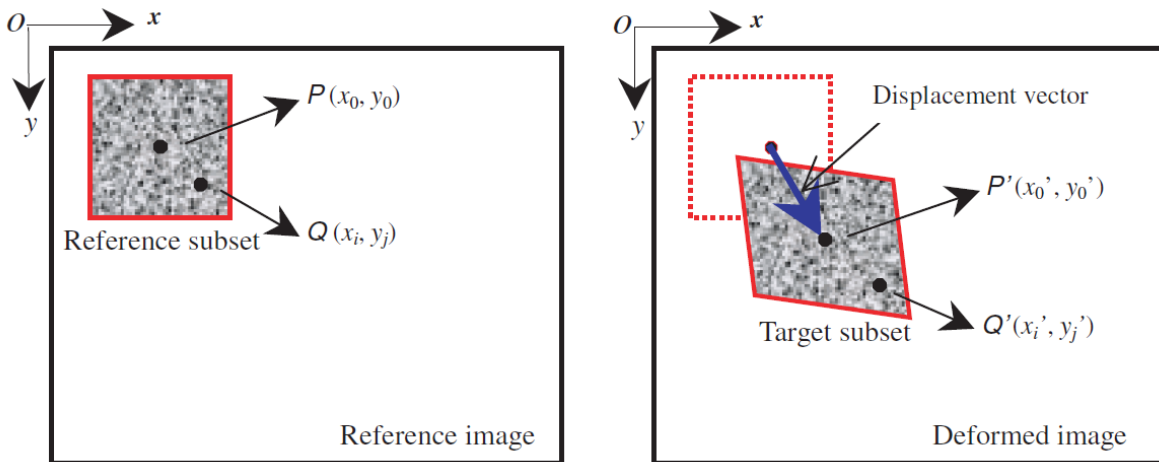


Figure 20. Mapping of points in a subset from reference image to deformed image [21].

The searching at sub-pixel level followed a Newton-Raphson scheme [37]. For every pixel in the reference frame, there is a one-to-one mapping point in the target (deformed) frame by the deformation—as shown in Fig. 20—such that

$$f(x, y) = g(x^*, y^*)$$

where  $f$  and  $g$  are reference and target frame, respectively.  $x^*$  and  $y^*$  are the spatial position of the pixel  $(x, y)$  from the reference frame in the target frame. By definition, this position is

$$\begin{aligned} x^* &= x + u(x, y), \\ y^* &= y + v(x, y). \end{aligned}$$

Define the center of a subset as  $(x_0, y_0)$ , and the distance from any point in the subset to the center as  $(\Delta x, \Delta y)$ , then the first-order Taylor expansion approximation of the mapped position of any point in a subset of reference frame is

$$\begin{aligned} x_i^* &= x_0 + \Delta x_i + u + u_x \Delta x_i + u_y \Delta y_i, \\ y_i^* &= y_0 + \Delta y_i + v + v_x \Delta x_i + v_y \Delta y_i \end{aligned}$$

where subscript  $i$  stands for the pixel index with respect to that subset. Subscript  $x$  and  $y$  stand for the gradient components of the displacements.  $u$  and  $v$  are the displacements at the center of the subset.

In this study, when two subsets from the reference and target frame match the one-to-one mapping, the calculated correlation coefficient must be at minimum for ZNSSD scheme. Since the correlation coefficient has become a function of the spatial coordinates of the subset now that the sub-pixel registration was done, finding its location becomes an optimization problem. This is where the Newton-Raphson scheme can be applied.

Let a vector  $p$  denote the deformation information  $[u, u_x, u_y, v, v_x, v_y]$ , the correlation coefficient is therefore a function of  $p$ . At the extrema, the gradient of the correlation coefficient,  $\nabla C$ , must be 0. According to the NR scheme,

$$\begin{aligned} \nabla C(\mathbf{p}^{k+1}) &= \nabla \nabla C(\mathbf{p}^k)(\mathbf{p}^{k+1} - \mathbf{p}^k) + \nabla C(\mathbf{p}^k) = \mathbf{0}, \\ \mathbf{p}^{k+1} &= \mathbf{p}^k - \frac{\nabla C(\mathbf{p}^k)}{\nabla \nabla C(\mathbf{p}^k)}. \end{aligned}$$

Here, the Hessian of the correlation coefficients is needed in the iterative process. Both the gradient and the Hessian can be estimated to drastically save computation time [27].

$$\nabla C(\mathbf{p}) = -2 \sum_{i=0}^M \sum_{j=0}^N \left\{ \left[ \frac{f(x_i, y_j) - f_m}{\Delta f} - \frac{g(x_i^*, y_j^*) - g_m}{\Delta g} \right] \frac{\nabla g(x_i^*, y_j^*)}{\Delta g} \right\},$$

$$\nabla\nabla C(\mathbf{p}) = 2\sum_{i=0}^M\sum_{j=0}^N \left[ \frac{1}{(\Delta g)^2} \nabla g(x_i^*, y_j^*)^T \nabla g(x_i^*, y_j^*) \right].$$

For an iterative solution method, an initial guess is needed. The integer pixel displacement result from the direct search were used as initial guesses in this study. The answer is found as  $\mathbf{p}$  converges.

### 2.5.3 Mean Intensity Gradient (MIG)

Qualitatively, the DIC measurements yield higher accuracy and finer resolution when the speckle patterns in the images are finer and have higher contrast. This has been experimentally shown and a quantity has been defined to quantitatively express how good the speckle quality is in contribution to an accurate measurement [24]. Intuitively, if the speckles have high contrast and fine pattern, the total gradient calculated across the entire intensity field should be higher than that calculated for coarser pattern with lower contrast. Therefore, higher total intensity gradient means better speckle pattern. To make it a consistent measure that disregard of the size of the images, the total intensity gradient shall be normalized with respect to the image size and become mean intensity gradient factor, given as

$$\delta_f = \sum_{i=1}^W \sum_{j=1}^H |\nabla f(\mathbf{x}_{ij})| / (W \times H)$$

where  $W$  and  $H$  stand for the width and height of the image, respectively, and  $\mathbf{x}_{ij}$  is the spatial coordinates of the pixels.

In this study, the grey-level intensity was normalized. to compare those frequently seen in the literature, the intensity value has been scaled by 255, which corresponds to the maximum intensity value in an 8-bit format. The mean intensity gradient factor is also a good indicator for achievable resolution. From a qualitative point of view, if the speckle pattern is finer, the measurable feature would also be finer. The relationship can be quantified in theoretical error analysis.

Figure 21 shows a list of speckles reported in [24]. It was reported that the measured error in the last speckle (MIG=9.04) is significantly greater than the rest of listed speckles, almost doubling the second greatest error with MIG equal to 12.34, albeit only increased by 3.3. An ad



hoc standard can be estimated to serve as a guideline of speckle quality, that a speckle with MIG greater than 10 would produce acceptable DIC analysis. It is also reported that a high-rate XPCI image with MIG around 22 can be considered of excellent quality [25].

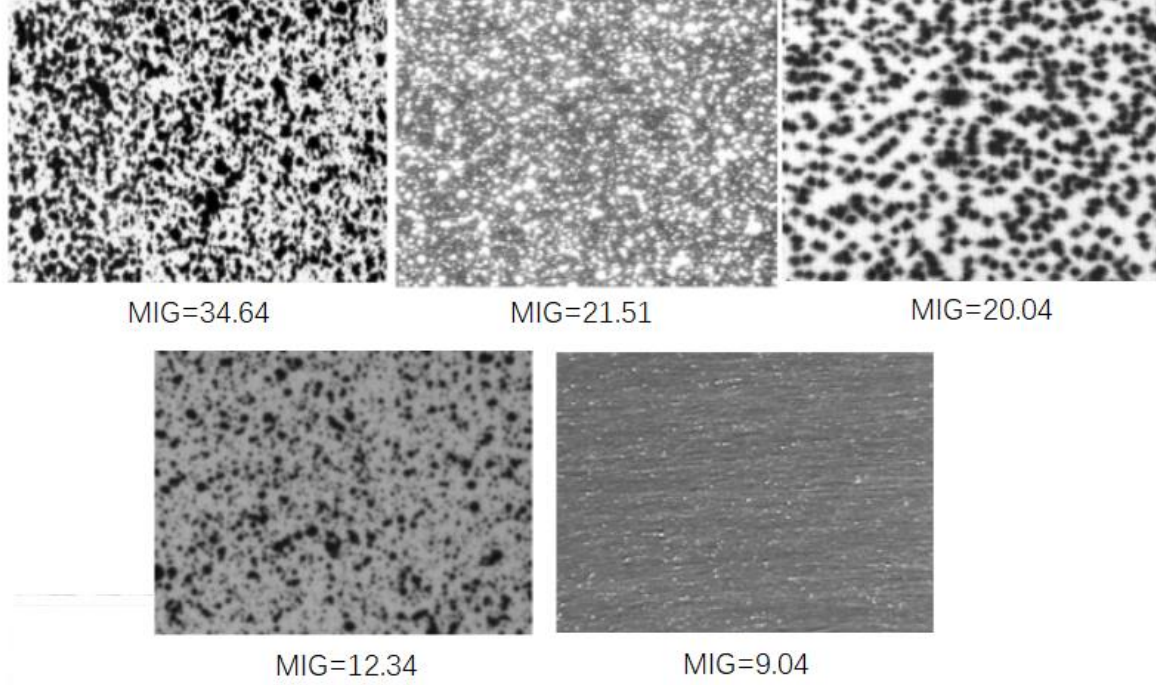


Figure 21. A list of speckles with decreasing MIG [24].

#### 2.5.4 Theoretical Error Estimation

The theoretical error of a DIC measurement depends on the Gaussian noise, the subset size and the mean intensity gradient. In a measurement, some part of the image may be measured more accurately than others, and the overall error varies spatially. Therefore, the theoretical error is defined as the standard deviation of measured displacement of a subset with respect to the true displacement:

$$std(u_e) \cong \frac{\sqrt{2}\sigma}{\sqrt{\sum_{i=1}^N \sum_{j=1}^N [f_x(\mathbf{x}_{ij})]^2}}$$

where  $\sigma$  is the Gaussian noise. What this error physically means is the deviation at each pixel As reflected in the summation, this formulation is specific to square subsets, which were consistently

used in this study. The deviation error is inversely proportional to the local mean intensity gradient at a given subset size. Similarly, for a given level of error, the minimum achievable subset size is also inversely proportional to the local intensity gradient. For dynamic studies, the resolution is very important. Therefore, a high level of intensity gradient is desired.

To transform the local analysis of theoretical error to a global parameter, the global intensity gradient is related to the subset size via an approximation:

$$\sqrt{\sum_{i=1}^N \sum_{j=1}^N [f_x(\mathbf{x}_{ij})]^2} \cong N\delta_f.$$

Write in term of deviation error,

$$std(u_e) \cong \frac{\sqrt{2}\sigma}{N\delta_f}.$$

### 3. RESULTS AND DISCUSSION

#### 3.1 Bright Field Correction

The brightness of the X-ray in the center of the images is higher than the rest of the images, thus the intensity is not uniform within each image. Therefore, before any DIC analysis was done, a bright field adjustment was introduced to correct this feature. For any frame, the intensity of all the pixels was corrected as:

$$I_c = \frac{I(x, y)}{I_0(x, y)} I_0^*$$

where  $I$  denotes the intensity of the original frame and  $I_0$  denoted the intensity of an PCI image taken with no sample being mounted—a background image. The  $I_0^*$  term is the mean value of the intensity across the background image. A comparison of the uncorrected and corrected images is given in Fig. 22. It can be seen that the brightness is much more even on the corrected images, whereas the center seems brighter in the uncorrected one.

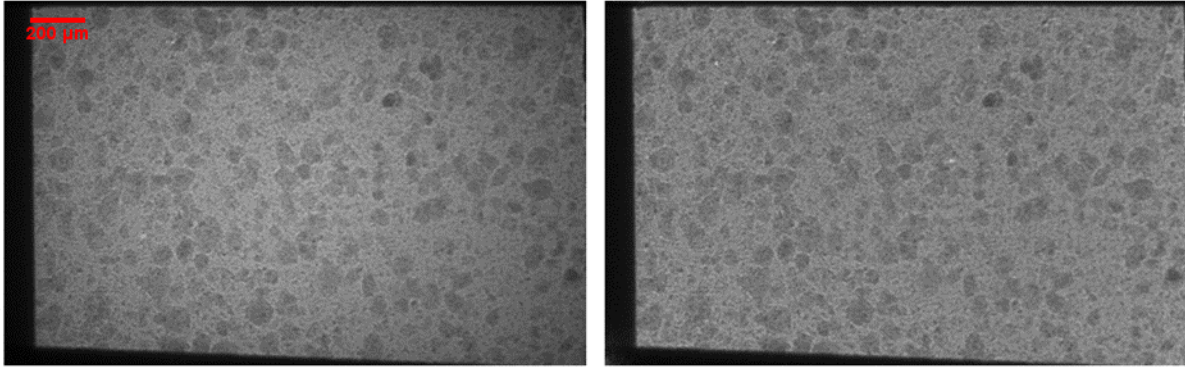


Figure 22. Comparison between a) uncorrected and b) corrected XPCI images of Sylgard® with 13% FeO.

#### 3.2 Phase Contrast Imaging Results

Selected frames of X-ray PCI frames after bright field correction are first shown for each sample configuration. The Quality of the speckles are then assessed, the subset size required based on 0.01-pixel accuracy calculated, and the theoretical error based on 25 X 25 pixels subsets evaluated. The DIC measurements in displacements are then provided. The subset sizes used are

of similar value as those calculated in the theoretical error estimation. The discussion on the results is provided afterwards.

In a dynamic experiment on an elastomer sample, it is expected that the sample goes through a large strain. During this deformation process, the overall speckle quality may change due to compaction of particles and overlapping of particles in different planes. Therefore, the quality of speckles in term of mean intensity gradient is calculated throughout the impact process. The mean intensity gradient is averaged over the entire area, but the dark borders should not be taken into account for speckle quality assessment. Therefore, only a region of interest is evaluated for mean intensity gradient for each frame for all the experiments.

The region of interest is selected as a rectangle whose sides are a few pixels into the sample region away from the dark borders, The reason why the outer-most layer of the sample is not considered inside the region of interest is that, this layer of material experienced non-negligible deformation in the X-ray direction, which makes the measurement invalid. Also, the deformation specifically at the boundary layer is not of interest in this study. The thickness of the outer layer was decided based on an ad hoc standard that depends on the observation on the PCI images. This standard was applied throughout all the experiments.

### **3.2.1 FeO Inclusions at 4% Weight**

Representative images of Sylgard® with 4% of FeO particles during the process of being compressed are presented in Fig. 23. The region enclosed by the red box is the region of interest in each frame. The box follows the deformation of the sample and evolve across frames. Figure 24 shows the mean intensity gradient change during the impact process. The significance of the values of the mean intensity gradient is discussed after all PCI results are presented.

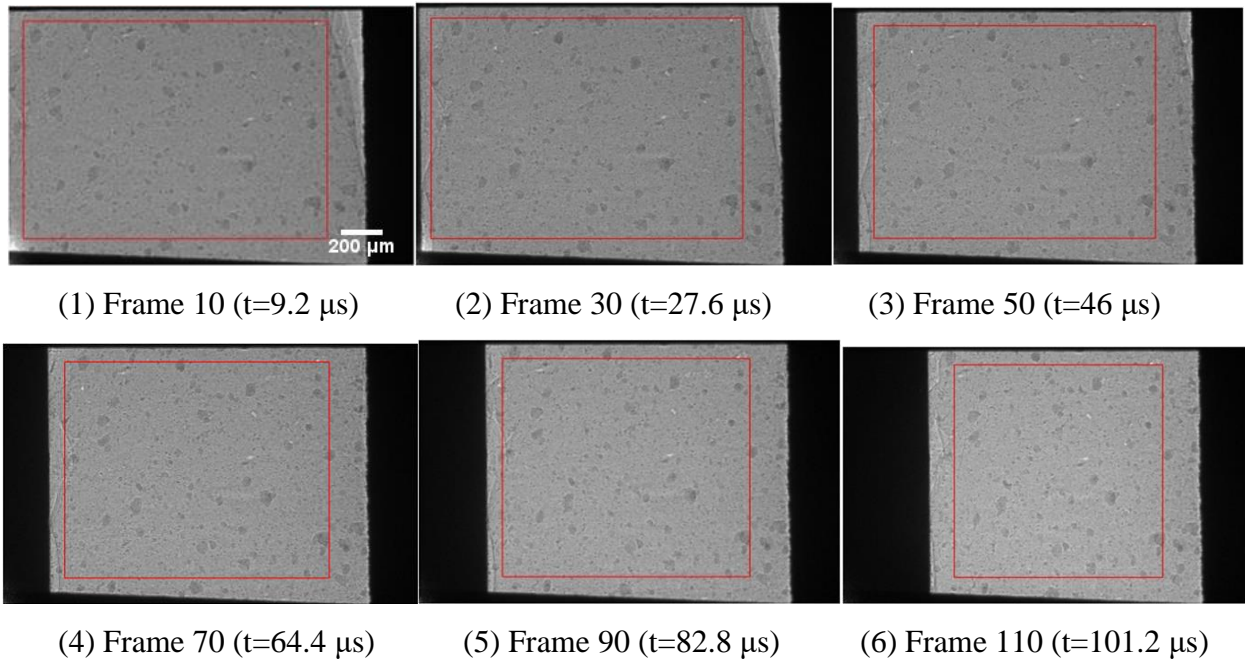


Figure 23. Sylgard® with 4% FeO particles under impact.

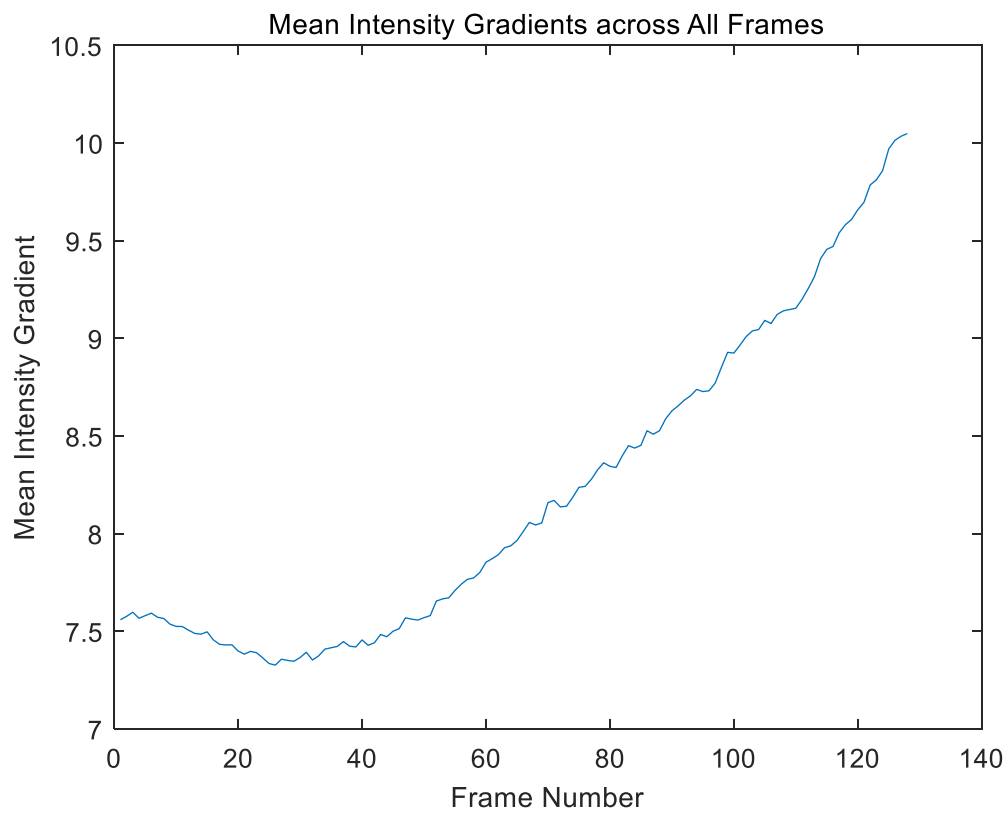


Figure 24. Mean Intensity Gradient Change during the Impact Process, 4% FeO.

From a qualitative point of view, the speckles include large number of small particles and small amount of particle clusters. As shown in Fig. 25, the normalized gray level distribution of the particles concentrates towards the middle gray region. This means that the colors of the particles as well as the matrix are alike, and the level of uniqueness of the particle colors is relatively low. The quality of speckles stayed relatively constant during the first 40 frames, where only a small deformation was seen, then slowly ramped up to 133% as the particles are squeezed to be closer to each other.

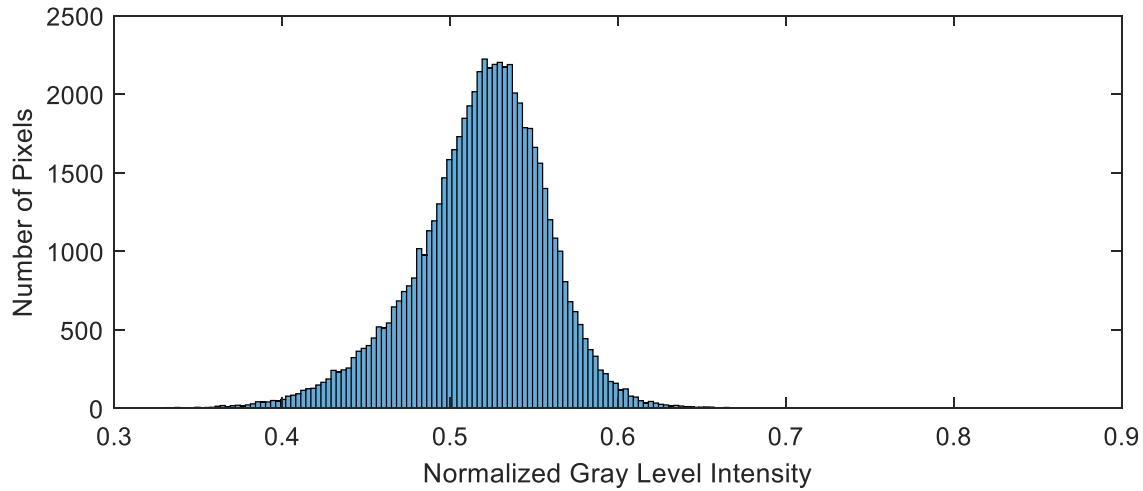


Figure 25. Gray Level Intensity Distribution in the 4% FeO Sample Image.

### 3.2.2 FeO Inclusions at 7% Weight

Representative images of Sylgard® with 7% of FeO particles during the process of being compressed are presented in Fig. 26. The region enclosed by the red box is the region of interest in each frame. Figure 27 shows the mean intensity gradient change during the impact process.

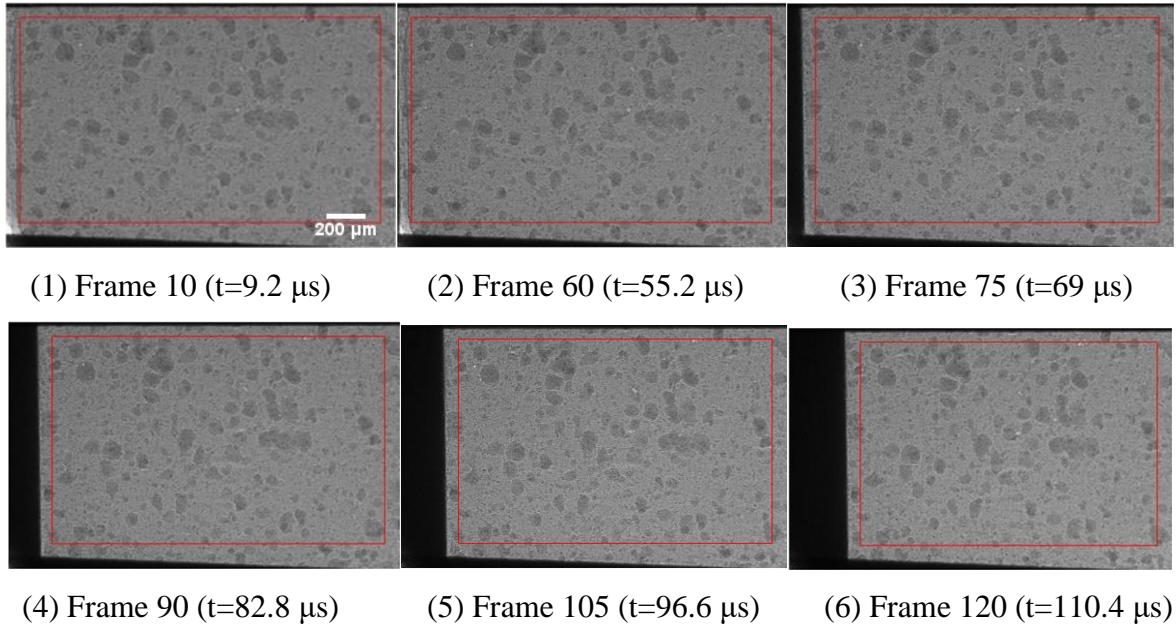


Figure 26. Sylgard® with 7% FeO particles under impact.

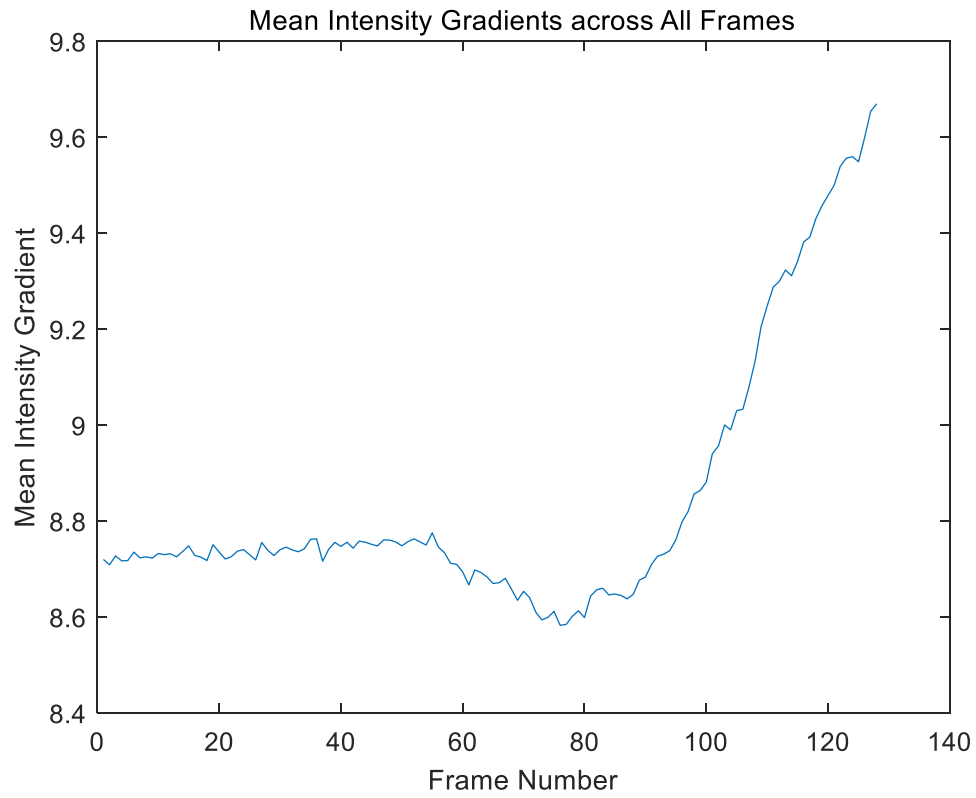


Figure 27. Mean Intensity Gradient Change during the Impact Process, 7% FeO.

By adding 3% of FeO particles, the numbers of both small particles and large clusters increased. As shown in Fig. 28, the normalized gray level distribution of the particles concentrates less towards the middle gray region and spreads out a bit. Although, most of the normalized intensity is still distributed in the 0.4-0.55 region. In this specific experiment, the sample was not compressed until around frame 60 (55.2  $\mu$ s). As the sample starts being compressed, the mean intensity gradient showed the same trend, slightly decreasing before ramping up. Possibly due to the short compression time, the value only increased by  $\sim 1$ .

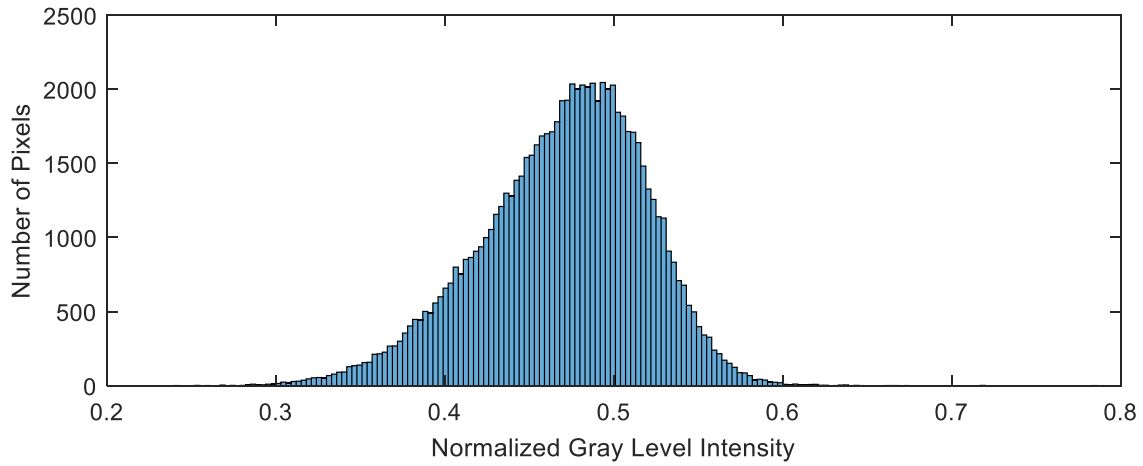


Figure 28. Gray Level Intensity Distribution in the 7% FeO Sample Image.

### 3.2.3 FeO Inclusions at 10% Weight

Representative images of Sylgard® with 7% of FeO particles during the process of being compressed are presented in Fig. 29. The region enclosed by the red box is the region of interest in each frame. Figure 30 shows the mean intensity gradient change during the impact process.



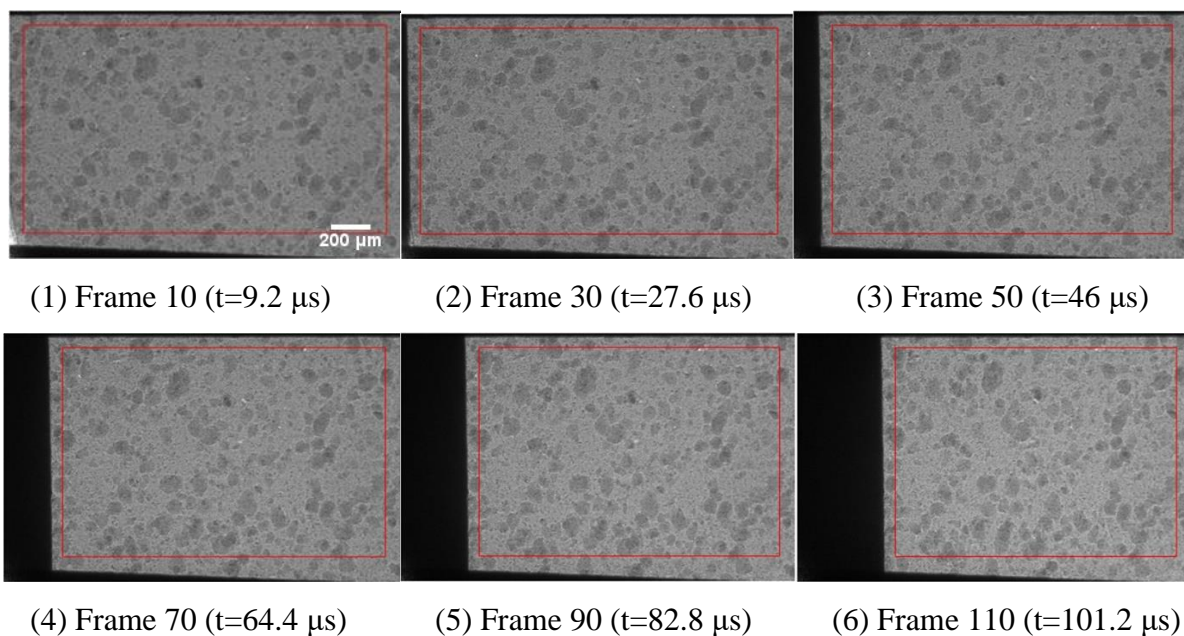


Figure 29. Sylgard® with 10% FeO particles under impact.

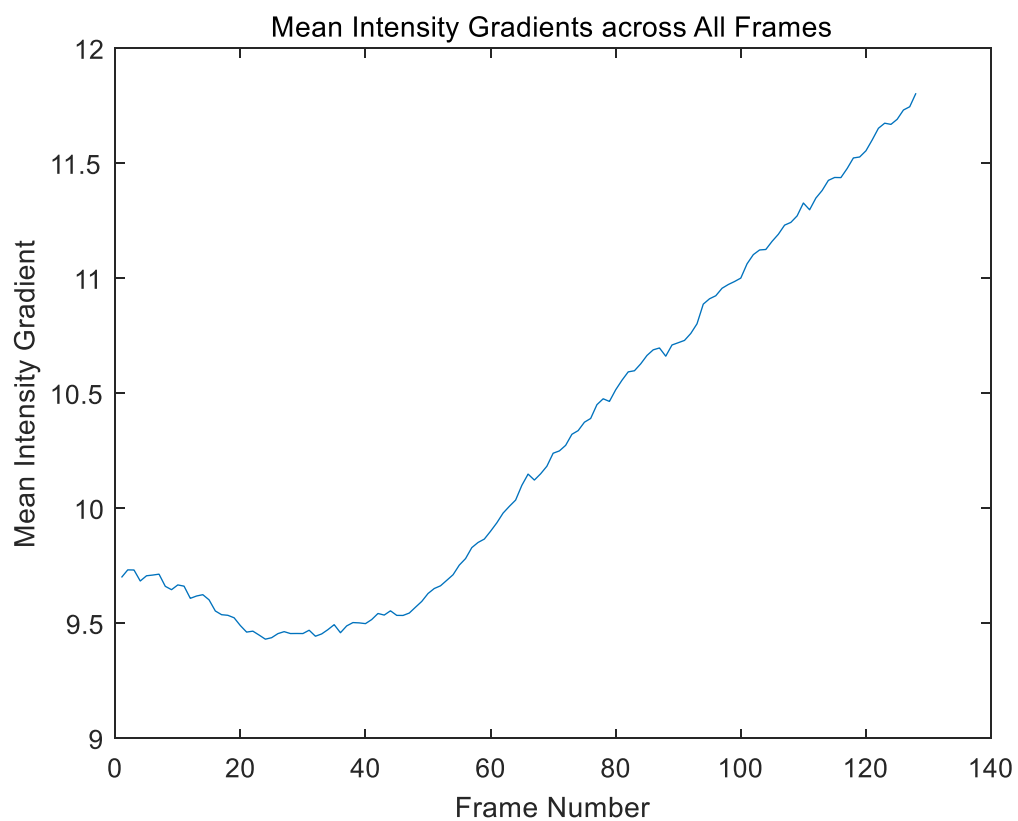


Figure 30. Mean Intensity Gradient Change during the Impact Process, 10% FeO.

Similarly, the number of features present in the images increased as the inclusion content increased. The intensity distribution did not change significantly compared to the 7% FeO sample. The mean intensity gradient exhibited exactly the same trend as the former samples, increasing by ~2 during the compression process.

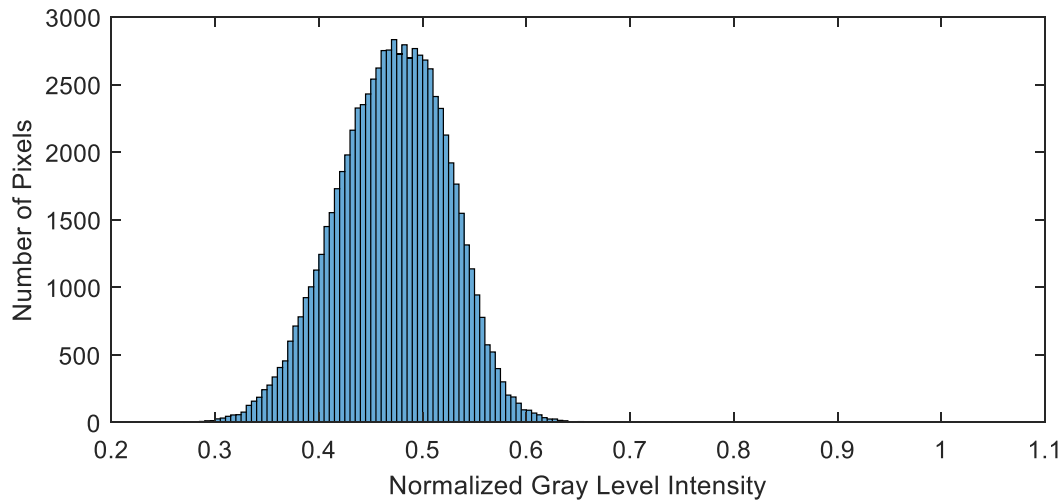


Figure 31. Gray Level Intensity Distribution in the 10% FeO Sample Image.

### 3.2.4 FeO Inclusions at 13% Weight

Representative images of Sylgard® with 13% of FeO particles during the process of being compressed are presented in Fig. 32. The region enclosed by the red box is the region of interest in each frame. Figure 33 shows the mean intensity gradient change during the impact process.

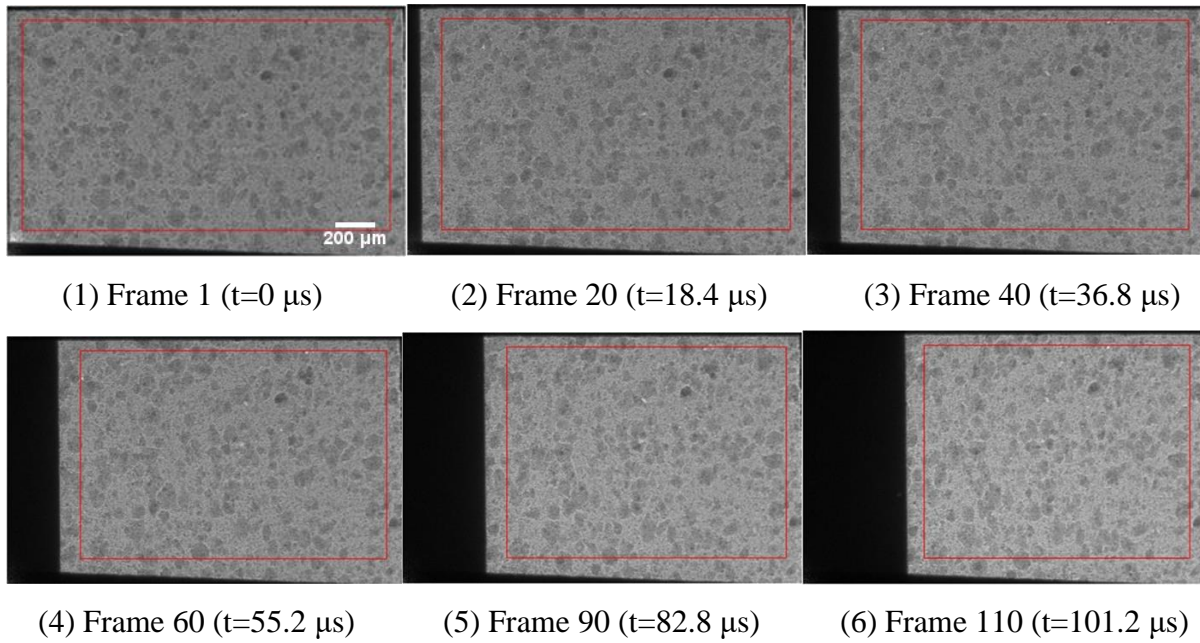


Figure 32. Sylgard® with 13% FeO particles under impact.

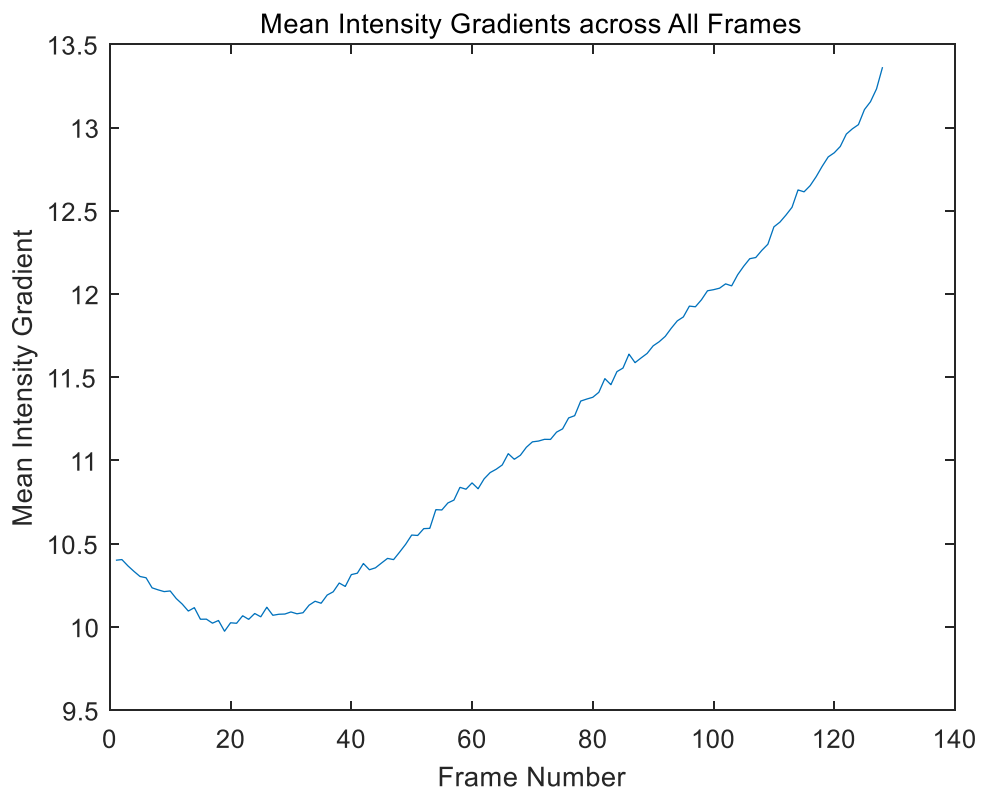


Figure 33. Mean Intensity Gradient Change during the Impact Process, 13% FeO.

From observation, the number of features present in the images increased, but not as apparent as the former samples. It can be summarized that the intensity distribution does not change significantly based on the inclusion weight ratio for FeO particles. The mean intensity gradient exhibited exactly the same trend as the former samples, increasing by  $\sim 3$  during the compression process.

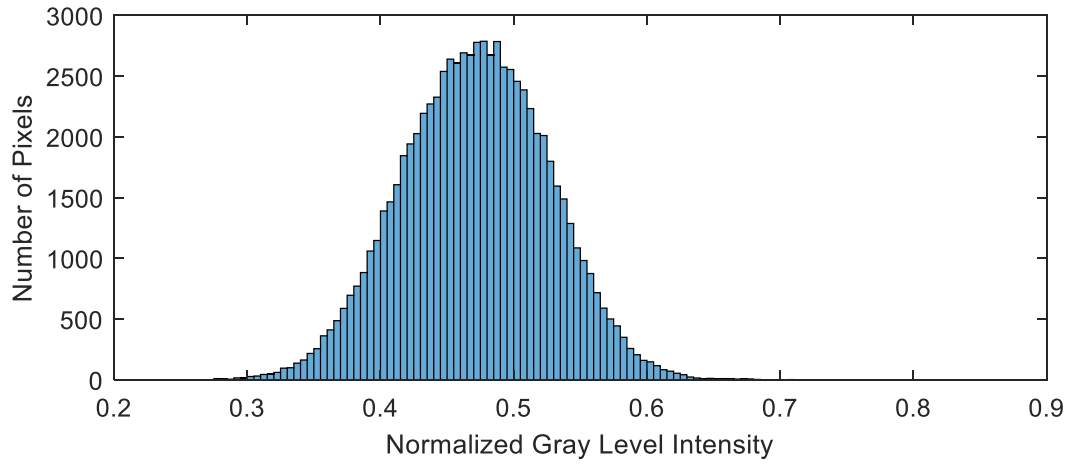


Figure 34. Gray Level Intensity Distribution in the 13% FeO Sample Image.

### 3.2.5 WC Inclusions at 4% Weight

Representative images of Sylgard® with 4% of WC particles during the process of being compressed are presented in Fig. 35. The region enclosed by the red box is the region of interest in each frame. Figure 36 shows the mean intensity gradient change during the impact process. It can be seen on the left that the front surface of this sample is not flat. This may affect the wave profile in the sample as it is impacted.

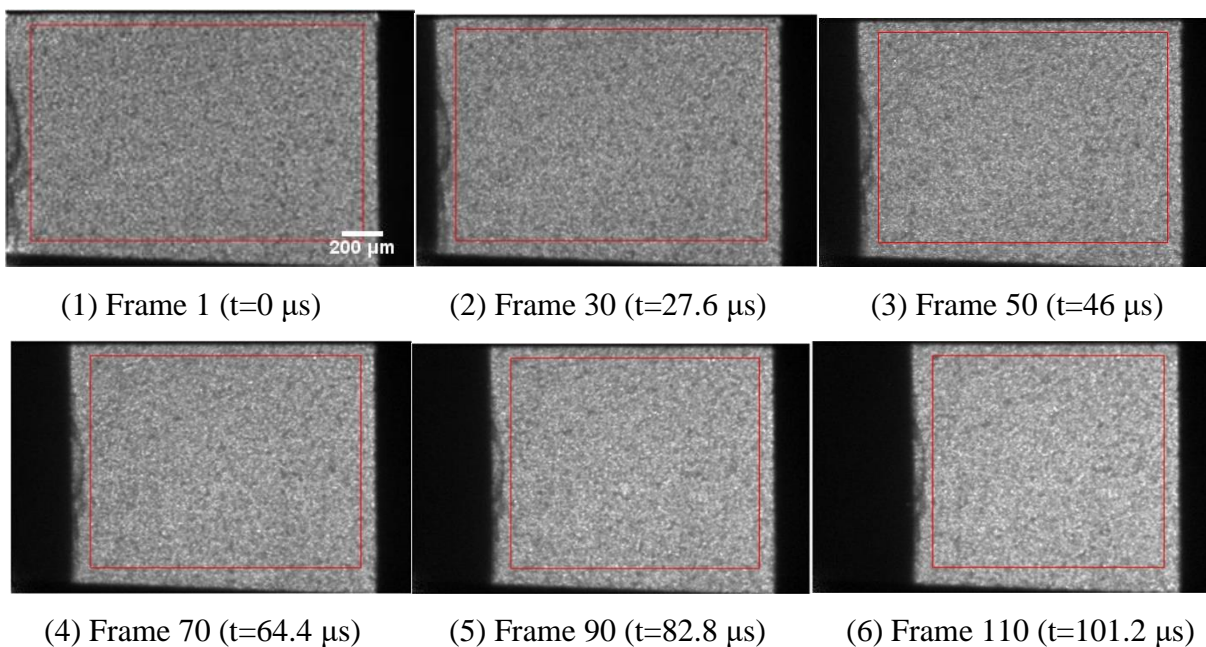


Figure 35. Sylgard® with 4% WC particles under impact.

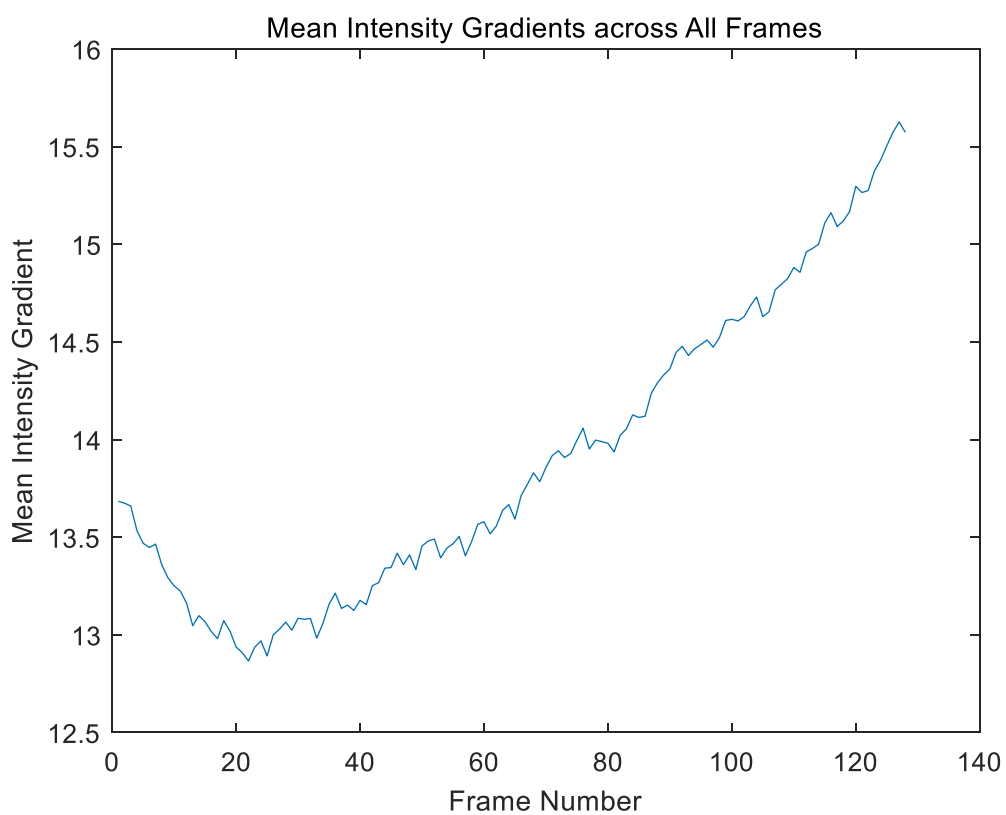


Figure 36. Mean Intensity Gradient Change during the Impact Process, 4% WC.

By observation, the sizes of the particle clusters are smaller and more evenly spread over the frame as compared to the FeO samples. The particles appear darker as well under X-ray PCI. These are indicators of better speckle pattern in general. In fact, this is evidenced in both mean intensity gradient and intensity distribution plots. Even as compared to the 13% FeO sample, the mean intensity gradient still significantly increased, by more than 30%, while keeping consistent with the trend. It may not be obvious from the shapes, but the distribution is more spread out over the spectrum, from 0.35-0.7.

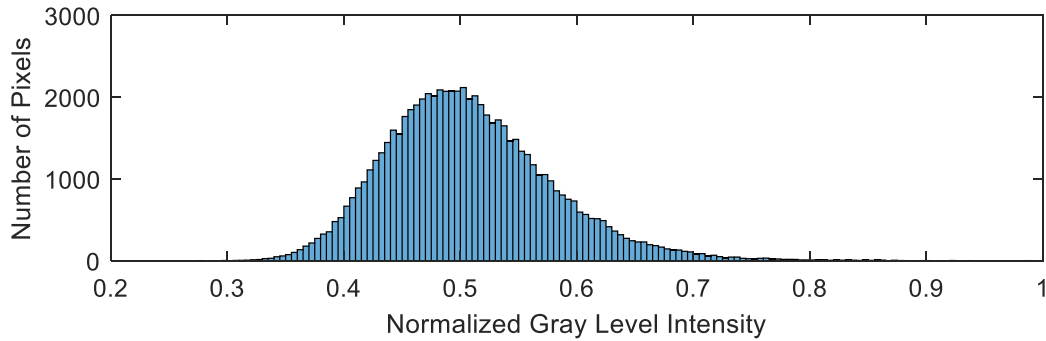


Figure 37. Gray Level Intensity Distribution in the 4% WC Sample Image.

### 3.2.6 WC Inclusions at 7% Weight

Representative images of Sylgard® with 7% of WC particles during the process of being compressed are presented in Fig. 38. The region enclosed by the red box is the region of interest in each frame. Figure 39 shows the mean intensity gradient change during the impact process. Regions of imperfect surface can be seen on the front edge.



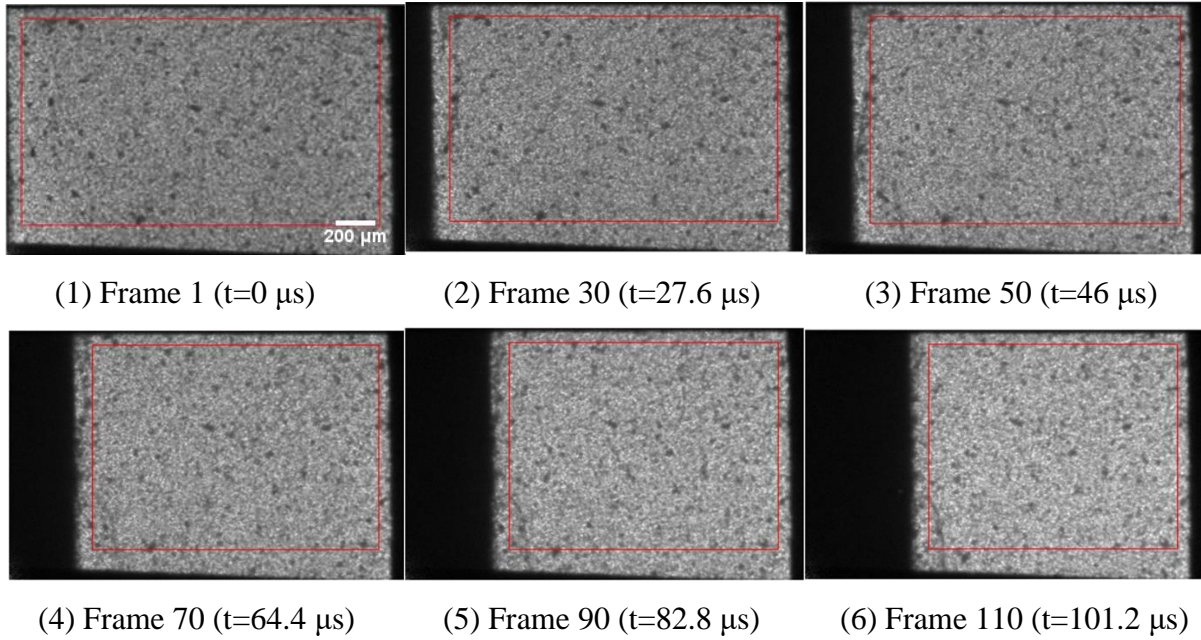


Figure 38. Sylgard® with 7% WC particles under impact.

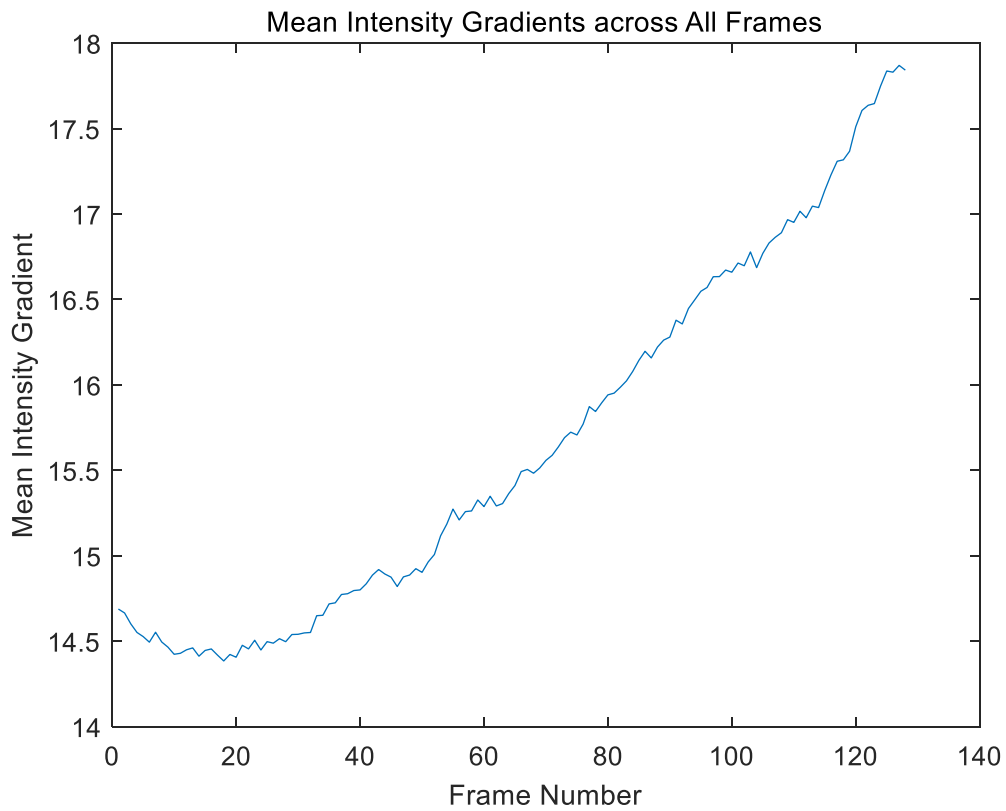


Figure 39. Mean Intensity Gradient Change during the Impact Process, 7% WC.

By observation, the particles appear denser and larger clusters start to form compared to the 4% WC sample. The mean intensity gradient increased as a whole and ramped up by  $\sim 3$  during the compression. The increase in particle content does not seem to significantly alter the intensity distribution except for leaning slightly towards the darker (towards 0) side. In this specific experiment, the compression seemed to start shortly before the camera started recording, by approximately 20 frames ( $18.4 \mu\text{s}$ ), inferring from the previous trend.

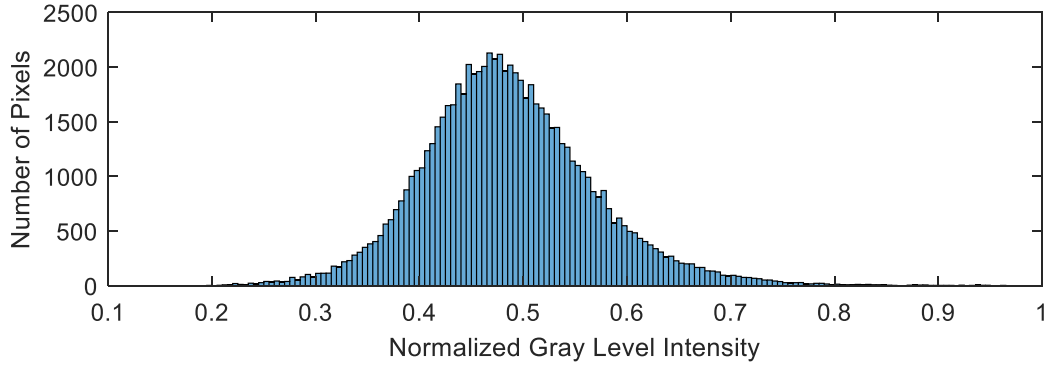


Figure 40. Gray Level Intensity Distribution in the 7% WC Sample Image.

### 3.2.7 WC Inclusions at 10% Weight

Representative images of Sylgard® with 10% of WC particles during the process of being compressed are presented in Fig. 41. The region enclosed by the red box is the region of interest in each frame. Figure 42 shows the mean intensity gradient change during the impact process.



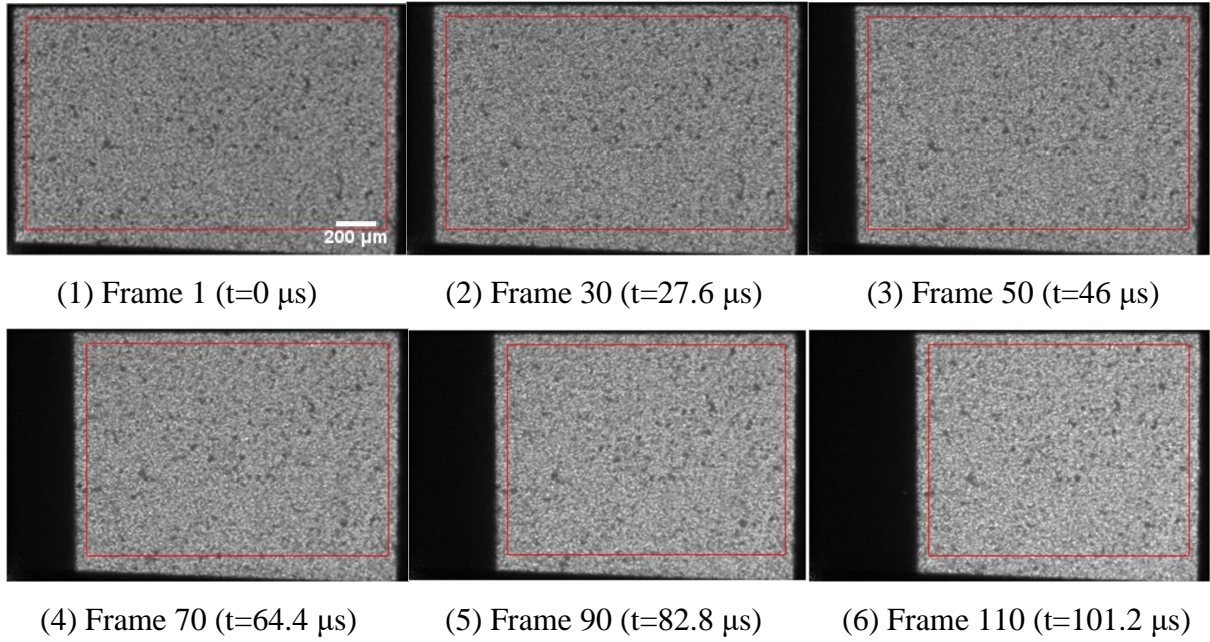


Figure 41. Sylgard® with 10% WC particles under impact.

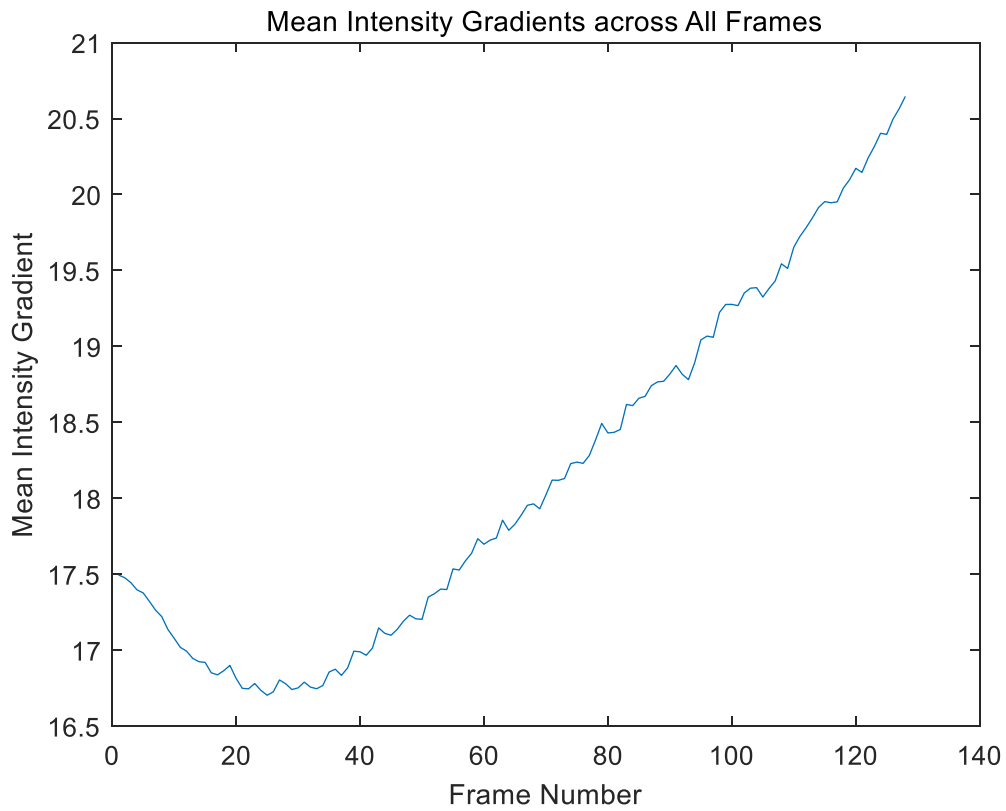


Figure 42. Mean Intensity Gradient Change during the Impact Process, 10% WC.

By observation, the particles appear denser as the particle content increases, and larger clusters does not seem to increase. The mean intensity gradient increased as a whole and ramped up by ~3 during the compression. A small jump in the overall mean intensity gradient values from that of the 7% WC sample can be found as compared to other samples. This can be explained by the recording delay in experiment with the 7% WC sample. The increase in particle content does not seem to significantly alter the intensity distribution except for leaning slightly towards the darker (towards 0) side.

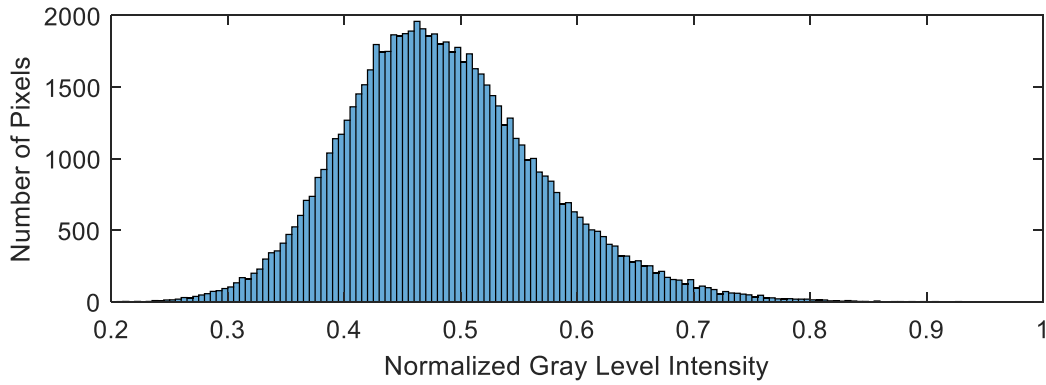


Figure 43. Gray Level Intensity Distribution in the 10% WC Sample Image.

### 3.2.8 WC Inclusions at 13% Weight

Representative images of Sylgard® with 10% of WC particles during the process of being compressed are presented in Fig. 44. The region enclosed by the red box is the region of interest in each frame. Figure 45 shows the mean intensity gradient change during the impact process.

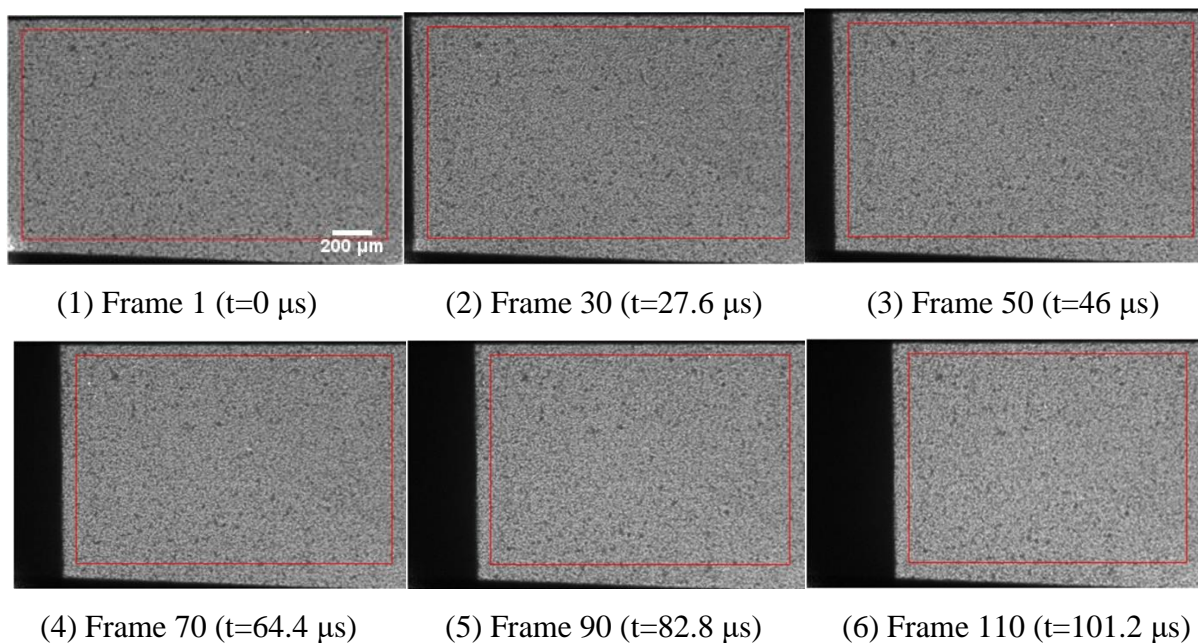


Figure 44. Sylgard® with 13% WC particles under impact.

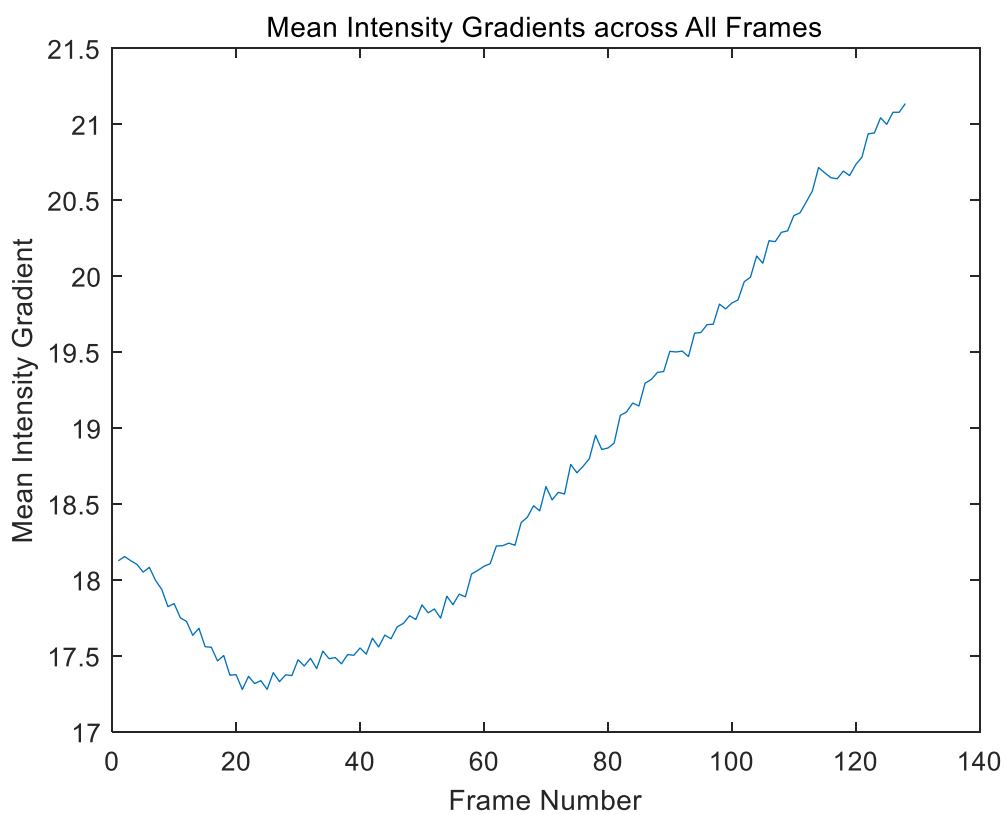


Figure 45. Mean Intensity Gradient Change during the Impact Process, 13% WC.

By observation, the particles appear denser as the particle content increases, and larger clusters does not seem to increase. The mean intensity gradient increased as a whole and ramped up by  $\sim 3$  during the compression. The increase in particle content does not seem to significantly alter the intensity distribution except for leaning slightly towards the darker (towards 0) side.

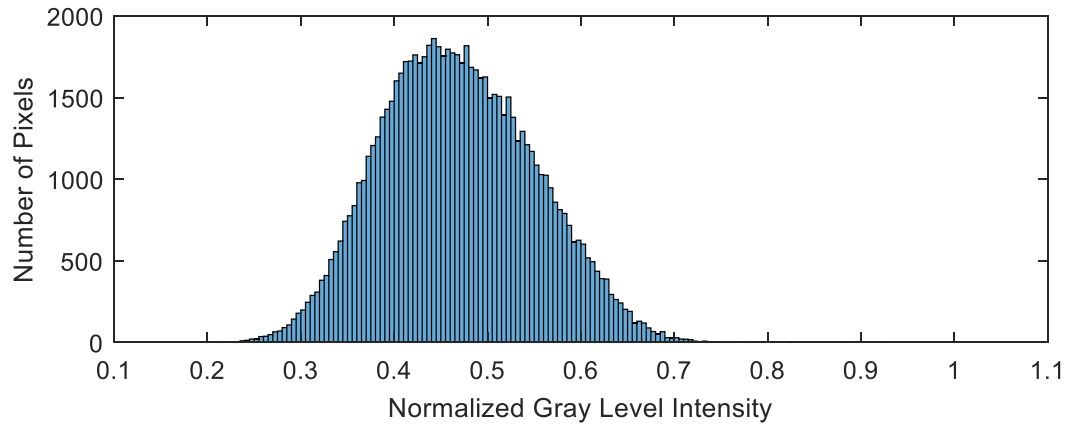


Figure 46. Gray Level Intensity Distribution in the 13% WC Sample Image.

### 3.2.9 Pt Inclusions at 5% Weight

Representative images of Sylgard® with 5% of Pt particles during the process of being compressed are presented in Fig. 47. The region enclosed by the red box is the region of interest in each frame. Figure 48 shows the mean intensity gradient change during the impact process.

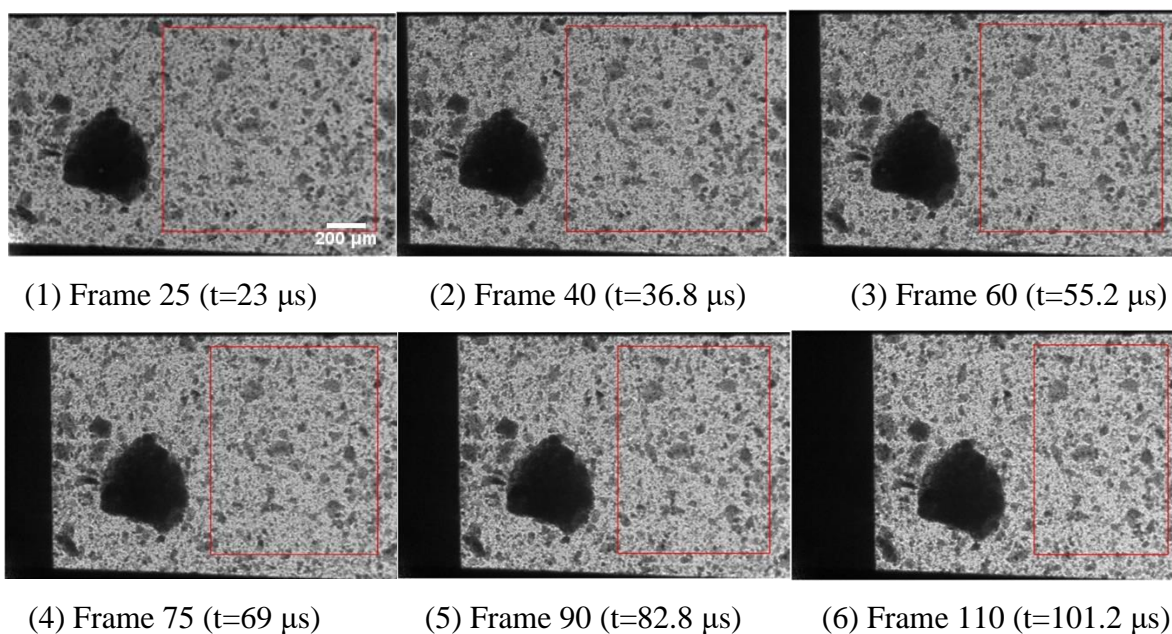


Figure 47. Sylgard® with 5% Pt particles under impact.

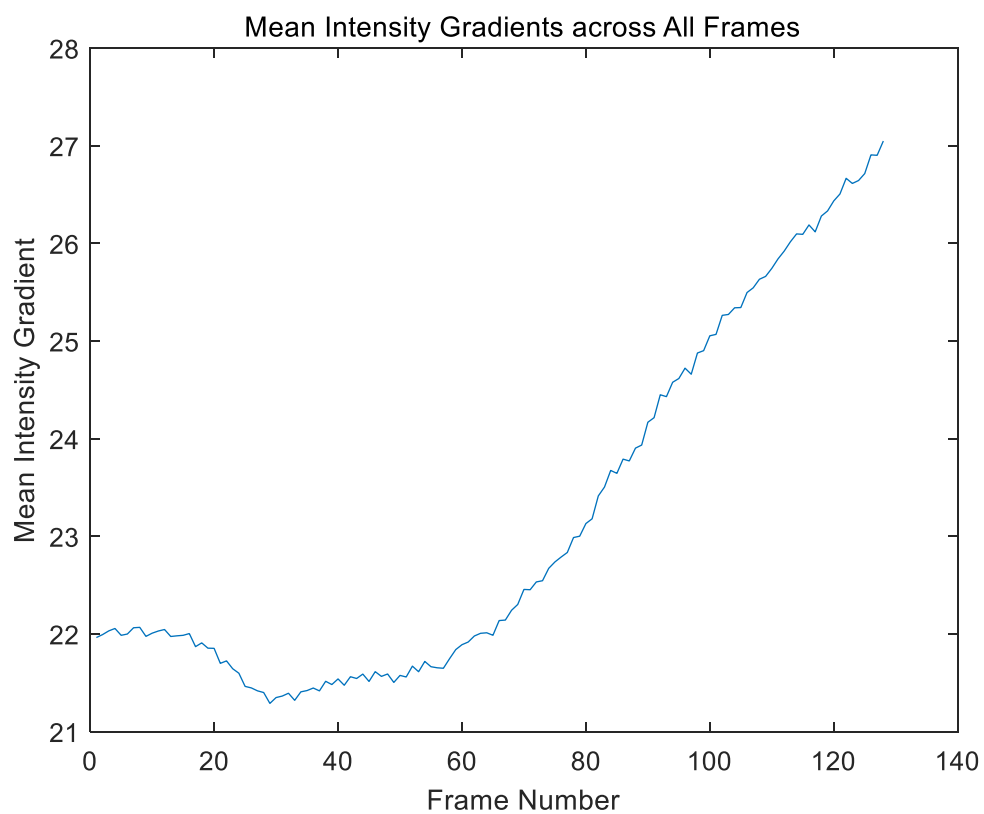


Figure 48. Mean Intensity Gradient Change during the Impact Process, 5% Pt.

Due to the presence of the large particle near the front surface, that region is excluded from the region of interest. The large particle is most likely an agglomerate of Platinum particles that formed from the reaction with the hardener. Although being cautiously avoided, reaction still happened in the sample. The region with such a particle is impossible to track with DIC because there is no speckle inside the particle, unless the chosen subset is even larger than the particle. The mean intensity gradient showed the same trend. The overall MIG values are significantly higher than WC particles even at 13%. Although distributed over the similar range, the intensity distribution lies more evenly than the WC samples, once again proving its superiority in producing speckles.

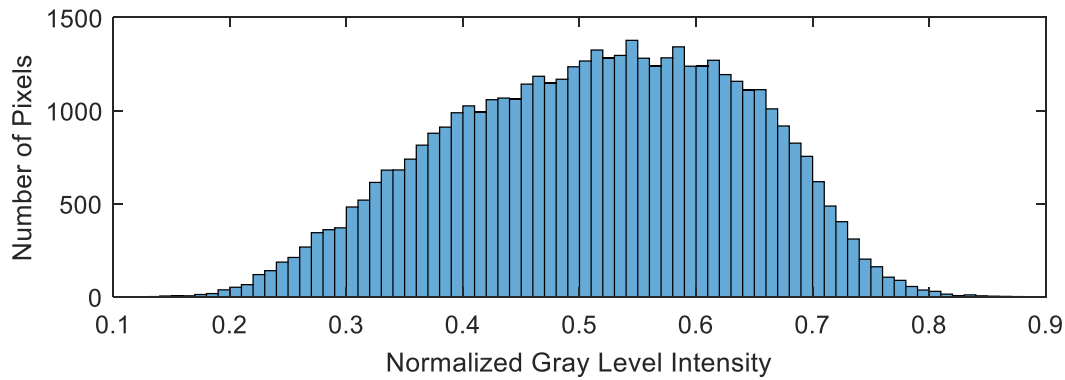


Figure 49. Gray Level Intensity Distribution in the 5% Pt Sample Image.

### 3.2.10 Speckle Assessment and Error Analysis

It is apparent that, no matter which inclusion material the sample has, increasing the weight ratio of the inclusions yields more distinct particle features present in the images. This may sound redundant but increasing the inclusion ratio by too much may lose distinct features due to the stacking of all layers of the sample in the X-ray propagation direction. This is also evidenced in the mean intensity gradient change across all samples as denser particle population means higher gradient density. However, the increase in mean gradient intensity from adding more particles seems less effective than changing the material of the inclusion. Defining the nominal mean intensity gradient as the mean intensity gradient value at the first frame, Table. 3 presents the nominal mean intensity gradient of all samples studied.

Table 3. Mean Intensity Gradient of Each Sample.

FeO Inclusions		WC Inclusions		Pt Inclusions	
Weight Ratio	MIG	Weight Ratio	MIG	Weight Ratio	MIG
4%	7.6	4%	13.7	5%	22.0
7%	8.7	7%	14.7		
10%	9.7	10%	17.5		
13%	10.4	13%	18.2		

First of all, it is obvious that Platinum particles out-compete any other particle types in every category, as expected being the presumed optimum case in this study. Usage of Pt particles should be considered if the speckle quality requirement outweigh the cost while making sure it does not react with the matrix during manufacture.

It can be seen from the samples with FeO inclusions that, by increasing the same amount of inclusion, the increase in the overall speckle quality decreases. The only exception is that between the 7% WC sample and the 10% WC sample, there is a small jump in the mean intensity gradient value. This trend can be a good sign because monotonically increasing the inclusion content is increasingly ineffective in improving the speckle quality. Therefore, an optimized value should be sought at lower values of inclusion weight ratio. On the other hand, increasing the FeO inclusion weight ratio by 9% only yields 2.8 in mean intensity gradient, which is 36.8%, while switching to WC at 4% immediately results in an 80.3% increase.

Compared to the calibration experiments reported in literature, the speckle quality can be considered acceptable if the mean intensity gradient is greater than 10 [24]. Although, the physical significance of the mean intensity gradient values is still ambiguous if it is not related to the theoretical error of the DIC measurement. For subsets with size  $N \times N$ , the average theoretical error can be calculated from

$$std(u_e) \cong \frac{\sqrt{2}\sigma}{N\delta_f}.$$



Table 4. Theoretical Deviation Error of Each Sample.

FeO Inclusions		WC Inclusions		Pt Inclusions	
Weight Ratio	Error (px)	Weight Ratio	Error (px)	Weight Ratio	Error (px)
4%	0.0074	4%	0.0041	5%	0.0026
7%	0.0065	7%	0.0038		
10%	0.0058	10%	0.0032		
13%	0.0054	13%	0.0031		

The theoretical error based on the nominal mean intensity gradient and subset size of 25 X 25 pixels is presented in Table. 4. One pixel corresponds to 6.4  $\mu\text{m}$  in the sample. The results once again remind that monotonically increasing the inclusion content does not effectively eliminate measurement error. However, by switching from FeO at 4% weight to WC at 4% weight, the error decreased by 44.6%. Theoretically, if the target accuracy is 0.01 pixels (0.064  $\mu\text{m}$ ), and the resolution is 25 pixels (160  $\mu\text{m}$ ), all choices of configuration satisfy the requirements. However, depending on the specific interest, finer resolution may be desired. Table. 5 shows the best theoretical resolution each configuration can achieve if 0.01 pixels (0.064  $\mu\text{m}$ ) accuracy is accepted. Comparing the achievable subset size of 4% FeO sample to that of 4% WC sample, the size almost halved, gaining almost double resolution. This can be considered a great improvement given that the size of entire frame is only 400 X 250 pixels.

Table 5. Subset Size Required to Ensure 0.01 pixels Theoretical Error.

FeO Inclusions		WC Inclusions		Pt Inclusions	
Weight Ratio	Subset Size	Weight Ratio	Subset Size	Weight Ratio	Subset Size
4%	19	4%	11	5%	7
7%	17	7%	10		
10%	15	10%	9		
13%	14	13%	8		

As for the gray level intensity distribution, it is desired that the intensity is spread out across the spectrum, because more intensity values means more distinct features. From the previously presented histograms, increasing the inclusion content does not significantly alter the intensity distribution. However, the distribution is significantly affected by the inclusion material. This can be explained with the diffraction difference between different materials as X-ray propagates through. Figure 50 shows the distribution comparison between the 4% FeO sample and the 4%



WC sample. The gray level intensity of the 4% WC sample is much more evenly spread over the spectrum.

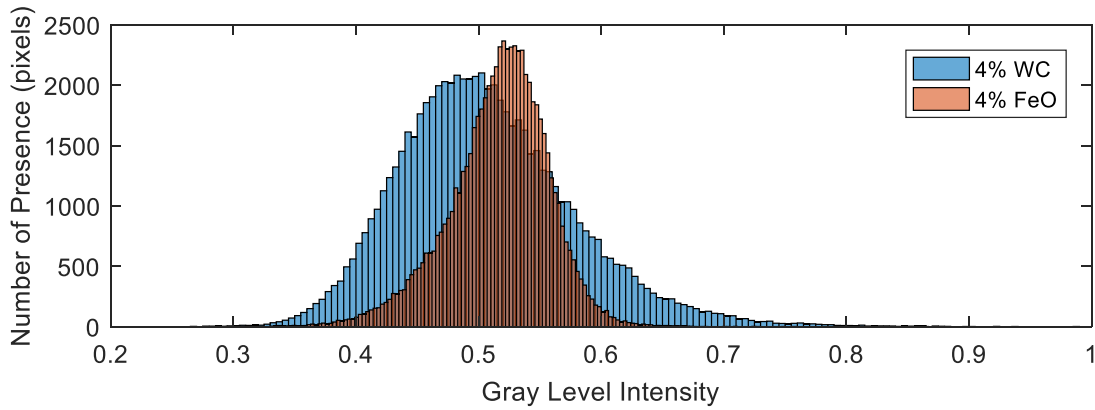


Figure 50. Intensity Distribution Comparison between the 4% FeO Sample and the 4% WC Sample.

With all these facts combined, it is apparent that material-wise, the tungsten carbide power is the superior choice for desirable DIC speckle quality. Since increasing weight ratio of inclusions does not improve the speckle quality at good efficiency, lower levels of particle content should be preferred unless certain parameter, such as measurement resolution, is required by the research interest. It is also optimal if the measurements start 60 frames ( $\sim 55 \mu\text{s}$ ) after the sample starts being compressed, as the speckle quality starts to ramp up.

### 3.3 X-ray DIC Results

Selected X-ray DIC results are displayed in this section for each sample. The time instants chosen are based on the sample deformation. Frames without any deformation are not chosen to be presented. The region of interest is selected and evolves in the same way as the previous section. The subset size of 25 X 25 pixels is uniformly used throughout all the samples. Each displacement map is fitted into the box that encloses the region of interest. Since the loading can be considered one dimensional, only the displacement in the load direction,  $u$ , is shown. For each measurement, the displacement is not calculated from the time instant to the next frame, but rather to 3 frames later such that the time elapsed is  $\sim 2.76 \mu\text{s}$ . The color bars are given in units of pixels. DIC results

with finer resolution is also presented for the superior choice of inclusion configuration—WC at 4%. Discussion of the results is provided after all the results are shown.

### 3.3.1 FeO Inclusions at 4% Weight

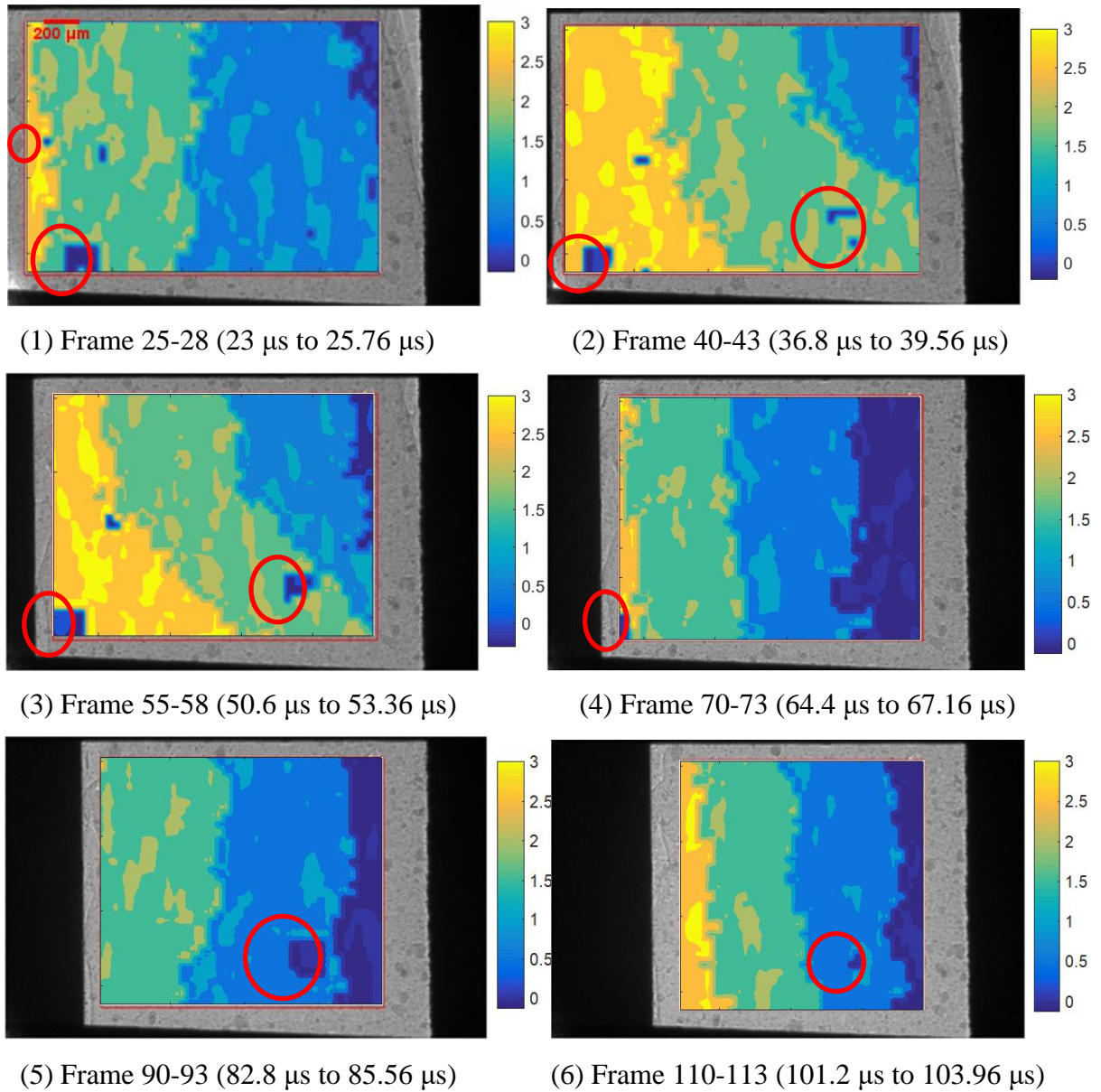


Figure 51. Displacement map of the 4% FeO sample.

The displacement maps of Sylgard® sample with 4% FeO at selected instants are presented in Fig. 51. As presented in all the frames, the front layer of the sample experienced the most displacement, at  $\sim 3$  pixels ( $19.2\ \mu\text{m}$ ). This result matches the approximately 1 pixel/frame displacement at the front of the sample from XPCI images. The back of the sample almost did not deform at all. There are distinct layers of displacement propagating through the sample as it is compressed. Such layer is not uniform in the vertical plane in the first half of deformation but settles down later. All these features agree with observations on the PCI images. However, there are regions that exhibit apparent measurement errors (marked with red ellipses). The larger error sites stick with their locations in the sample through the process and even tend to vanish as the sample is compressed the most. This can be due to the local low speckle quality or distortion of particles in the X-ray direction.

### 3.3.2 FeO Inclusions at 7% Weight

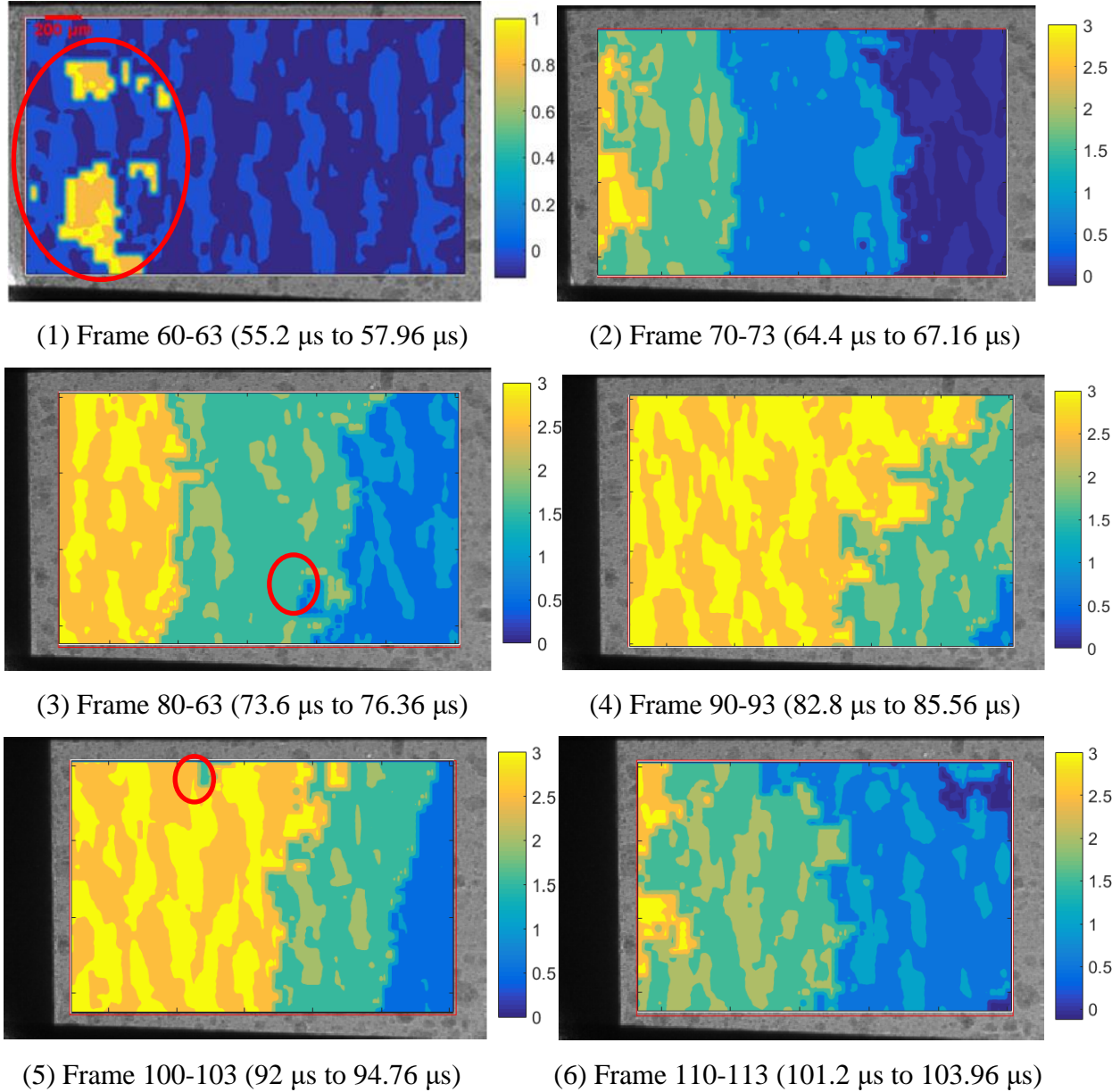


Figure 52. Displacement map of the 7% FeO sample.

The displacement maps of Sylgard® sample with 7% FeO at selected instants are presented in Fig. 52. The first selected moment was as the sample just started to show deformation. In the rest of the frames, the displacement showed the same trend as the 4% FeO sample. Since the time frame presented is significantly shorter for this experiment, the frame to frame comparison may seem different. As the sample is compressed, the displacement through the sample ramps up from

frame (2) to frame (4) before dying down. The region marked with red ellipse in frame 1 cannot be considered reliable because the region in front of this deformed region shows no displacement, which is against physics. Besides this, only minor error sites are found occasionally (marked with red ellipse in frame (3) and (5)).

### 3.3.3 FeO Inclusions at 10% Weight

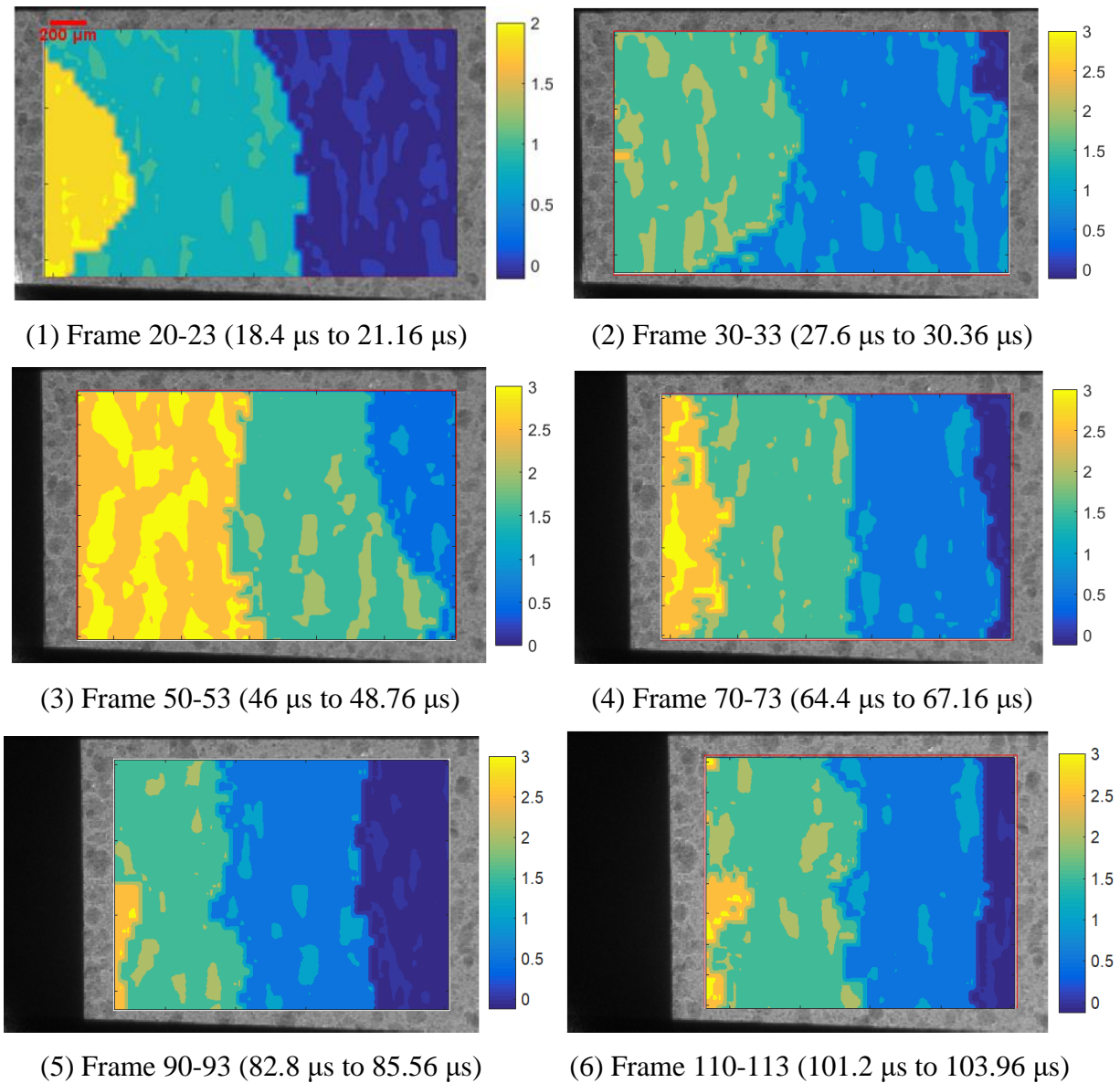


Figure 53. Displacement map of the 10% FeO sample.



The displacement maps of Sylgard® sample with 7% FeO at selected instants are presented in Fig. 53. The displacement evolvement exhibited the same trend. It should be noted that the color bar scale in the first frame is different from the rest. As the sample is compressed, the sample shows a pulse of acceleration before slowing down, and the displacement took some time to become uniform in the vertical planes from frame (1) to (4). There is not apparent error site exhibiting in this experiment.

### 3.3.4 FeO Inclusions at 13% Weight

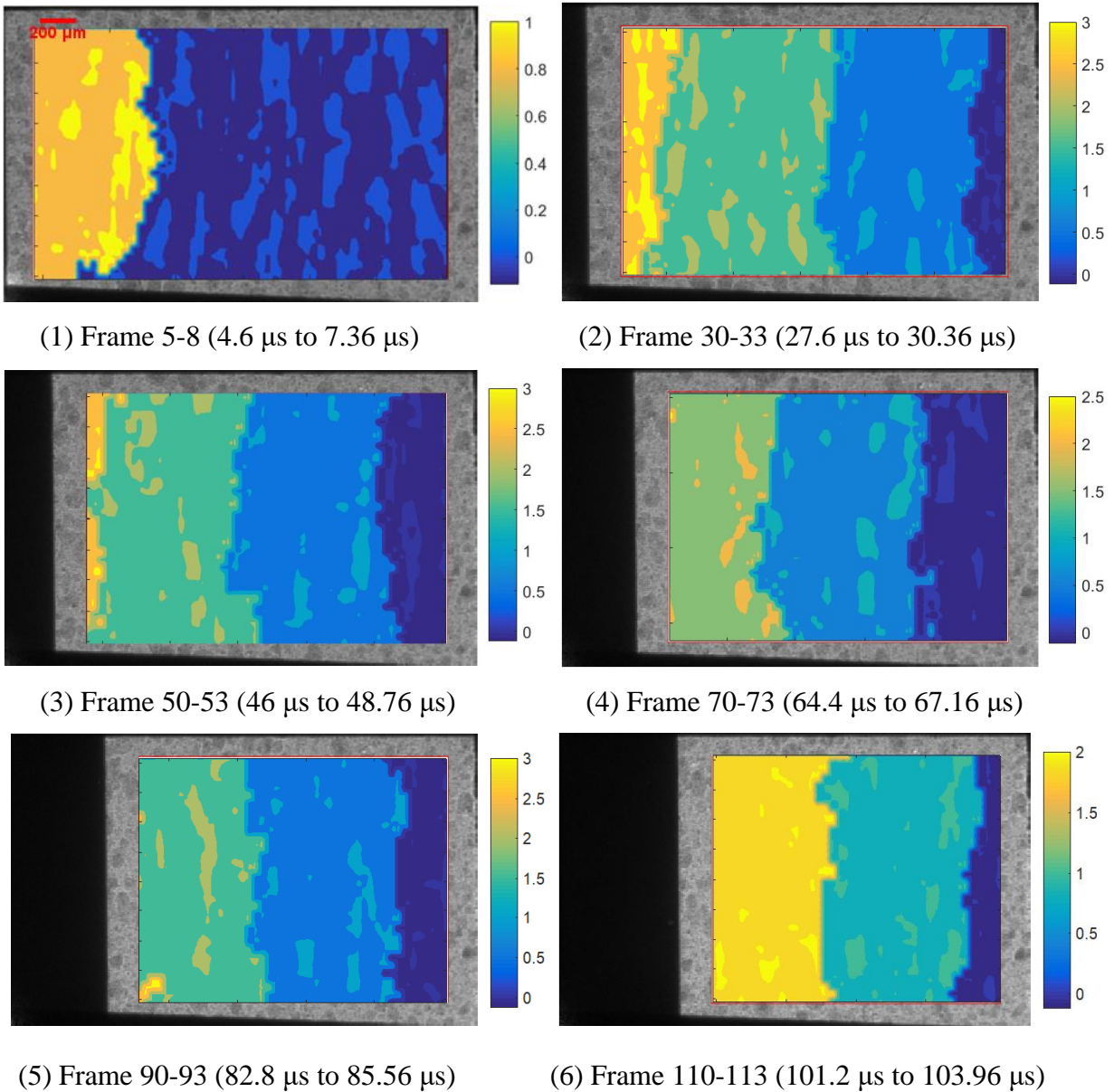


Figure 54. Displacement map of the 13% FeO sample.

The displacement maps of Sylgard® sample with 7% FeO at selected instants are presented in Fig. 54. The displacement evolvement appears to be the same as other FeO samples. The displacement became stable within a shorter period of time compared to the previous FeO samples. No major or minor error sites are spotted in these frames.

### 3.3.5 WC Inclusions at 4% Weight

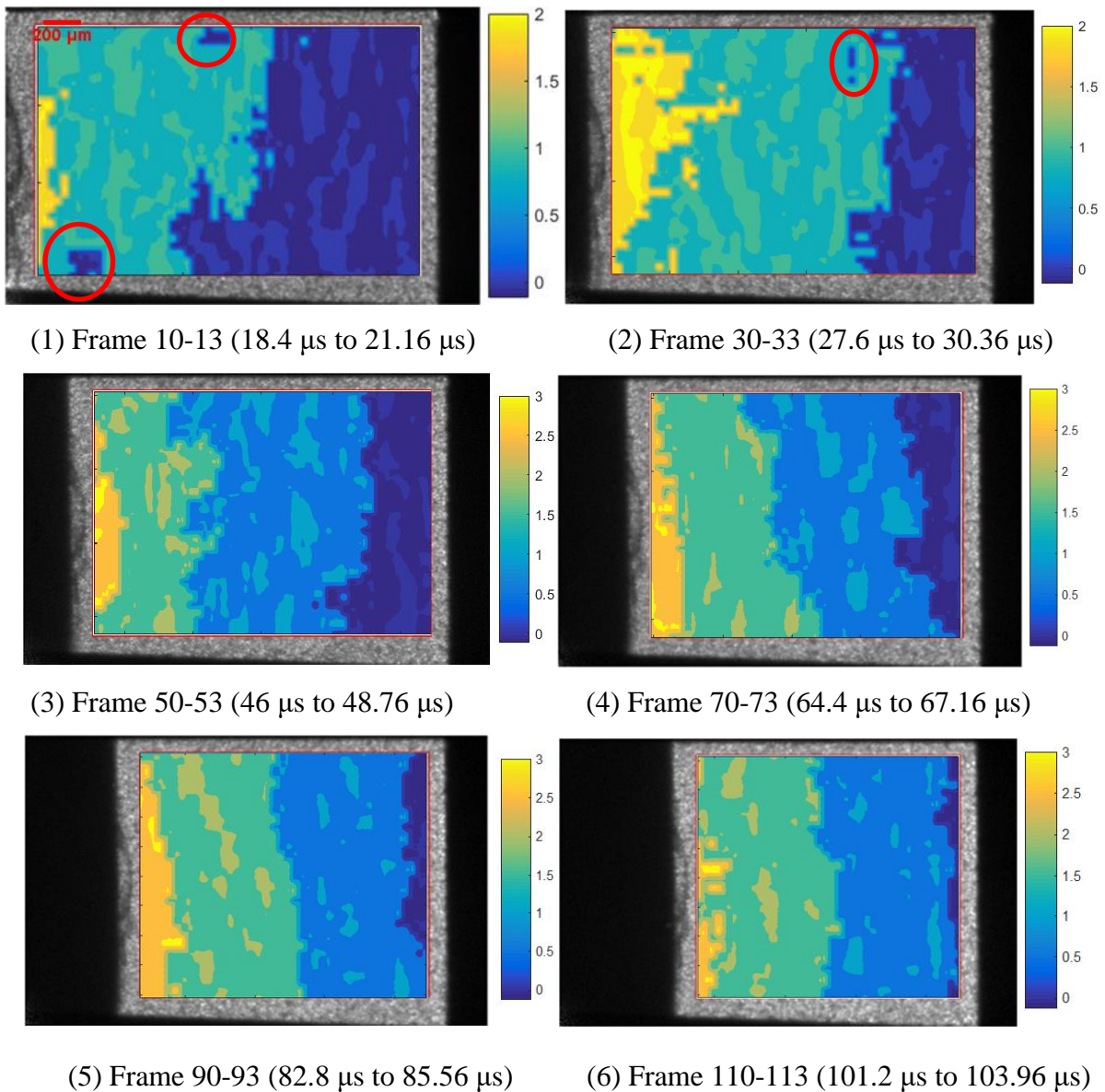


Figure 55. Displacement map of the 4% WC sample.

The displacement maps of Sylgard® sample with 4% WC at selected instants are presented in Fig. 55. Compared to the FeO samples, while the overall displacement evolvement is of the same trend, the displacement propagation is more distorted. It also took longer for the displacement to become uniform in the vertical planes. At the acceleration stage, some minor error sites are spotted and marked. As the sample is compressed, these sites vanish.

### 3.3.6 WC Inclusions at 7% Weight

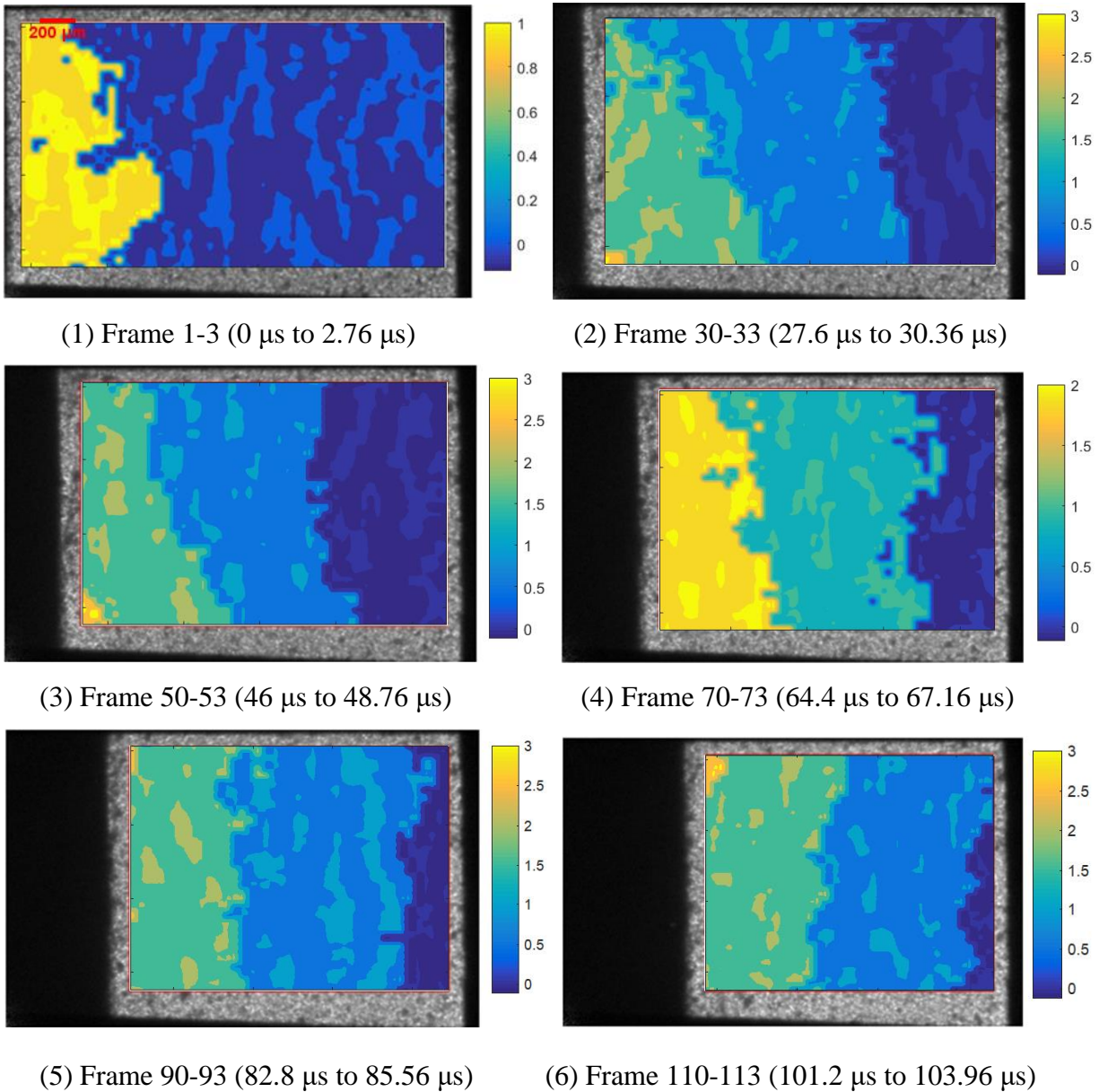


Figure 56. Displacement map of the 7% WC sample.



The displacement maps of Sylgard® sample with 7% WC at selected instants are presented in Fig. 56. The frames selected capture the deformation process from the start of acceleration. Similar to the 4% WC sample, the displacement propagation exhibits some distortion, which settles down as the compression goes on. The displacement starts to show signs of uniformity in the vertical planes from frame (4). No apparent error sites are found once the deformation becomes steady.

### 3.3.7 WC Inclusions at 10% Weight

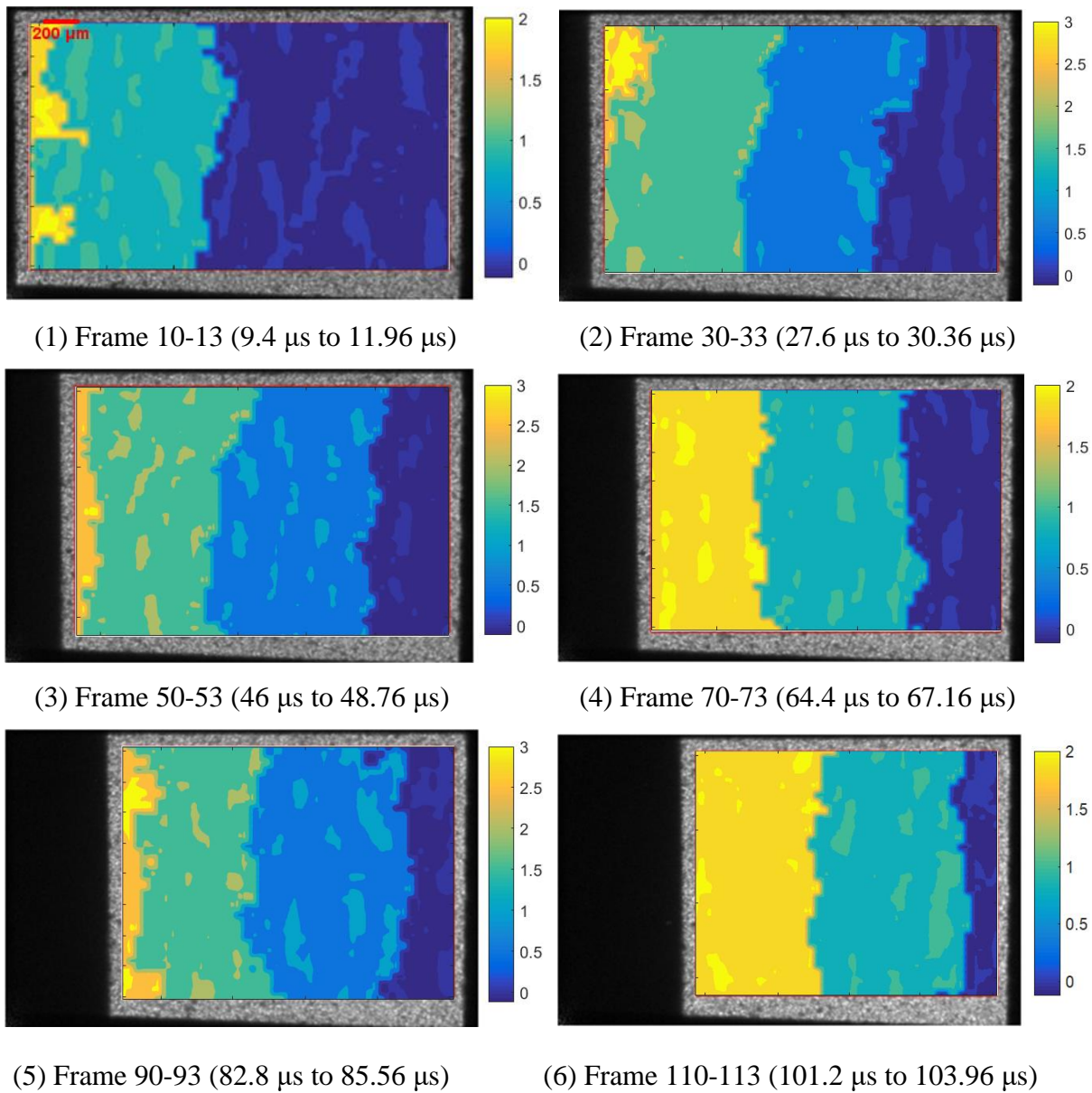


Figure 57. Displacement map of the 10% WC sample.

The displacement maps of Sylgard® sample with 10% WC at selected instants are presented in Fig. 57. The displacement evolution exhibits the same trend as the rest of the WC samples. The displacement becomes uniform faster than the previous samples. No major error sites are found.

### 3.3.8 WC Inclusions at 13% Weight

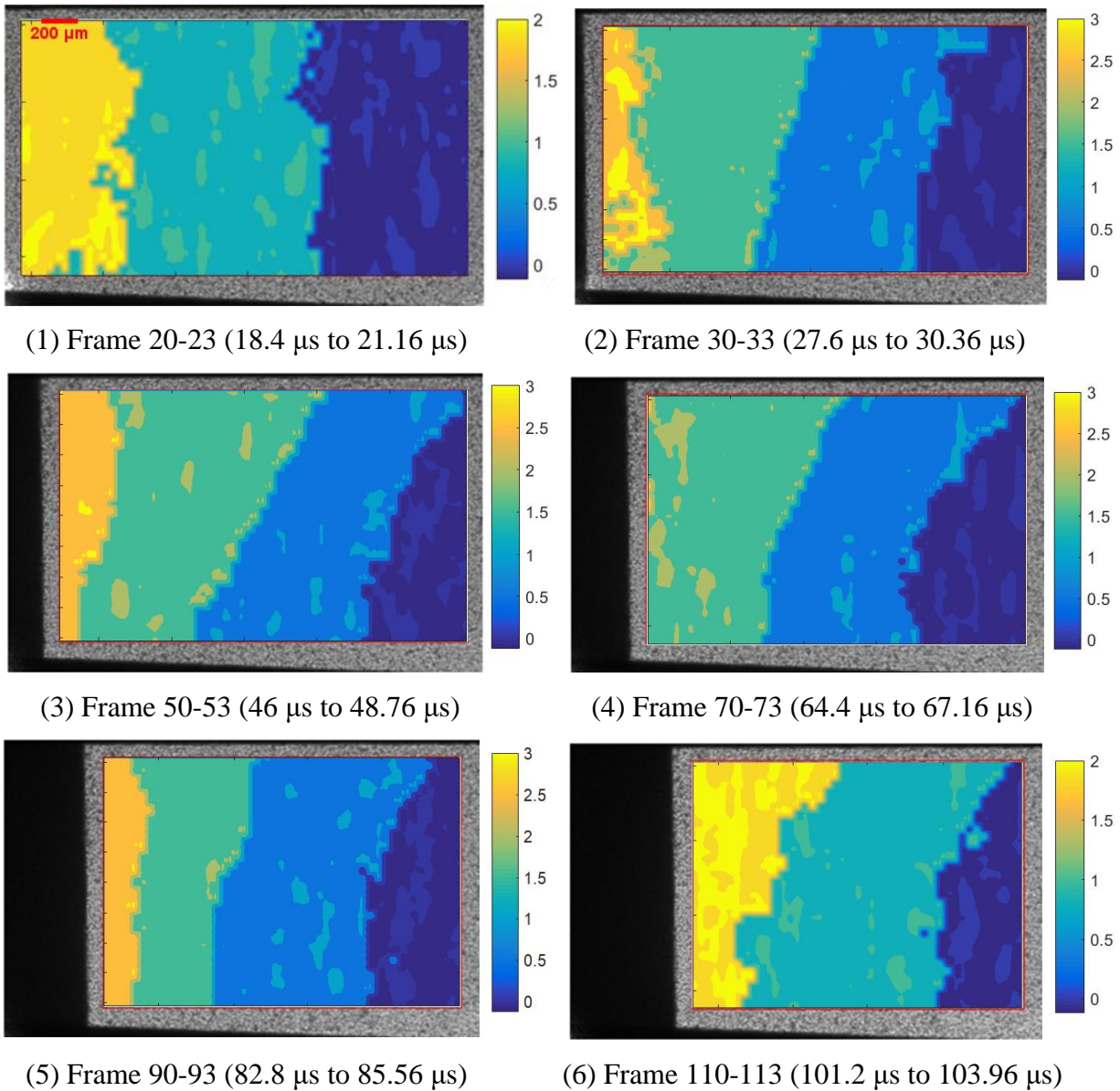


Figure 58. Displacement map of the 10% WC sample.

The displacement maps of Sylgard® sample with 10% WC at selected instants are presented in Fig. 58. The displacement map evolves in the same way as all other samples. However, in this experiment, the displacement never becomes uniform in the vertical direction even as the deformation starts to decelerate. The distortion at the propagation front in this experiment is less dominant. No major or minor error sites are found throughout the process.

### 3.3.9 Pt Inclusion with 5% Weight

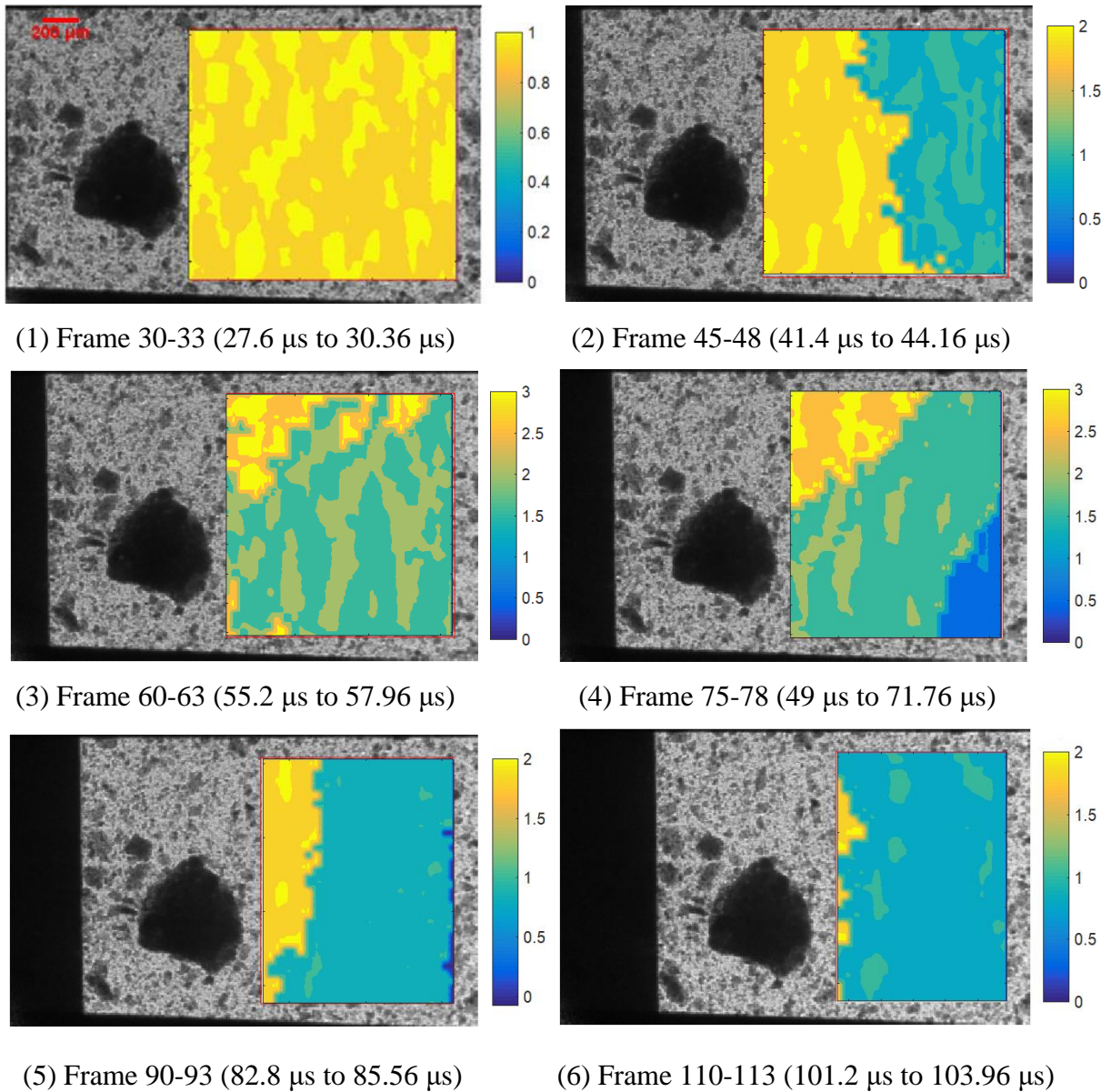


Figure 59. Displacement map of the 10% WC sample.



The displacement maps of Sylgard® sample with 10% WC at selected instants are presented in Fig. 59. Although only limited region is analyzed with DIC, the displacement map in this region exhibits the same trend as in other samples. The displacement settled to be uniform in the vertical planes in the last two frames. There are no apparent error sites visible in all frames, and the displacement map showed the least fluctuation among all samples.

### 3.3.10 WC Inclusion with 4% Weight at Finer Resolution

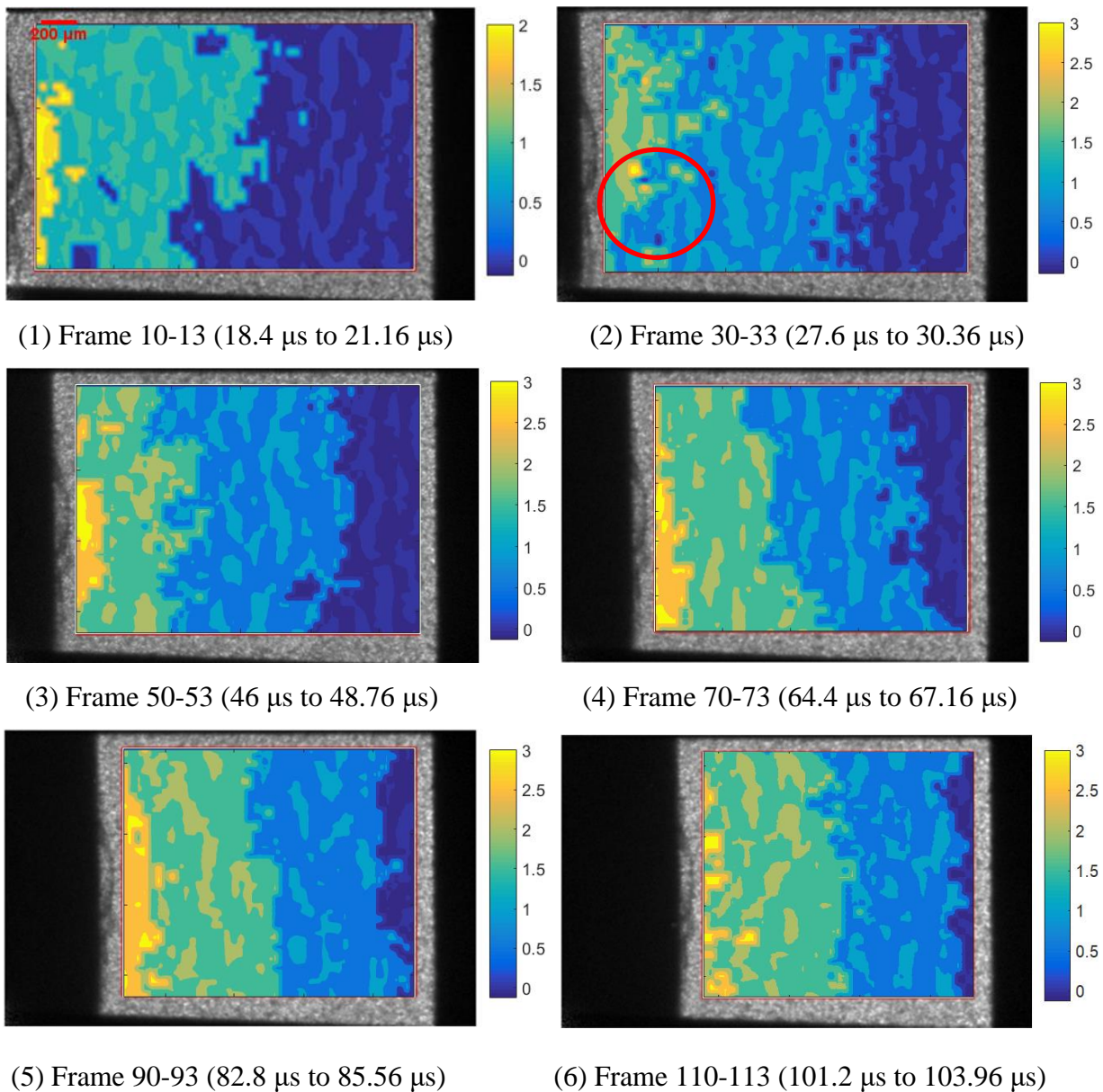


Figure 60. Displacement map of the 4% WC sample using 19 X 19 subsets.

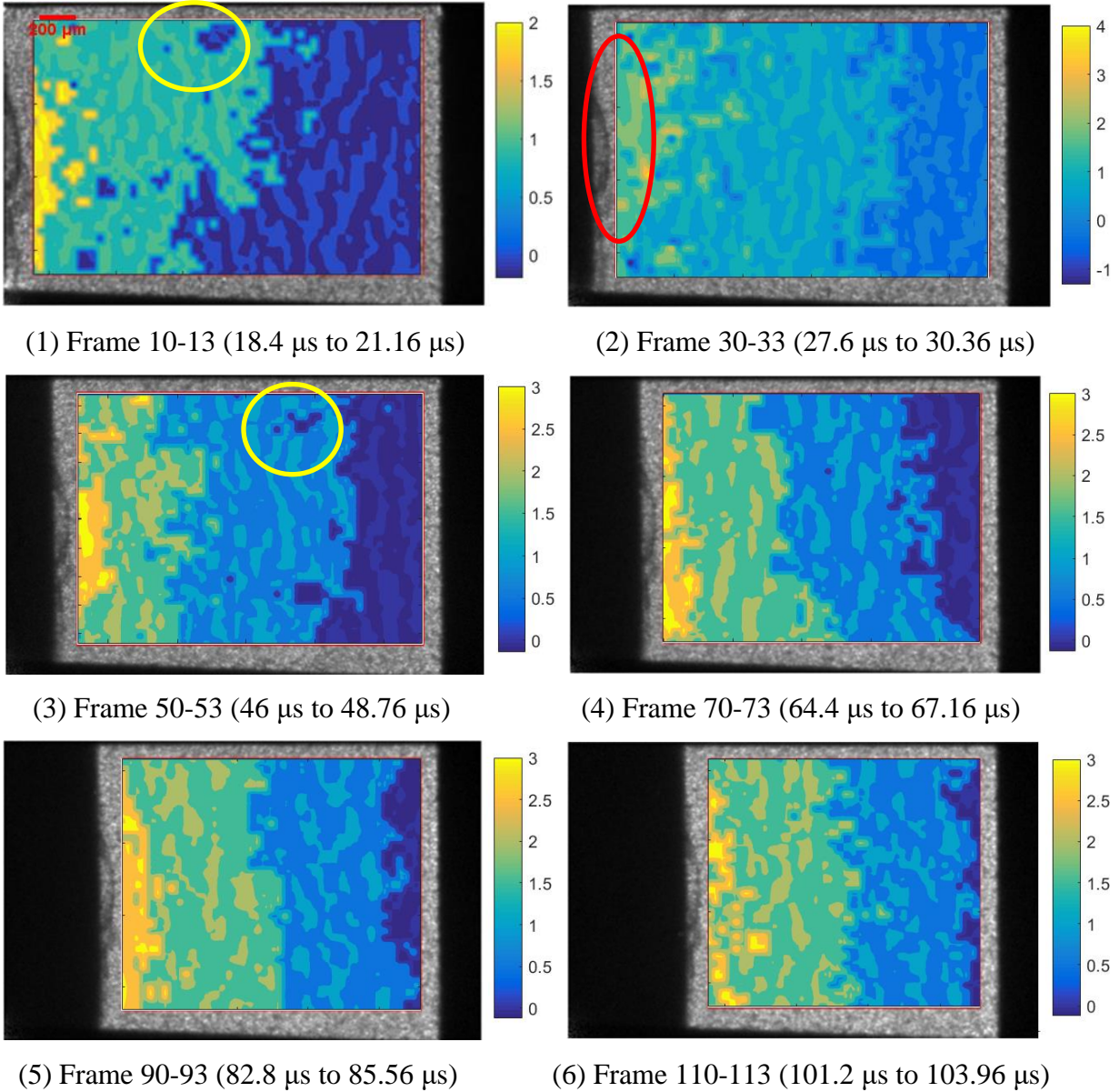


Figure 61. Displacement map of the 4% WC sample using 13 X 13 subsets.

The displacement maps of Sylgard® sample with 4% WC using subsets of 19 X 19 and 13 X 13 pixels are presented in Fig. 60 and Fig. 61, respectively. Although according to theoretical calculation, the size can be as small as 11 X 11 pixels, conservative concerns were considered, and 13 X 13 pixels subsets are used. Although staying in the same overall shapes and patterns, as the size of subsets decreases, more details of the displacement map are revealed. Based on the results, some of the presumed error sites may simply be highly distorted borders of the regions with different displacements. Some examples are marked with yellow ellipses in Fig. 61. Reducing

subset size also introduces minor error sites, as marked in Fig. 60 and Fig. 61 with red ellipses. Despite higher possibility of inducing error, subset size reduction is always recommended for qualitative examination.

### **3.3.11 Discussion on the DIC Result**

A few things can be summarized from the DIC results. In samples with lower particle weight ratio, minor error sites can be present especially in the early stages of the compression process. This is likely due to the local regions of low-quality speckles. In samples with higher particle weight ratio, where the particles are apparently denser, the amount of error sites reduces or vanishes. Although samples with smaller amount of WC yields higher mean intensity gradient than samples with higher amount of FeO, more error sites are found in the WC samples. This means that the particle density is also an important factor when it comes to the reliability of measurement. Other than this dispute, the DIC analysis quality is as expected. For any particle weight ratio, the WC results are always better than the FeO results, just as the MIG predicted. Less error sites are found with the WC samples than FeO samples. Also, for each material, the samples with higher content ratios are always better than that of lower content ratios, as expected.

During the compression process of any sample, it is apparent that the quality of DIC measurement keeps improving. Error sites reduce or vanish, and displacement measurements becomes more stable. This is also as expected since the MIG has shown to increase during the compression process of a sample. It is also important to note that most of the error sites form near the outer portion of the Sylgard® sample. Some unstable or distorted displacement measurements, where large errors may reside, also occurs near the edges, for example, frame (2) in the 13% WC sample, or frame (2) in the 4% WC sample. This is due to that the sample is more likely to distort in the X-ray direction near the surfaces, causing the particle pattern to morph as if there is a discontinuity. When tracking the subsets that include these regions in the deformed frame, it is impossible to find the true optimum. These facts suggests that when designing a polymer matrix sample in Kolsky bar experiments paired with XDIC, it is important to make sure the region of interest is away from the sample surfaces, and it is optimum if the interested event occurs within the later stages of compression.

Overall, MIG well reflects the speckle quality and can be used as a guideline while designing samples for dynamic XDIC analysis. It is shown that the number of error sites significantly increase as MIG of the image drops below 10. Although particle density governs the existence of error sites, with higher MIG, the error sites can quickly vanish as the sample is compressed, during which the particle density keeps increasing. It is worth noticing that the displacement error within the error sites can be as big as 3 pixels in the frames shown. This is far more than the theoretical error calculated as less than 0.01 pixels. However, the theoretical error only is only a statistical measure of the displacement deviation at each pixel. Errors at local regions can exceed this by a large value. This fact reemphasizes the importance of designing a sample such that the region of interest is away from regions where the error sites are likely to reside.

### **3.4 Kolsky Bar Results**

In this section, the results from the material response experiments with Kolsky compression bar are presented. The stress-strain relationships are displayed in groups for comparison. Comparison of samples of different FeO weight ratios with pure Sylgard®, samples of different WC weight ratios with pure Sylgard®, and cross comparison are given. In these experiments, rubber pulse shapers are used to generate a slow-ramping incident wave for the purpose of constant strain rate. A sample strain calculation during a loading of a single pulse is given in Fig. 62. The sample contains 4% FeO particles. The plot shows that the strain rate quickly ramps up to a constant value. The strain rate calculated is  $\sim 2900 \text{ } \epsilon^{-1}$ . This trend is found to be consistent throughout the experiments.

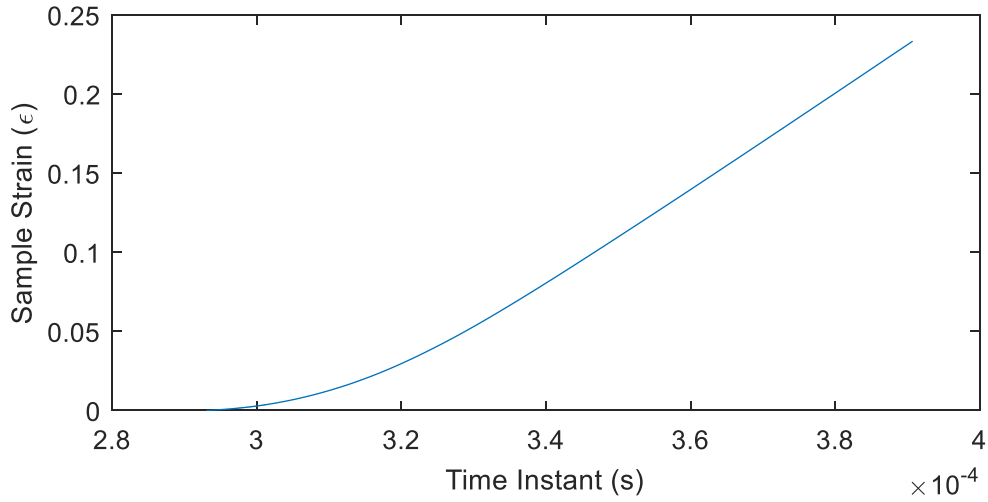


Figure 62. Calculated strain from single pulse loading for sample of 4% FeO.

Figures 63 and 64 show the comparison between FeO sample groups and WC sample groups with pure Sylgard® sample, respectively. Figure 65 compares the FeO samples with the WC samples at the same particle weight ratios. Most of the stress-strain curves stay close to that of pure Sylgard®, except for the 4% and 13% FeO samples. In general, samples with WC particles are more consistent and less scattered from the pure Sylgard®. However, no apparent relationship between stress-strain response and the particle content can be concluded from the plots. Significant distinction cannot be found between the samples with added particles and the pure Sylgard®.



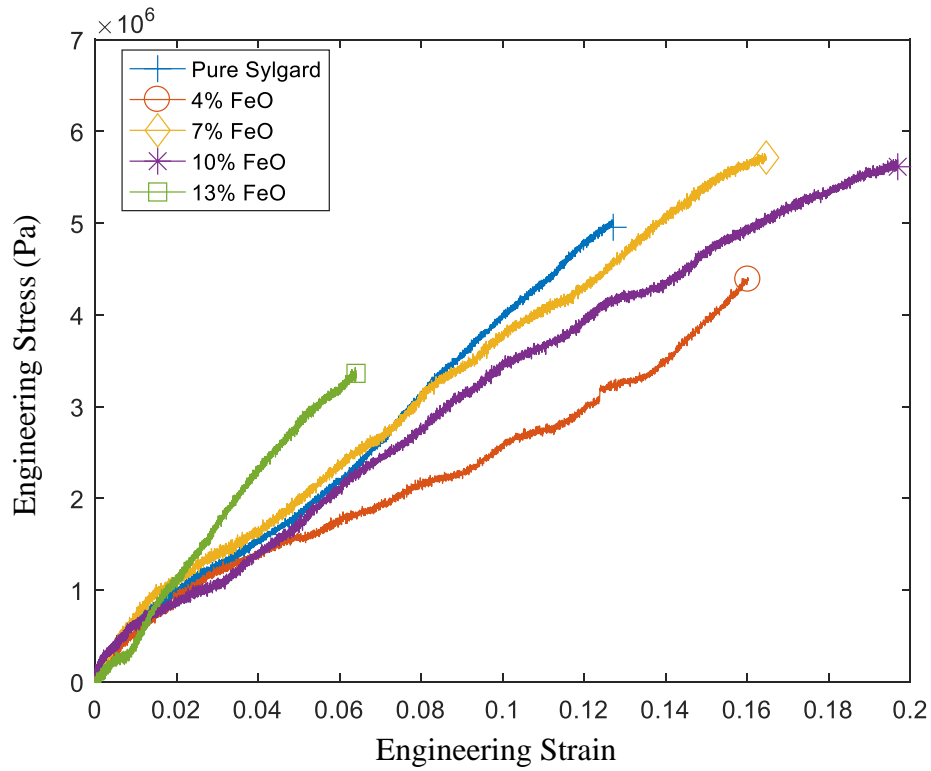


Figure 63. Comparison of FeO samples and pure Sylgard®.

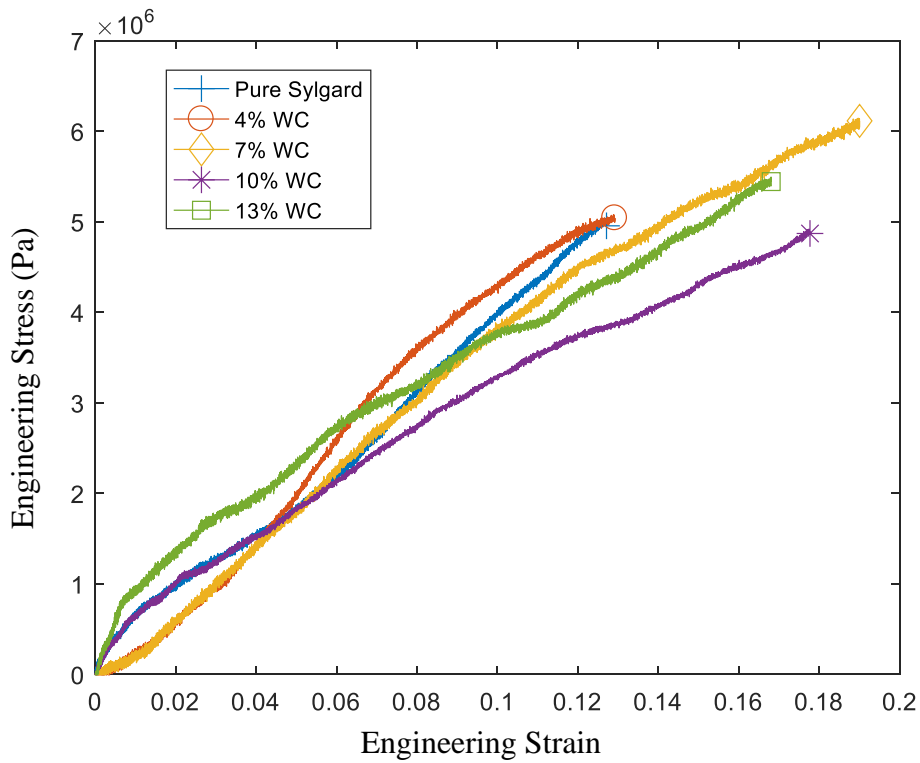


Figure 64. Comparison of WC samples and pure Sylgard®.

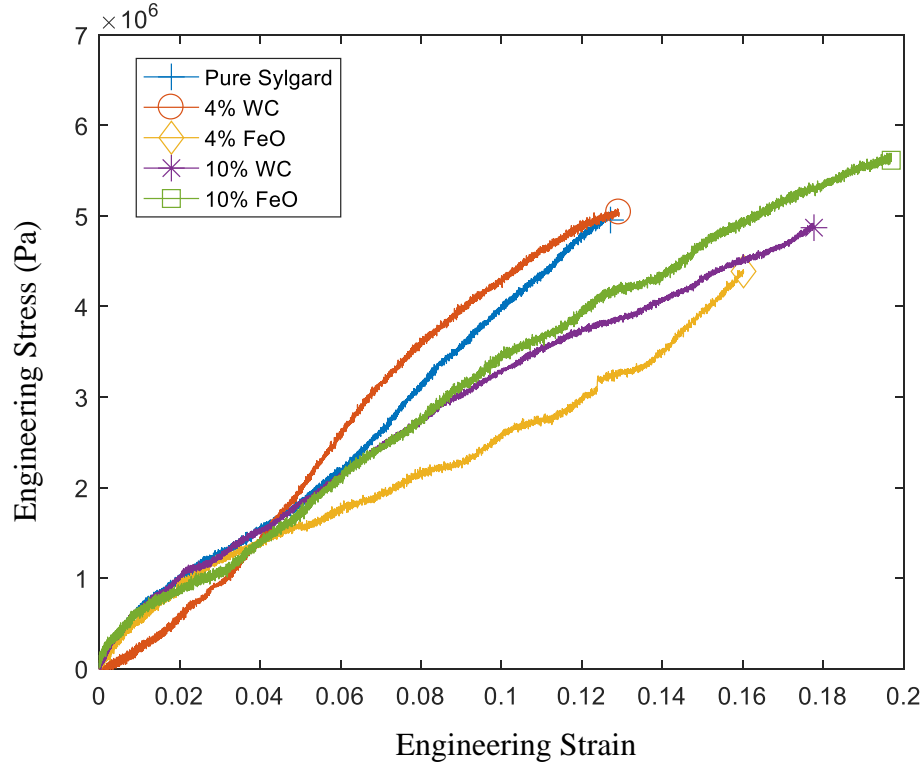


Figure 65. Comparison of WC samples and pure Sylgard®.

The Reuss and Voight limits are calculated for each sample using the linear regression of the measured Sylgard® stress-strain relation and tabulated properties of WC and FeO [38][39]. The bounds are given in Table. 6. It can be seen that the mechanical response is very close to the Reuss model. Since the modulus of Sylgard® is on a scale of  $10^{-4}$  of the inclusion's modulus, it is expected that the addition of particles does not significantly change the properties. Again, due to difference in loading conditions, there can be considerable fluctuation in the measurements. The tabulated properties of the inclusion materials do not reflect the properties of the materials used in this study either. However, Table. 6 provides a referential comparison to examine where the properties lie in the possible composite space. The scale difference between the Reuss and Voight limits should be sufficient to overcome fluctuations in tabulated properties and measurements in this study.

Table 6. Reuss and Voight Limits for Each Sample.

Particle Type	Reuss Limit (MPa)	Voight Limit (MPa)	Measured (MPa)
4% FeO	41.67	2.404E4	29.9
7% FeO	43.01	4.204E4	34.05
10% FeO	44.44	6.004E4	28.94
13% FeO	45.98	7.804E4	56.4
4% WC	41.67	2.404E4	44.12
7% WC	43.01	4.204E4	34.72
10% WC	44.44	6.004E4	27.51
13% WC	45.98	7.804E4	29.94

In the Kolsky bar measurements, the sample strain calculated from the bar strain signals stays consistent throughout all the samples studied, as well as the strain rates being  $\sim 2900$  /s consistently. What makes the curves different is the force measurement. Unlike the ability to calibrate strain input from the Kolsky bar apparatus, it is extremely difficult to enforce consistent loading condition for load measuring with the current setup. The sample placement significantly affects the load measurement. When setting up the experiments, effort was devoted to make sure the plunger and the sample are in good contact, and no significant strain was applied. This was not successfully achieved with the current setup. To improve the ability to control loading condition, a video recording device with magnification to monitor the sample placement should be considered. In addition, monitoring the load signal prior to loading could also help to find a good placement.

## 4. CONCLUSION

This study explored the applicability and the standards of embedding particles into transparent materials under X-ray PCI, especially polymers, in order to apply DIC analysis in dynamic experiments without significantly changing the properties of the samples. Three types of particles were embedded in Sylgard® epoxy to make small pieces of samples, and the samples were loaded with Kolsky compression bar and imaged with XPCI. The FeO powder and WC powder are the target materials with a range of weight ratios, and 5% Pt powder were used as a referential case due to the difficulty in applying in the samples used in this study. The PCI results were examined, and the speckle quality is assessed with intensity gradient analysis. DIC analysis were performed and examined. The stress-strain relations were characterized separately using a Kolsky compression bar with pulse-shaping techniques. The results were examined, and the property change due to addition of particles were assessed.

The PCI results suggest that WC is the superior choice of material to embed in polymers for speckle producing. Its high diffraction provides a good contrast, and its smaller size provides good pattern with high particle density. The mean intensity gradient ranges from 13.7 to 18.2, reflecting a decent speckle with theoretical pixel deviation error being 0.0041-0.0031 pixels. The correlation resolution can be as small as 11-8 pixels. On the other hand, FeO powders produce overall inferior speckle patterns. At lower content ratios, the MIG of the PCI images drop below 10 and inapplicable regions are likely to be present.

It is shown that monotonically increasing the particle weight ratio is progressively less effective in improving the speckle quality. Therefore, it is encouraged to use the least amount of inclusion that the accuracy allows. MIG and particle density can well serve as indicators to help find the optimal weight ratio. It is suggested that the sample is designed with MIG value of at least 10. For finer resolution (subset size below 20 X 20), MIG of at least 20 is suggested.

It is important to note that, during the loading event, speckle quality inside the sample is not evenly distributed both spatially and temporally. As the sample is compressed, the MIG increases after a small drop near the beginning of the loading event. The regions near the sample surfaces tend to shear in the X-ray direction, producing locally distorted speckle patterns near the surfaces, and thus introducing error sites. These two facts combined emphasizes the importance in sample design for experiments in which XDIC is applied. In an optimal design, the region of interest

should be away from the surface towards the back of the sample such that a small time period is required for the loading to reach the region of interest, during which the speckle quality is allowed to improve.

No conclusion of significant property change can be confidently made based on the experimental results. The sample strain is consistent, but the loading history is greatly affected by sample placement. However, the measured stress-strain relations of most particle types stayed close to the pure Sylgard® case. By comparing the stress-strain relation from regression with the Reuss and Voight limits, it is shown that the property change is not expected to be significant due to the addition of particles at low weight ratios (<13%) because the calculated modulus is very close to the Reuss limit. The modulus of Sylgard® is small enough to overcome the change caused by the particles. However, the loading history in this study never reached the failure regime. In applications where failures may happen, extra caution should be used because the addition of particles may also change the failure mechanism.

## 5. FUTURE RESEARCH

This work serves towards bridging the gap between traditional DIC and X-ray DIC that only applies to those with natural speckles. The role of this work is similar to speckle spraying in traditional DIC. Many improvements and future works can initiate from this work.

From a methodology development perspective, this work can be extended to form better standard in particle embedding for producing speckles. For example, combination of particles can be used to form more sophisticated speckle. The effectiveness can be assessed. The sample placement setup can be improved for better control, allowing more accurate force measurement so that the property change can be calibrated. The effect of sample thickness, which is important in accuracy in X-ray DIC analysis, remains unassessed in this work. Assessing such effect can even more greatly help application of particle embedding.

In the application aspect, what is learned in this work can make researchers more comfortable in extending their works. For example, with embedded particles, DIC analysis can be applied to a Sylgard® sample with HMX crystals in it to find the strain field around the crystal, providing a way to interpolate the strain field inside the HMX crystals using elasticity theories. In a polymer-based composite with microstructure much larger than the particle size, particle embedding can enable the application of FEM-DIC to study the deformation or even the failure mechanism of the microstructure.

It is important to note that this work is only the first attempt to calibrate particle embedding in order to produce speckles for DIC analysis as a methodology. Many details still remain unclear and extra caution is always suggested when applying this technique.

## REFERENCES

- [1] Peters, W. H, & Ranson, W. F. (1982). Digital Imaging Techniques In Experimental Stress Analysis. *Optical Engineering*, 21(3), 213427.
- [2] Peters, W. H, Ranson, W. F, Sutton, M. A, Chu, T. C, & Anderson, J. (1983). Application Of Digital Correlation Methods To Rigid Body Mechanics. *Optical Engineering*, 22(6), 226738.
- [3] Lin, Ming-Tzer, Sciammarella, Cesar, Espinosa, Horacio D, Furlong, Cosme, Lamberti, Luciano, Reu, Phillip, Sutton, Michael, Hwang, Chi-Hung. (2019). *Advancements in Optical Methods and Digital Image Correlation in Experimental Mechanics, Volume 3 (Conference Proceedings of the Society for Experimental Mechanics Series)*. Cham: Springer International Publishing AG.
- [4] Kirugulige, Madhu S, Tippur, Hareesh V, & Denney, Thomas S. (2007). Measurement of transient deformations using digital image correlation method and high-speed photography: Application to dynamic fracture. *Applied Optics. Optical Technology and Biomedical Optics*, 46(22), 5083-5096.
- [5] Reu, P L, & Miller, T J. (2008). The application of high-speed digital image correlation. *The Journal of Strain Analysis for Engineering Design*, 43(8), 673-688.
- [6] Sun, Yaofeng, and Pang, John H L. "AFM Image Reconstruction for Deformation Measurements by Digital Image Correlation." *Nanotechnology*, vol. 17, no. 4, 2006, pp. 933–939.
- [7] Sutton, M. A, Li, N, Joy, D. C, Reynolds, A. P, & Li, X. (2007). Scanning Electron Microscopy for Quantitative Small and Large Deformation Measurements Part I: SEM Imaging at Magnifications from 200 to 10,000. *Experimental Mechanics*, 47(6), 775-787.
- [8] Pan, Bing, Wu, Dafang, Wang, Zhaoyang, & Xia, Yong. (2011). High-temperature digital image correlation method for full-field deformation measurement at 1200 °C. *Measurement Science & Technology*, 22(1), 015701.
- [9] Grant, B M B, Stone, H J, Withers, P J, & Preuss, M. (2009). High-temperature strain field measurement using digital image correlation. *The Journal of Strain Analysis for Engineering Design*, 44(4), 263-271.

- [10] Huang, JianWen, Zhang, Lingqi, Jiang, Zhenyu, Dong, Shoubin, Chen, Wei, Liu, Yiping, Liu, Zejia, Zhou, Licheng, and Tang, Liquan. (2018). Heterogeneous parallel computing accelerated iterative subpixel digital image correlation. *Science China. Technological Sciences*, 61(1), 74-85.
- [11] Xiong, Chen, Chen, Jiatao, Li, Feng, and Cai, Ming. (2019). Fast digital image correlation using parallel temporal sequence correlation method. *Optical Engineering*, 58(12), 124101.
- [12] Pan, Bing, Wu, Dafang, and Yu, Liping. (2012). Optimization of a three-dimensional digital image correlation system for deformation measurements in extreme environments. *Applied Optics* (2004), 51(19), 4409-4419.
- [13] Ma, Shaopeng, Zhao, Zilong, & Wang, Xian. (2012). Mesh-based digital image correlation method using higher order isoparametric elements. *The Journal of Strain Analysis for Engineering Design*, 47(3), 163-175.
- [14] Yoneyama, S. (2016). Basic principle of digital image correlation for in-plane displacement and strain measurement. *Advanced Composite Materials*, 25(2), 105-123.
- [15] Lu, L, Fan, D, Bie, B. X, Ran, X. X, Qi, M. L, Parab, N, Sun, J. Z, Liao, H. J, Hudspeth, M. C, Claus, B, Fezzaa, K, Sun, T, Chen, W, Gong, X. L, Luo, S. N. (2014). Note: Dynamic strain field mapping with synchrotron X-ray digital image correlation. *Review of Scientific Instruments*, 85(7), 076101.
- [16] Wagner, Karla B, Keyhani, Amirreza, Boddorff, Andrew K, Kennedy, Gregory, Montaigne, Didier, Jensen, Brian J, Beason, Matthew, Zhou, Min, Thadhani, Naresh N. (2020). High-speed x-ray phase contrast imaging and digital image correlation analysis of microscale shock response of an additively manufactured energetic material simulant. *Journal of Applied Physics*, 127(23), 235902.
- [17] Pan, Bing, & Wang, Bo. (2020). Some recent advances in digital volume correlation. *Optics and Lasers in Engineering*, 135, 106189.
- [18] Buljac, A, Jailin, C, Mendoza, A, Neggers, J, Taillandier-Thomas, T, Bouterf, A, Smaniotto, B, Hild, F, Roux, S. (2018). Digital Volume Correlation: Review of Progress and Challenges. *Experimental Mechanics*, 58(5), 661-708.



- [19] Hudspeth, M, Claus, B, Dubelman, S, Black, J, Mondal, A, Parab, N, Funnell, C, Hai, F, Qi, M. L, Fezzaa, K, Luo, S. N, Chen, W. (2013). High speed synchrotron x-ray phase contrast imaging of dynamic material response to split Hopkinson bar loading. *Review of Scientific Instruments*, 84(2), 025102.
- [20] Chen, Weinong W, Hudspeth, Matthew C, Claus, Ben, Parab, Niranjana D, Black, John T, Fezzaa, Kamel, & Luo, S N. (2014). In situ damage assessment using synchrotron X-rays in materials loaded by a Hopkinson bar. *Philosophical Transactions of the Royal Society of London. Series A: Mathematical, Physical, and Engineering Sciences*, 372(2015), 20130191.
- [21] Pan, Bing, Qian, Kemao, Xie, Huimin, & Asundi, Anand. (2009). Two-dimensional digital image correlation for in-plane displacement and strain measurement: A review. *Measurement Science & Technology*, 20(6), 062001.
- [22] Paulson, Shane C, Roberts, Zane A, Sorensen, Christian J, Kerschen, Nicholas E, Harr, Michael H, Parab, Niranjana D, Sun, Tao, Fezzaa, Kamel, Son, Steven F, Chen, Wayne W. (2019). Observation of Damage During Dynamic Compression of Production and Low-Defect HMX Crystals in Sylgard® Binder Using X-Ray Phase Contrast Imaging. *Journal of Dynamic Behavior of Materials*, 6(1), 34-44.
- [23] Wu, S.Y, Bie, B.X, Fan, D, Sun, T, Fezzaa, K, Feng, Z.D, Huang, J. Y, Luo, S.N. (2018). Dynamic shear localization of a titanium alloy under high-rate tension characterized by x-ray digital image correlation. *Materials Characterization*, 137(C), 58-66.
- [24] Pan, Bing, Lu, Zixing, & Xie, Huimin. (2010). Mean intensity gradient: An effective global parameter for quality assessment of the speckle patterns used in digital image correlation. *Optics and Lasers in Engineering*, 48(4), 469-477.
- [25] Bie, B.X, Huang, J.Y, Su, B, Lu, L, Fan, D, E, J.C, Sun, T, Fezzaa, K, Luo, S.N. (2016). Dynamic tensile deformation and damage of B4C-reinforced Al composites: Time-resolved imaging with synchrotron x-rays. *Materials Science & Engineering. A, Structural Materials : Properties, Microstructure and Processing*, 664(C), 86-93..
- [26] Balerna, Antonella, & Mobilio, Settimio. (2014). Introduction to Synchrotron Radiation. In *Synchrotron Radiation* (pp. 3-28). Berlin, Heidelberg: Springer Berlin Heidelberg.

- [27] Spanne, P, Raven, C, Snigireva, I, & Snigirev, A. (1999). In-line holography and phase-contrast microtomography with high energy x-rays. *Physics in Medicine and Biology*, 44(3), 741-749.
- [28] Parab, Niranjana D, Claus, Benjamin, Hudspeth, Matthew C, Black, John T, Mondal, Alex, Sun, Jianzhuo, Fezzaa, Kamel, Xiao, Xianghui, Luo, S. N, Chen, Wayne. (2014). Experimental assessment of fracture of individual sand particles at different loading rates. *International Journal of Impact Engineering*, 68, 8-14.
- [29] Parab, Niranjana D, Black, John T, Claus, Benjamin, Hudspeth, Matthew, Sun, Jianzhuo, Fezzaa, Kamel, & Chen, Weinong W. (2014). Observation of Crack Propagation in Glass Using X-ray Phase Contrast Imaging. *International Journal of Applied Glass Science*, 5(4), 363-373.
- [30] Parab, Niranjana D, Guo, Zherui, Hudspeth, Matthew C, Claus, Benjamin J, Fezzaa, Kamel, Sun, Tao, & Chen, Weinong W. (2017). Dynamic fracture behavior of single and contacting Poly(methyl methacrylate) particles. *Advanced Powder Technology : The International Journal of the Society of Powder Technology, Japan*, 28(11), 2929-2939.
- [31] Nie, Yizhou, Parab, Niranjana D, Chu, Jou-Mei, Kim, Garam, Sun, Tao, Fezzaa, Kamel, Sterkenburg, Ronald, Chen, Weinong W. (2018). Dynamic crack propagation from a circular defect in a unidirectional carbon fiber reinforced plastic composite. *Journal of Composite Materials*, 52(25), 3539-3547.
- [32] Hudspeth, Matthew, Claus, Ben, Parab, Niranjana, Lim, Boonhim, Chen, Weinong, Sun, Tao, & Fezzaa, Kamel. (2015). In Situ Visual Observation of Fracture Processes in Several High-Performance Fibers. *Journal of Dynamic Behavior of Materials*, 1(1), 55-64.
- [33] Zhai, Xuedong, Guo, Zherui, Gao, Jinling, Kedir, Nesredin, Nie, Yizhou, Claus, Ben, Sun, Tao, Xiao, Xianghui, Fezzaa, Kamel, Chen, Weinong W. (2019). High-speed X-ray visualization of dynamic crack initiation and propagation in bone. *Acta Biomaterialia*, 90(C), 278-286.
- [34] Kolsky, H. "An Investigation of the Mechanical Properties of Materials at Very High Rates of Loading." *Proceedings of the Physical Society. Section B*, vol. 62, no. 11, 1949, pp. 676-700.
- [35] Song, B, Chen, W, & Jiang, X. (2005). Split Hopkinson pressure bar experiments on polymeric foams. *International Journal of Vehicle Design*, 37(2-3), 185-198.

- [36] Chen, Weinong W, & Song, Bo. (2010). Split Hopkinson (Kolsky) Bar (Mechanical Engineering Series). New York, NY: Springer.
- [37] Vendroux, G, & Knauss, W. G. (1998). Submicron deformation field measurements: Part 2. Improved digital image correlation. *Experimental Mechanics*, 38(2), 86-92.
- [38] Ouglova, A, Berthaud, Y, François, M, & Foct, F. (2006). Mechanical properties of an iron oxide formed by corrosion in reinforced concrete structures. *Corrosion Science*, 48(12), 3988-4000.
- [39] Fang, Z. Zak, Wang, Xu, Ryu, Taegong, Hwang, Kyu Sup, & Sohn, H.Y. (2009). Synthesis, sintering, and mechanical properties of nanocrystalline cemented tungsten carbide – A review. *International Journal of Refractory Metals & Hard Materials*, 27(2), 288-299.

## **VITA**

Junyu Wang is a Master of Science student in the school of Aeronautics and Astronautics at Purdue University working with Prof. Wayne Chen in his Impact Science Laboratory. Junyu Wang finished his Bachelor of Science degree in Aerospace Engineering at Missouri University of Science and Technology before his graduate study at Purdue University. Junyu Wang's research interest covers broadly in failure mechanism characterization of materials under high-rate loading, optimization of materials towards better failure mechanisms, as well as methodology development related to high-rate experiments. He enjoys exploring the science of material response via experimental study and wishes to make value out of his knowledge to serve the society and human as an entirety.